Shock-wave and high strain-rate phenomena in matter: modeling and applications

POLITECNICO DI TORINO

Ph. D. in Mechanics
(S.D. ING-IND/14)
XXV Ph.D. Course

PH.D. THESIS

Shock-wave and high strain-rate phenomena in matter: modeling and applications

Martina Scapin

Tutor
Prof. Massimiliano Avalle

Coordinator
Prof. Luigi Garibaldi

February 2013

Acknowledgements

Some topics discussed in this thesis are developed as part of WP8 ColMat of the EuCARD Project (co-funded by the European Commission within the Framework Programme 7 Capacities Specific Programme, under Grant Agreement no 227579).

I want to thank all the people who helped and supported me during my PhD.

Index

1. Introduction

The understanding of the material response in case of high strain-rate, impact or shock loading is fundamental in several applications, such as e.g. ballistic, nuclear and military fields. The objective of the investigation of wave propagation in solids is the development of reliable methods for the prediction of dynamic events, such as high velocity or high energy impacts and detonation of explosives. In these events, usually, both high compression and expansion are involved and it is necessary to know physical, mechanical and thermodynamic properties of involved materials in wide ranges of densities, temperatures and deformations.

The first chapter describes the problems correlated to shock regime and tries to collect the tools necessary to cope with the description of high dynamic regime. The concept of shock-wave phenomena is introduced and then the description of planar wave propagation in solid is reported. The analysis starts from the propagation of elastic wave and then extends to shock-wave propagation in fluids and solid. For each case presented, the corresponding numerical model is developed, aiming to highlight the main features of the investigated phenomenon. At the end of the first chapter, the propagation of cylindrical waves is also treated and the results are compared with the planar case.

In the usual continuum mechanics treatment, the complete stress tensor, which describes the material condition state, is divided into two components: the deviatoric and the hydrostatic tensors. In high strain-rate and shock loading conditions, the choice of the material constitutive equations, which includes both strength model (deviatoric component) and equation of state (hydrodynamic component), is of fundamental importance: in chapter 2 the attention is focused on the hydrodynamic response, while in

chapter 3 on the material strength.

In impact, shock or generally high strain-rate regime, the material covers a wide range of different possible states. For example, some parts of the material can be subjected to high pressure and temperature and this implies that the thermodynamic response prevails on the mechanical one. On the other hand, other parts of material can remain in a low pressure condition, in which it is not possible to neglect the mechanical strength, which becomes the dominant part of the material response. In chapter 2, the concept of Equation Of State (EOS) is introduced, starting from the thermodynamic theory. The main characteristics of the EOS are described, with particular reference to their implementation in most of the commercial FE and hydrodynamic codes. In the last part of chapter 2, an overview of some EOS is reported, focusing the attention on their formulation and range of applicability: for each EOS presented, the trend of the pressure is reported on the basis of the data available in literature for different materials.

For the visco-thermo-plastic behaviour description, the definition of constitutive relations is needed, in which the flow stress is defined as a function of all the variables of interest. Usually, in plasticity, the independent variables are: deformation (both plastic and volumetric), strain-rate, temperature and pressure. This aspect is treated in chapter 3, in which the concepts at the basis of the definition of strength material models are described, with particular reference to the high strain-rate and shock-wave regime. In this perspective, an overview of all the variables of interest in such kind of problems is examined. Then, the most common strength models, usually implemented in commercial FE codes, are examined, paying attention to the meaning of each model parameter and the availability of data for different materials, for which the plastic behaviour is analyzed and compared. After this, also some failure models, which should be defined in a numerical model for the complete description of the material behaviour, are presented and in the final part of the chapter 3, a procedure for the material model identification, based on a numerical inverse method, is presented.

In chapters 5 to 7 the shock-wave propagation in matter, due to the interaction of high energy particle beams with solids is analyzed. The main objective of this study is to build safe and reliable numerical models able to estimate the damage on targets due to the impact of high energy proton beam in CERN Large Hadron Collider (LHC). To do this, all the concepts introduced in the previous chapter are used.

In chapter 5 the problem is introduced on its generality: after a brief introduction to the

LHC, the interaction between intense beam and solid targets is investigated from a qualitative and phenomenological point of view. This allows the comprehension of the involved phenomena, which is necessary for the construction of the numerical model described in chapters 6 and 7.

In chapter 6, the numerical simulation of the high energy deposition on cylindrical bars, hit at the centre of one face by 8 proton bunches of the LHC at 7 TeV is performed. Two cases are analyzed, varying the material of the target (copper and tungsten). For each case a Lagrangian 2D axisymmetric simulation is performed, starting from the energy deposition map.

In chapter 7, the impact of high energy proton beams against 3D structures is described: the FE solution is obtained in case of Lagrangian and pure structural analysis solved with an explicit time integration method, on 3D solid elements. Two different cases are reported. In the first one, the impact is simulated on the simplified model of a Tertiary collimator and the impact condition implies that the target is impacted perpendicularly to the free surface by 8 protons bunches at 5 TeV. The description of this case is of particular interest for the evaluation of the consequences of the impact near a free surface. For the second case, the objective is the description of a numerical procedure, for a soft coupling between the FLUKA and the LS-DYNA codes, developed in collaboration with the FLUKA Team at CERN. The main objective is evaluating the influence of the change in density on the deposition phase. In order to achieve this, a great number of bunches (60) are supposed to impact against a tungsten parallelepiped.

The studies presented in chapter 5 to 7 are developed within the European project EuCARD (European Coordination for Accelerator Research & Development), which is co-funded by the European Commission within the Framework Programme 7 Capacities Specific Programme. In more details, the Work Package (WP) 8 is involved. The WP8, named ColMat, Collimations & Materials for higher beam power beam, has the main objectives the development of material and machine components related to collimation system and intercepting devices.

The last chapter is dedicated to the description of an experiment (first-of-its-kind), in which the responses of different materials are measured under the controlled impact of a high energy proton beam with the aim to validate numerical models and extract material data in terms of strength and EOS models. The experiment was performed in the HiRadMat facility at CERN in October 2012 and some preliminary results are shown. The

description of the experiment is also reported, paying particular attention to the most relevant aspects of the design phase, including the choice of materials and impact conditions.

2. Shock-waves in solids

The study of the dynamic behaviour of materials involves different scientific disciplines. In general, the processes to which a material is subjected in case of high dynamic loading conditions are significantly different from those related to quasi-static situations. This chapter describes the problems correlated to shocks and tries to collect the tools necessary to cope with the description of high dynamic regime. In more details, after a brief summary, in which the shock-wave phenomena are introduced, the description of planar wave propagation in solid is reported, starting from the propagation of elastic wave and reaching the shock-wave propagation in fluids and solid. For each case presented, some numerical models are developed, with the aim to highlight the main features of the investigated phenomenon. At the end of this chapter, the case of the propagation of cylindrical wave is also treated and the results are compared with the planar case.

The understanding of the material response in case of high strain-rate, impact or shock loading is fundamental in several applications, such as e.g. ballistic, nuclear and military fields. The objective of the investigation of wave propagation in solids is the development of reliable methods for the prediction of dynamic events, such as high velocity or high energy impacts and detonation of explosives. In these events, usually, both high compression and expansion are involved and it is necessary to know physical, mechanical and thermodynamic properties of involved materials in wide ranges of densities, temperatures and deformations.

Shock-wave techniques provide a very important source of data for this purpose. As a

matter of fact, they are used in order to investigate range of the state of the matter, which can not be investigated using other methods. In these conditions, the state of the matter is characterized by high pressure and high rate of deformation. Another important aspect of using shock experiments is to investigate material changes, which occur after the wave propagation. In this sense, it is possible to investigate the effects of chemical and metallurgical changes, phase transition, fragmentation, etc.

Usually, the experiments are based on producing plane shock compression with different methods: hypervelocity impacts, shock tubes, explosions and energy depositions. In general, at least in the portion of material in which the shock is generated, a uniaxial strain state is generated, while the stress state is three-dimensional.

A complete and exhaustive treatment of the shock-wave propagation in solids and high velocity impact dynamic phenomena can be found in [1-3].

2.1 Acoustic waves

The complete behaviour of materials is, usually, described in function of stress and strain tensors, which are defined as:

$$\sigma = \begin{bmatrix} \sigma_{xx} & \sigma_{xy} & \sigma_{xz} \\ \sigma_{yx} & \sigma_{yy} & \sigma_{yz} \\ \sigma_{zx} & \sigma_{zy} & \sigma_{zz} \end{bmatrix} = \begin{bmatrix} s_{xx} & s_{xy} & s_{xz} \\ s_{yx} & s_{yy} & s_{yz} \\ s_{zx} & s_{zy} & s_{zz} \end{bmatrix} - \begin{bmatrix} p & 0 & 0 \\ 0 & p & 0 \\ 0 & 0 & p \end{bmatrix}$$
$$\varepsilon = \begin{bmatrix} \varepsilon_{xx} & \varepsilon_{xy} & \varepsilon_{xz} \\ \varepsilon_{yx} & \varepsilon_{yy} & \varepsilon_{yz} \\ \varepsilon_{zx} & \varepsilon_{zy} & \varepsilon_{zz} \end{bmatrix} = \begin{bmatrix} e_{xx} & e_{xy} & e_{xz} \\ e_{yx} & e_{yy} & e_{yz} \\ e_{zx} & e_{zy} & e_{zz} \end{bmatrix} + \frac{1}{3}\begin{bmatrix} \varepsilon_v & 0 & 0 \\ 0 & \varepsilon_v & 0 \\ 0 & 0 & \varepsilon_v \end{bmatrix} \tag{2.1}$$

in which the pressure P and the volumetric strain ε_v are, respectively, defined as

$$P = -\frac{\sigma_{xx} + \sigma_{yy} + \sigma_{zz}}{3}$$
$$\varepsilon_v = \varepsilon_{xx} + \varepsilon_{yy} + \varepsilon_{zz} \tag{2.2}$$

In this way the complete tensors are split into deviatoric and hydrostatic components. The constitutive law defines the relation between deviatoric stress and strain components, while the equation of state between the hydrostatic ones.

Before entering more in depth in the explanation of wave propagation and its features, it is convenient to recall the elastic stress-strain relations for some states of stress or deformation which will be of particular interest in the following treatment. In general in elasticity:

$$\begin{Bmatrix} \varepsilon_{xx} \\ \varepsilon_{yy} \\ \varepsilon_{zz} \\ \varepsilon_{xy} \\ \varepsilon_{xz} \\ \varepsilon_{yz} \end{Bmatrix} = \begin{bmatrix} 1/E & -\upsilon/E & -\upsilon/E & 0 & 0 & 0 \\ -\upsilon/E & 1/E & -\upsilon/E & 0 & 0 & 0 \\ -\upsilon/E & -\upsilon/E & 1/E & 0 & 0 & 0 \\ 0 & 0 & 0 & 1/G & 0 & 0 \\ 0 & 0 & 0 & 0 & 1/G & 0 \\ 0 & 0 & 0 & 0 & 0 & 1/G \end{bmatrix} \begin{Bmatrix} \sigma_{xx} \\ \sigma_{yy} \\ \sigma_{zz} \\ \sigma_{xy} \\ \sigma_{xz} \\ \sigma_{yz} \end{Bmatrix} \tag{2.3}$$

in which E is the Young's modulus, υ the Poisson's ratio and G the shear modulus. Each elastic constant can be derived if other two are known, e.g. the shear modulus and the bulk modulus (K) can be obtained as combination of the Young's modulus and the Poisson ratio:

$$\begin{aligned} G &= \frac{E}{2(1+\upsilon)} \\ K &= \frac{E}{3(1-2\upsilon)} \end{aligned} \tag{2.4}$$

The case of uniaxial stress corresponds to the state of unconfined compression. In this case, the only stress component different from zero is σ_{xx}, while the deformation state is triaxial. The governing equations are derived from Eq. 2.3 imposing $\sigma_{yy}=\sigma_{zz}=0$ and can be summarized as follows:

$$\begin{aligned} \sigma_{xx} &= E\varepsilon_{xx} \\ \varepsilon_{v} &= (1-2\upsilon)\varepsilon_{xx} \end{aligned} \tag{2.5}$$

When the compression can be considered confined such as the deformation can occur only in one direction, the strain state is uniaxial, while the stress state is triaxial. In this case the governing equations are derived from Eq. 2.3 imposing $\varepsilon_{yy}=\varepsilon_{zz}=0$ and can be expressed as:

$$\sigma_{xx} = \left(K + \frac{4}{3} G \right) \varepsilon_{xx}$$
$$\varepsilon_v = \varepsilon_{xx} \tag{2.6}$$

The last case taken into account is the hydrostatic state, in which the three normal components of stress are all equal to the pressure (opposite in sign). This implies that also the three normal components of strain are equal. In more details, the pressure is proportional to the volumetric strain, and the scale factor is represented by the bulk modulus:

$$P = -K\varepsilon_v = -K \frac{v - v_0}{v_0} \tag{2.7}$$

in which v is the specific volume, defined as the inverse of the density. From the last equation, it is possible to conclude that linear elasticity, implies also linear equation of state in volume.

An acoustic (elastic) wave corresponds to small pressure changes. The partial differential equation, which describes the elastic wave propagation, can be easily obtained starting from equilibrium consideration [3] of an infinitesimal portion of material and, independently from the stress/strain state, it assumes the form:

$$\frac{\partial^2 u}{\partial x^2} = \frac{1}{c^2} \frac{\partial^2 u}{\partial t^2} \tag{2.8}$$

The term c, which represents the speed of propagation of the elastic perturbation, assumes different expression in function of the case which is considered:

$$c = \sqrt{\frac{E}{\rho_0}} \quad \text{uniaxial stress}$$
$$c = \sqrt{\frac{K + \frac{4}{3} G}{\rho_0}} \quad \text{uniaxial strain} \tag{2.9}$$
$$c = \sqrt{\frac{K}{\rho_0}} \quad \text{hydrostatic stress}$$

The main features of an elastic wave are that the wave front does not change shape

during the propagation. This is strictly correlated to the fact that the wave velocity is constant with respect to the undisturbed material and is equal to the sound speed in the undisturbed material.

2.2 Hydrodynamic materials

When the deviatoric component of stress is much smaller with respect to the pressure, it can be neglected. In this condition, the material law is fully defined only by the equation of state. The hydrodynamic response of materials can be applied if:

- ✓ the material is loaded in a hydrodynamic way, but this condition is very difficult to be reached for metals;
- ✓ the material has a very low shear stiffness, as e.g. in fluids;
- ✓ metals are subjected to very high compressive loads: in this case the yield of the material limits the deviatoric response, but the pressure can exceed the yield stress by more than 2 orders of magnitude.

Considering a hydrodynamic stress wave travelling in the material, it is possible to conclude that, in general:

$$c = \sqrt{\frac{\mathrm{d}P}{\mathrm{d}\rho}} \tag{2.10}$$

The previous definition can also be derived with respect to the specific volume, just making a change of variables:

$$c = \sqrt{\frac{\mathrm{d}P}{\mathrm{d}v}\frac{\mathrm{d}v}{\mathrm{d}\rho}} = v\sqrt{-\frac{\mathrm{d}P}{\mathrm{d}v}} \tag{2.11}$$

By definition, an equation of state, which defines the pressure P as function of the specific volume v (or density), respects the following inequality (see the chapter 3 for an exhaustive treatment of the argument):

$$\frac{\partial P}{\partial v} < 0$$
$$\frac{\partial^2 P}{\partial v^2} > 0 \qquad (2.12)$$

Such an EOS is defined as stiffening: the pressure grows faster than linearly with the volume. This implies that the wave velocity c increases if the pressure increases.

2.3 Shock in fluids

In general, a shock is characterized by a propagating surface in which the displacement is continuous, but other properties, such as density, pressure (or stress), particle velocity and in general the other thermodynamic quantities are discontinuous. In the matter, as mentioned before, the speed of sound, which is the speed of the wave inside the material, can be defined as the square root of the ratio between the change in pressure with respect to the change in density. This means that, beyond the elastic regime, the sound speed continues to increase with pressure, if a stiffening EOS is considered. This implies that a disturbance front, which at the beginning can be quite smooth, continues to steepen up while travelling into the material.

Usually, when a shock front is generated in solid matter, the pressure generated is so high with respect to the strength of the material, that the latter could be neglected. In this condition the material can be approximated with a fluid. In this sense, what is deduced in this section for fluids can be applied also in case of solid materials subject to strong shocks.

2.3.1 The Rankine-Hugoniot jump condition

In order to better understand the problem, it is possible to refer to the condition in which a compressible fluid is inside a tube, which is open to one side and closed by a piston to the other (see Fig. 2.1). At the beginning the piston is at rest, and the fluid initial conditions are defined as ρ_0, P_0, E_0 and u_{P0}=0 (also the fluid is at rest). Then suppose that the piston reaches the finite velocity up causing the generation of a shock-wave (labelled *S*) on the piston surface. The shock-wave starts to travel inside the material with a velocity

$U_S > u_{P1}$. The material placed beyond the shock front is pushed to reach the new conditions ρ_1, P_1, E_1 and u_{P1}. The material placed ahead of the shock front remains in the undisturbed initial conditions.

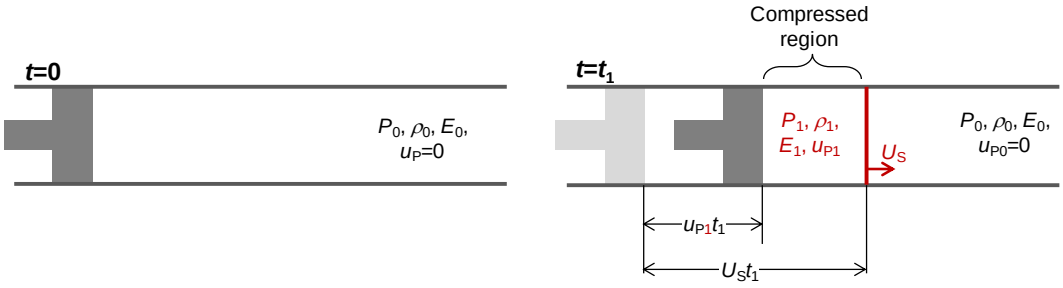

Fig. 2.1: Compressible fluid in which a shock-wave is generated.

In Fig. 2.2 the pressure is reported in function of both time and spatial coordinate (in the shock travel direction). If the applied load is of finite duration (e.g. the piston stops moving), an unloading wave (rarefaction wave) is generated from the rear. The unloading wave, which travels in the compressed material is faster than the shock front. Hence, there is a time in which the rarefaction wave reaches the shock front reducing it intensity. It is important to note that, always, a real shock front has a finite rise time also if small. The vertical line of Fig. 2.2, which represents the shock front is an idealization.

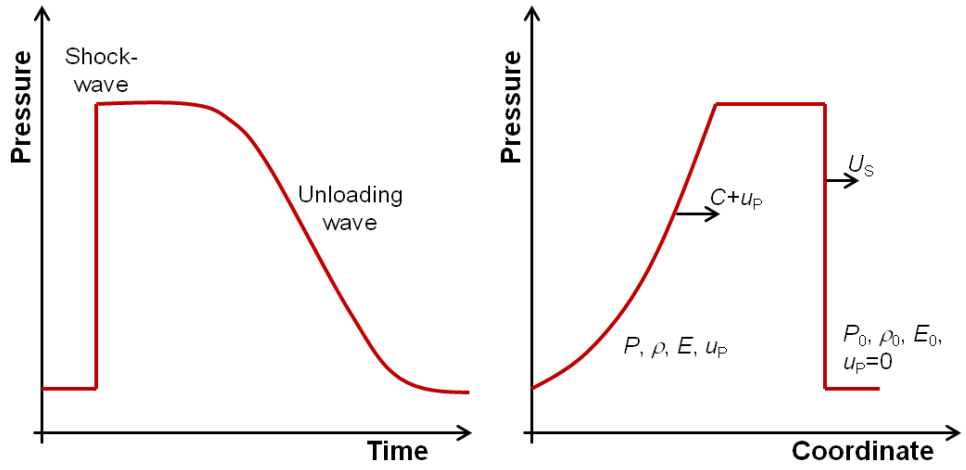

Fig. 2.2: Pressure in case of shock: in function of time (left) and spatial coordinate (right).

Supposing that the material immediately behind and after the shock front is in equilibrium condition, the conservation laws can be applied. The conservation of mass implies that the mass (per unit area) moving toward the front and that moving away from it are equal. This states that:

$$\rho_0 U_S = \rho_1 (U_S - u_{P1}) \tag{2.13}$$

The conservation of momentum requires that the difference in the momentum ahead and behind the front is equal to the impulse per unit of cross-sectional area:

$$P_1 - P_0 = \rho_0 U_S u_{P1} \tag{2.14}$$

in which the quantity $U_S\, u_{P1}$ is the shock impedance.

The conservation of energy requires that the work done by the shock wave is equal to the sum of the increase in both kinetic and internal energy:

$$P_1 u_{P1} = \frac{1}{2}\rho_0 U_S u_{P1}^2 + \rho_0 U_S (E_1 - E_0) \tag{2.15}$$

The three Eqs. 2.13, 2.14 and 2.15 are a system of equations in five unknowns, which are u_{P1}, U_S, ρ_1, P_1 and E_1. On the other hand, the quantities with the subscript 0, which refer to the initial condition, are assumed to be known. So at this time the system is undetermined.

By eliminating from the conservation laws the velocity U_S and u_{P1}, it is possible to obtain a single equation, which is function of the state variable ρ_1, P_1 and E_1:

$$E_1 = E_0 + \frac{(P_1 + P_0)(\rho_1 - \rho_0)}{2\rho_0\rho_1} \tag{2.16}$$

which is known as the Hugoniot equation and is fundamental in the shock-wave theory.

In order to be able to completely define the final state of a system invested by a shock front and in order to plot the Hugoniot curve it is necessary to add an equation. The equation needed to complete the system, is the equation of state of the material, i.e. $P=f(E,\rho)$. For an in-depth treatment see the chapter 3. Starting from the Eq. 2.16 and combining the EOS of the material, the energy could be eliminated obtaining the expression $P=f(\rho)$, or similarly, in function of the specific volume, $P=f(v)$. These last expressions define one form of the so called Hugoniot curve (see Fig. 2.3).

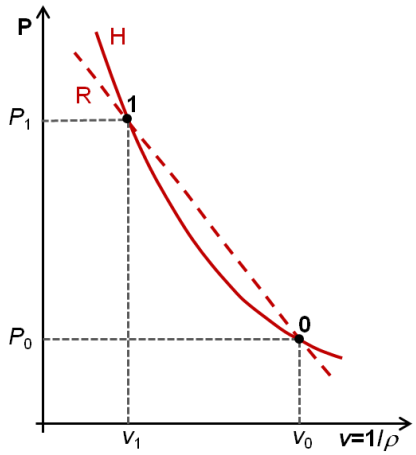

Fig. 2.3: Hugoniot, Rayleigh curves in the pressure vs. specific volume plane.

The Hugoniot curve does not represent a real hydrodynamic path on the surface of an EOS. It is the locus of all the states that can be reached during a shock, starting from the initial condition indicated with the subscript 0. So, it describes only the state of the material in compression. With reference to Fig. 2.3, when the material is shocked from the point indicated as 0 to that indicated as 1, the material does not follow the Hugoniot curve (H). Better, the pressure changes discontinuously from the initial value to the final one. The discontinuity is governed by the slope of the Rayleigh (R) curve, which is the line between the states 0 and 1 and can be defined as:

$$P = \frac{P_1 - P_0}{v_1 - v_0}\left(v - v_0\right) \tag{2.17}$$

An important path on the EOS surface in case of shocked material is the isentropic transformation (adiabatic and reversible transformation), which defines the release condition, or more precisely, the material unloading starting from the state reached after the shock. Usually, for materials the isentrope is very close to the Hugoniot, so practically the Hugoniot can approximate also the unloading path. In any case, the area between the loading and the unloading paths represents the energy stored in the material during the shock process and converted into heat.

Another possibility to eliminate one variable from the conservation laws is funding a relation between two variables, which represents the fourth equation of the system. One of the most useful form is to represent the curve, which defines the U_S vs. u_P relation. This can be determined experimentally on the basis of flyer impact tests varying the impact

velocity. Usually, a polynomial is then used to fit the experimental data:

$$U_S = C_0 + S_1 u_P + S_2 u_P^2 + \ldots \tag{2.18}$$

where C_0 is the sound material at zero pressure and the coefficient S_i are to be determined. For most metals, all the S_i coefficients, except S_1, are equal to zero. Since in shock-waves, U_S has to be greater that u_P, S_1 hat to be greater (or at least equal) than unity. Otherwise, the unphysical condition in which $U_S < u_P$ happens for $C_0 < (S_1\text{-}1)\, u_P$.

Other relation between the shock parameters based on the definition of C_0 and S_1 are:

$$P = \frac{C_0^2 (v_0 - v)}{\left[v_0 - S_1 (v_0 - v)\right]^2} \tag{2.19}$$

which expresses the relation between pressure and specific volume. Another useful approach is considering the pressure in function on particle velocity:

$$P = \rho_0 \left(C_0 u_P + S_1 u_P^2\right) \tag{2.20}$$

All the possible relations between two of the four variables of the problem, which appear in Eq. 2. 13 (conservation of mass) and Eq. 2.14 (conservation of momentum) can be found in [3]. In Table 2.1 the C_0 and S_1 parameters for various materials are reported [4].

Table 2.1: Hugoniot materials data [4]

Material	**Density (kg/dm3)**	**C_0 (km/s)**	**S_1 (-)**
Al 6061	2.073	5.35	1.34
Brass	8.413	3.52	1.55
Copper	8.924	3.91	1.51
Lead	11.346	2.03	1.47
Molybdenum	10.208	5.14	1.22
Tantalum	16.656	3.43	1.19
Tungsten	19.2	4.04	1.23

In Fig. 2.4 shock speed vs. particle velocity, pressure vs. particle velocity and pressure vs. relative volume curves are reported in accordance to Eqs. 2.18, 2.19 and 2.20 and data of Table 2.1.

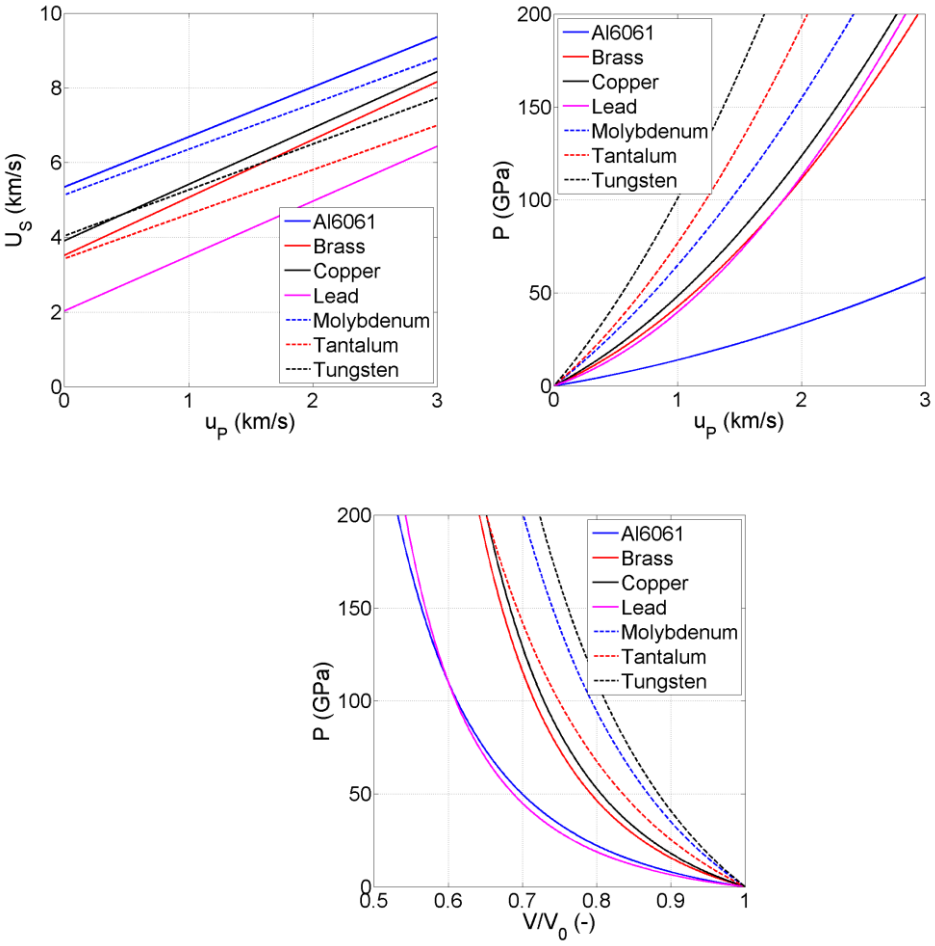

Fig. 2.4: Shock speed vs. particle velocity, pressure vs. particle velocity and pressure vs. relative volume curves for various materials.

2.3.2 Sound, particle and signal speeds

The objective of this section is to describe the relation between sound, particle and signal speeds, which leads to the formation of a shock front. First of all it is necessary to make some considerations about the reference system. In Fig. 2.5, the quantities of interest (particle velocity, sound speed and signal speed) are reported both in accordance with an external fixed observer and an observer fixed to the material.

In the first case, the discontinuity moves to the velocity U_S, the particle moves to u_{P1} in the shocked material and u_{P0}=0 in the undisturbed one and the pressure information moves to c_1+ u_{P1} in the shocked materials and c_0 in the undisturbed one (where c_1 and c_0 are, respectively, the sound speed in the shocked and undisturbed material). In the reference system of the material, some distinctions have to be done for the undisturbed or shocked material. From the shocked material point of view, the discontinuity moves to U_S- u_{P1}, while the pressure information inside the material moves to c_1. From the undisturbed material point of view, which is at rest at the initial condition, the discontinuity moves to U_S, while the pressure information inside the material moves to c_0.

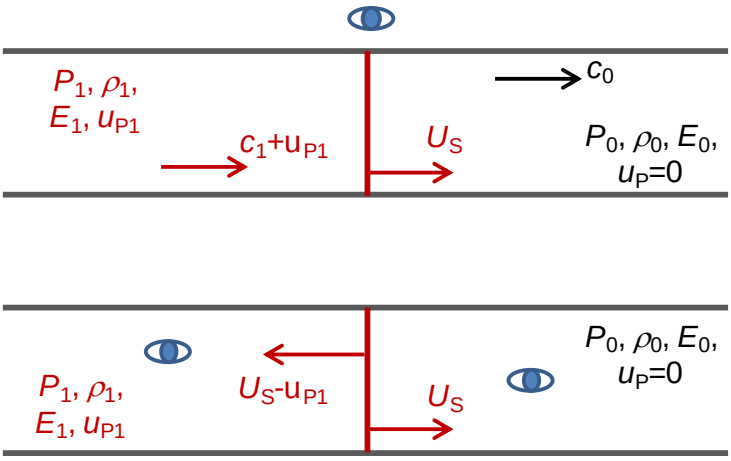

Fig. 2.5: Sound, particle and signal speed in an external fixed reference system (top) and in material reference system (bottom).

The relation between particle velocity, sound speed and signal speed can be found by looking at the problem from the material point of view. The objective is to compare the sound speed with the shock speed in reference to the particle velocity, both in the case of shocked and undisturbed material. The sound speed can be calculated starting from Eq. 2.10 or 2.11 and evaluating it in conditions 0 and 1.

$$c_0 = v_0\sqrt{-\left.\frac{\mathrm{d}P}{\mathrm{d}v}\right|_{v=v_0}} \qquad c_1 = v_1\sqrt{-\left.\frac{\mathrm{d}P}{\mathrm{d}v}\right|_{v=v_1}} \tag{2.21}$$

The shock speed in reference to particle velocity can be derived combining Eq. 2.13 and 2.14:

$$\begin{aligned} U_S - u_{P0} &= U_S = v_0 \sqrt{\frac{P_1 - P_0}{v_0 - v_1}} \\ U_S - u_{P1} &= v_1 \sqrt{\frac{P_1 - P_0}{v_0 - v_1}} \end{aligned} \tag{2.22}$$

As it can be easily noticed, the argument of the square root coincides with the slope of the Rayleigh line, which defines the shock transition. For any function which satisfies the condition of Eq. 2.12, the slope of the tangent line between two points satisfies the inequality:

$$\begin{aligned} \sqrt{-\left.\frac{\mathrm{d}P}{\mathrm{d}v}\right|_{v=v_0}} &< \sqrt{\frac{P_1 - P_0}{v_0 - v_1}} \\ \sqrt{-\left.\frac{\mathrm{d}P}{\mathrm{d}v}\right|_{v=v1}} &> \sqrt{\frac{P_1 - P_0}{v_0 - v_1}} \end{aligned} \tag{2.23}$$

This means that no signals move ahead the shock front. In this case the shock front is supersonic relative to the undisturbed material. Otherwise, in the case of shocked material, the sound speed is higher than the signal speed (U_S-u_P). This means that any disturbance can catch the shock front from behind. In this case the shock front is subsonic relative to the shocked material. This explains some of the statements made in the previous paragraphs, during the qualitative description of the problem of the gas in the tube.

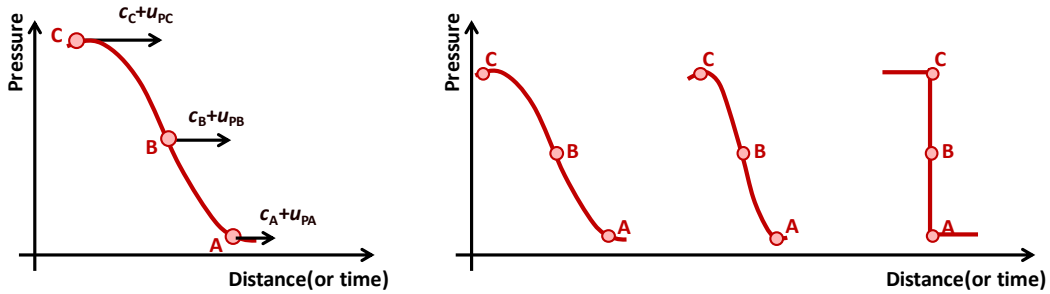

Fig. 2.6: Explanation of the formation of a shock front starting from a wave beyond the elastic limit.

As a matter of fact, an important consequence of this is that a shock front is spontaneously generated starting from a quite smooth signal moving with a U_S velocity

(external reference system), in accordance with what reported in the scheme of Fig. 2.6. Similar considerations on the unloading from a shock, lead to the generation of a rarefaction wave which reduces its slope while it travels and can overtake the shock.

For the purpose of verifying all the above considerations, the easier way is to consider an EOS linear in density defined as:

$$P(\rho) = K\left(\frac{\rho}{\rho_0} - 1\right) \tag{2.24}$$

or otherwise, as a hyperbolic function of the specific volume:

$$P(v) = K\left(\frac{v_0}{v} - 1\right) \tag{2.25}$$

Applying the definition of sound speed (Eq. 2.10 or 2.11) it can be found that the sound speed is constant and equal to:

$$c_0 = c_1 = \sqrt{\frac{K}{\rho_0}} \tag{2.26}$$

The calculation (Eq. 2.22) of the shock speed relative to the material velocity gives:

$$\begin{aligned} U_S &= \sqrt{\frac{\rho_1}{\rho_0^2}K} \\ U_S - u_{P1} &= \sqrt{\frac{K}{\rho_1}} \end{aligned} \tag{2.27}$$

Comparing the Eq. 2.26 with the Eq. 2.27, it is possible to conclude that the inequalities 2.23 are satisfied.

2.3.2.1 Numerical models

Simple numerical models are developed in LS-DYNA [5] with the aim of reproducing the shock features and compare the results varying the EOS or the material loading condition.

The numerical model reproduces a long bar with the longitudinal axis aligned in the *x*

direction, which is the direction of the wave propagation. The geometry is modelled with shell elements in a plane strain state. The uniaxial strain condition is obtained fixing the external node in *y* direction: in this way the lateral deformation is prevented. A trapezoidal velocity profile is imposed to a piston, which impacts against the material (see Fig. 2.7). Two different maximum velocities are investigated: 30 m/s and 300 m/s.

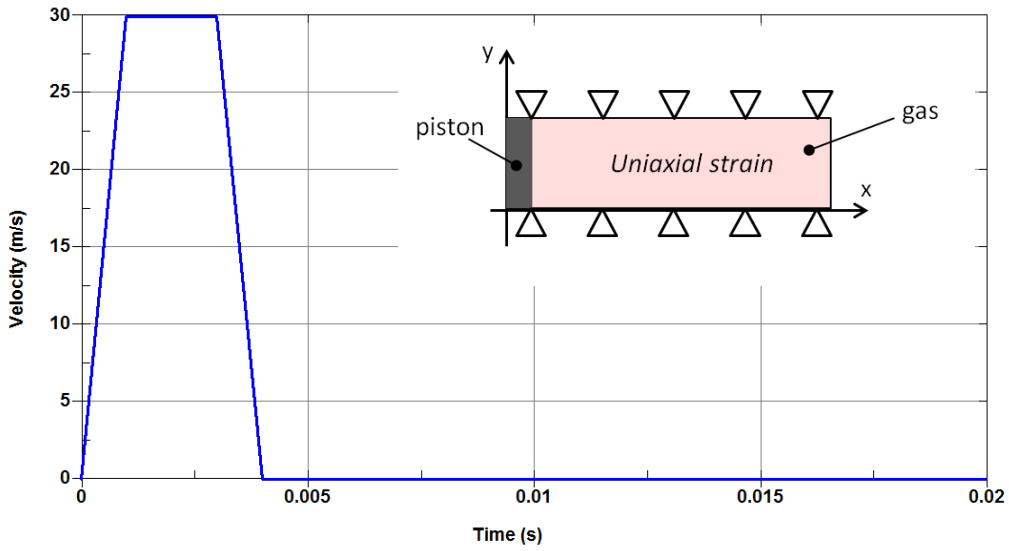

Fig. 2.7: Scheme of the 2D lagrangian model in uniaxial strain state; velocity profile (m/s) impressed to the piston in function of time (s).

The material is modelled like a fluid (*MAT_NULL) and a linear EOS in density is used to model the hydrodynamic behaviour of the material (*EOS_LINEAR_POLYNOMIAL). In Fig. 2.8 the pressure vs. time curves for two elements situated at different *x* coordinates are reported for the velocity equal to 30 m/s. This velocity implies a generation of about 1 GPa in pressure and this is not sufficient for a spontaneously generation of shock-wave. Obviously, if a more discontinuous initial velocity profile is assigned, also in case of low velocity, the generated shock front propagates.

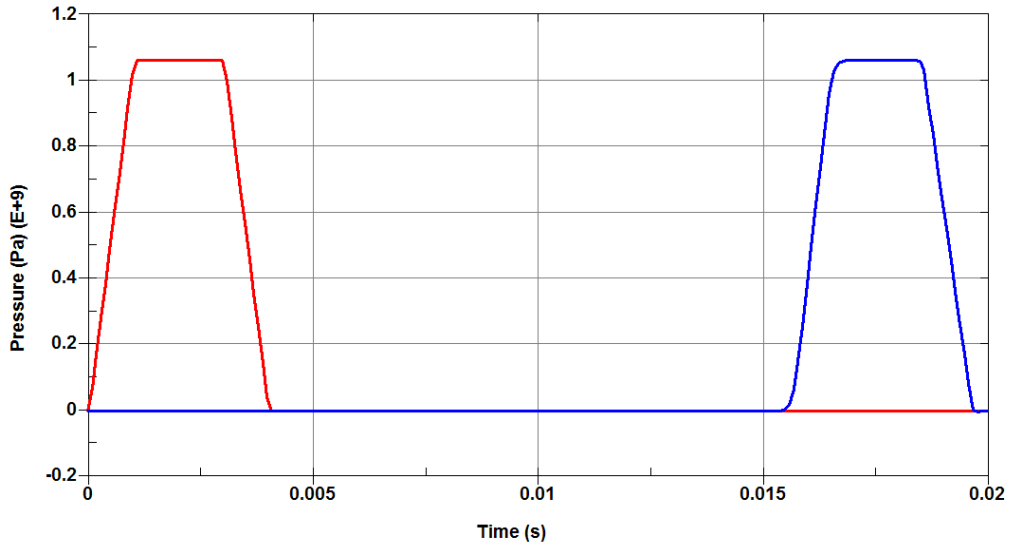

Fig. 2.8: Pressure vs. time history obtained in case of linear EOS and no shear strength material for a trapezoidal velocity profile (30 m/s).

In Fig. 2.9 the same results is reported for the case in which the velocity is 300 m/s (one order of magnitude more than before). In this case the correspondent pressure is about 11 GPa and it is sufficient for the spontaneous generation of a shock-wave. As a matter of fact, comparing the pressure profiles of two elements (the same of the previous case), it is possible to notice that, in the element far from the loaded surface, the pressure front is steeper, while the rarefaction wave (generated at the end of the shock) has a lower slope and starts to overtake the shock, reducing its duration. It is important to notice that even if a shock is generated inside the material, once finished, the material returns in the initial undisturbed condition. In Fig. 2.9 it is possible to observe that the pressure profile once the shock is generated is in accordance with the qualitative profile reported in Fig. 2.2 (left).

In Fig. 2.10 the pressure vs. longitudinal coordinate is reported. This diagram is obtained starting from the pressure vs. time profile for a set of elements. Again, the obtained result reproduces the anticipated behaviour of Fig. 2.2 (right).

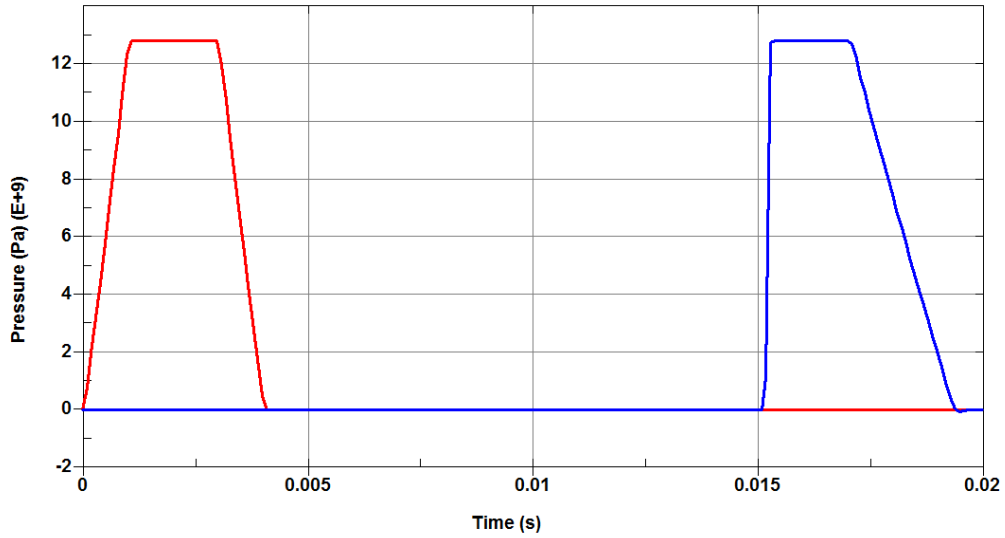

Fig. 2.9: Pressure vs. time history obtained in case of linear EOS and no shear strength material for a trapezoidal velocity profile (300 m/s).

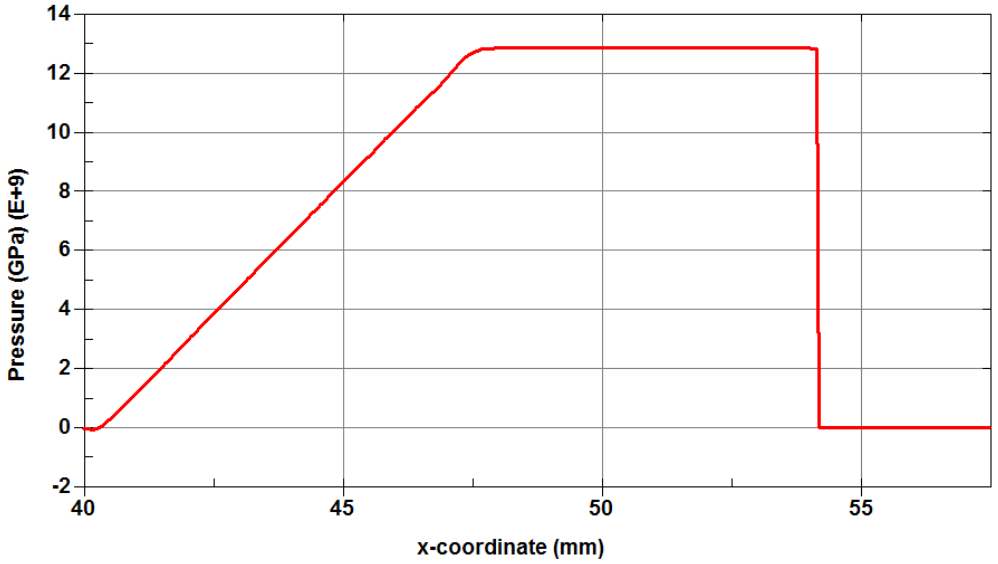

Fig. 2.10: Pressure vs. longitudinal coordinate obtained in case of linear EOS and no shear strength material for a trapezoidal velocity profile (300 m/s). The diagram is obtained at 15 ms after the impact.

2.4 Shock in solids

Usually, the material response in the stress-strain plane for solids assumes the form reported in Fig. 2.11, in which the mechanical behaviour of the material is reported for elastic and plastic regimes. In this case the material is subjected to a uniaxial stress state.

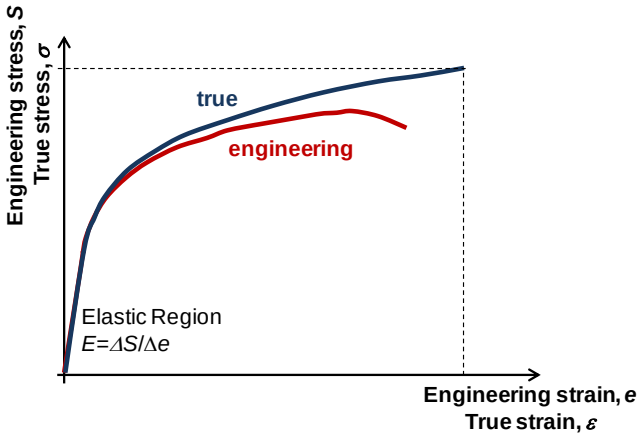

Fig. 2.11: Stress vs. strain curve in uniaxial stress state.

When the material is subjected to shock loading conditions, the usual approach for the estimation of the mechanical response is no longer valid. This implies that parameters, such as the elastic modulus, the yield stress or the elongation at failure, are no longer suitable. As a matter of fact, usually, during an impact the material is not in a uniaxial stress state, as in case for example of standard tensile or compression tests (see Fig. 2.11), but in uniaxial strain state. This can be easily explained thinking to a mechanical impact: the material is allowed to deform only in the impact direction. Otherwise, in the orthogonal direction the deformation is prevented (or limited) by the inertia.

Under these hypothesis, the only principal strain non equal to zero is that in the impact direction, $\varepsilon_1 = \varepsilon_{1e} + \varepsilon_{1p}$ and, since $\varepsilon_2 = \varepsilon_3 = 0$, this means that $\varepsilon_{2e} = -\varepsilon_{2p}$ and $\varepsilon_{3e} = -\varepsilon_{3e}$. Using the elastic relation of Eq. 2.3 between strain and stress and supposing that in plastic regime the material is incompressible ($\varepsilon_{1p} + \varepsilon_{2p} + \varepsilon_{3p} = 0$, $\upsilon = 0.5$), the expression of the total strain in the impact direction becomes:

$$\varepsilon_1 = \frac{\sigma_1(1-2\upsilon)}{E} + \frac{2\sigma_2(1-2\upsilon)}{E} \tag{2.28}$$

Considering an elastic-perfectly plastic material, the Tresca yield criterion is applied: $\sigma_1 - \sigma_2 = \sigma_0$, where σ_0 is the yield stress in uniaxial stress state, which can also be function

of plastic work. The principal stress in the impact direction is:

$$\sigma_1 = \frac{E}{3(1-2\upsilon)}\varepsilon_1 + \frac{2}{3}Y_0 = K\varepsilon_1 + \frac{2}{3}Y_0 \tag{2.29}$$

in which K is the bulk modulus.

In the elastic regime, $\varepsilon_1 = \varepsilon_{1e}$ and all the other strains are equal to 0. Following the same procedure used before, the elastic principal strain in the impact direction is:

$$\varepsilon_1 = \frac{\sigma_1}{E} - \frac{2\upsilon^2}{E(1-\upsilon)}\sigma_1 \tag{2.30}$$

and the principal stress is:

$$\sigma_1 = \frac{(1-\upsilon)}{(1-2\upsilon)(1+\upsilon)}E\varepsilon_1 \tag{2.31}$$

Comparing the slope of the elastic behaviour in uniaxial strain state with the slope in the case of uniaxial stress state (which is equal to E), it is evident that the slope of the elastic response of a material subjected to an impact is greater. The point at the transition between elastic and plastic region is Y_0 in case of uniaxial stress state. In case of uniaxial strain state it is the σ_{HEL}, Hugoniot Elastic Limit. Comparing the expression for the strain in elastic and plastic regime, it is possible to find the value of the stress at the interface between the two regimes, which is:

$$\sigma_{HEL} = \frac{(1-\upsilon)}{(1-2\upsilon)}\sigma_0 \tag{2.32}$$

Since $1-\upsilon$ is greater than $1-2\upsilon$, then $\sigma_{HEL} > \sigma_0$.

The general curve reported in Fig. 2.11 is then transformed into those of Figs. 2.12 and 13, in which the quantities of interest, such as the slope of the elasto-plastic curve and the yielding point, are reported. The curves labelled as “hydrostat” represents the mechanical response of the same material, neglecting its strength in case of hydrodynamic loading condition. Depending on the formulation of the EOS, different behaviours can be obtained. The first case (Fig. 2.12) implies a linear EOS combined with a piecewise elasto-plastic material (E_t is the tangent modulus). If the material remains in the elastic

domain (the applied stress is lower than the σ_{HEL}), then a single wave is generated in the material, which travel with a constant sound speed. If the stress exceeds the σ_{HEL}, the material starts to behave like a fluid. The curve "hydrostat" is parallel to the uniaxial strain curve and the distance between the two curves is $2\sigma_0/3$. In case of very high pressure (or stress), the difference can be neglected: the material can be approximated to a fluid without strength. The speeds of sound in the plastic domain are constant, both in uniaxial strain and stress states, and are equal to:

$$c_{pl} = \sqrt{\frac{E_t}{\rho_0}} \quad \text{uniaxial stress}$$
$$c_{pl} = \sqrt{\frac{K + \frac{4}{3}G_t}{\rho_0}} \approx \sqrt{\frac{K}{\rho_0}} \quad \text{uniaxial strain} \tag{2.33}$$

where $E_t << E$ and $G_t << K$. Comparing the expressions of Eq. 2.33 with the respective expressions in the elastic domain (Eq. 9), it is possible to conclude that the speed of plastic waves is less than the speed of elastic waves. This means that if the σ_{HEL} is exceeded, two separated wave fronts are developed.

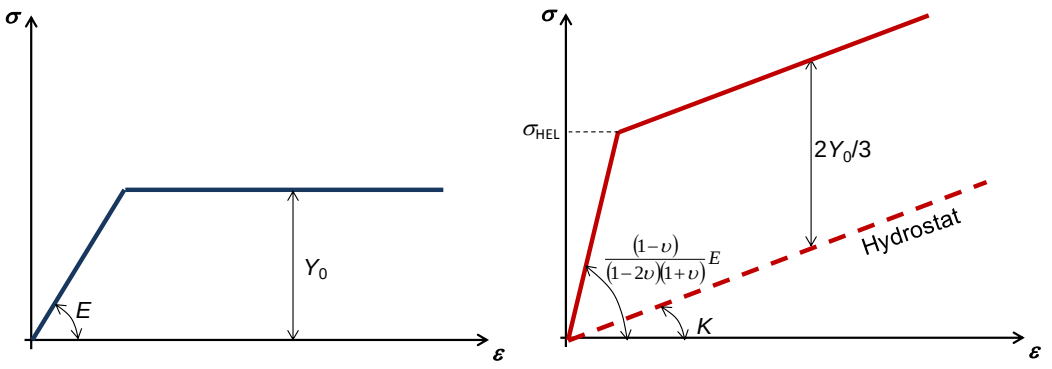

Fig. 2.12: Stress vs. strain curve in case of uniaxial stress for a linear piecewise material (left); stress vs. strain curve in case of uniaxial strain for an elastic-perfectly plastic material combined with a linear EOS (right).

In Fig. 2.13, the case in which a non-linear stiffening EOS is combined with an elasto-plastic material is reported. As before, if the material remains in the elastic domain, a single wave is generated in the material, which travels with a constant sound speed. When the stress exceeds the σ_{HEL}, also plastic wave starts to move. In this case the plastic wave

velocity depends on the strain. Until the point C, the velocity of the plastic wave is less than that elastic precursor, so two different wave fronts propagate at the same time. In correspondence to the point C, the elastic and plastic waves have the same velocity. At even higher pressure, beyond the point D, a single plastic shock-wave propagates in the material with a high velocity (U_S) proportional to the slope of the stress-strain curve and is higher than the elastic precursor speed.

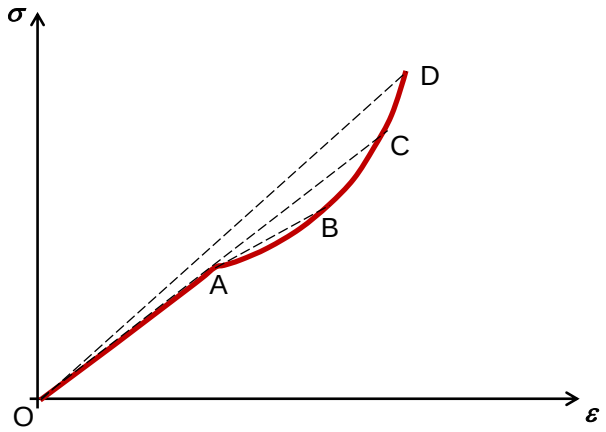

Fig. 2.13: Stress vs. strain curve in case of uniaxial strain state for an elasto-perfectly plastic material with a non-linear stiffening EOS.

The expected longitudinal stress σ_x vs. longitudinal strain ε_x (which is proportional to the specific volume) and σ_x vs. time t profiles, for the case in which the material condition remains under the point C, are reported in Fig. 2.14 [6]. Looking the σ_x vs. t profile (see Fig. 2.14.c) for a fixed longitudinal coordinate, it is possible to notice that two wave fronts are generated. Initially, there is only the elastic front, since its speed of propagation is higher and it limited by the σ_{HEL}. Then, at the time in which also the plastic front reaches that longitudinal coordinate, the two waves travel together in the material. At the end of the shock, the unloading process starts. The unloading process is elastic, so in the σ_x vs. ε_x plane it follows the slope of the elastic path (see Fig. 2.14.b). Initially, there is only the unloading of the elastic wave: the stress decrease of a quantity equal to σ_{HEL}. When the σ_x intercept the curve "hydrostat", it means that the material is subjected to a pure hydrostatic stress state and the equivalent stress goes to zero (see Fig. 2.14.a and b). As a matter of fact, the σ_x vs. ε_x diagram corresponds to the equivalent stress vs. strain (σ_{eq} vs. ε_{eq}, see Fig. 2.14.a) diagram with a superposition of the hydrostatic curve. When also the end of the plastic wave arrives, then the plastic wave starts the unloading (again elastically).

Since the hardening is considered to be isotropic and if in the material a sufficient energy was stored, during the unloading path the material could reached again the yield condition and plasticised again. In this condition, the maximum unloading corresponds to $2\sigma_{HEL}$, after that a second plastic wave front is generated. The final condition of the material, after the complete unloading, corresponds to have a σ_x=0 with residual ε_x, σ_{eq} and pressure P.

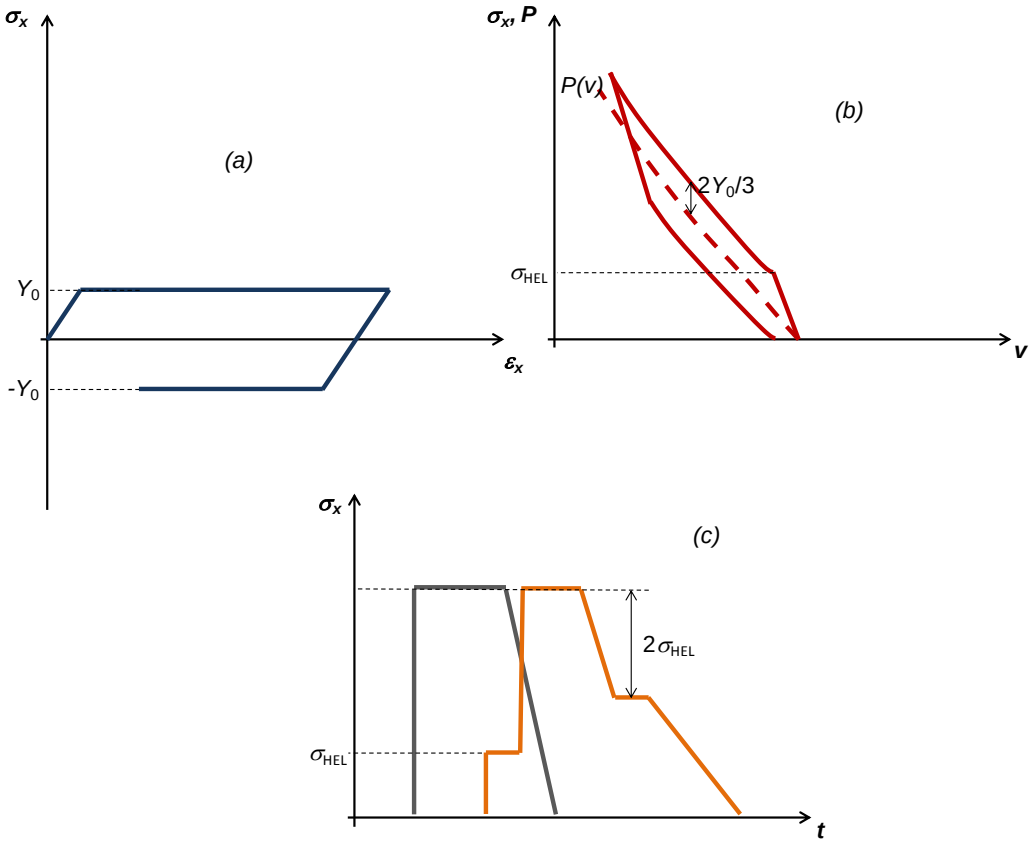

Fig. 2.14: Stress vs. strain diagram of an elastic-plastic body: (a) deviatoric equivalent stress vs. equivalent strain; (b) longitudinal stress (or pressure) vs. longitudinal strain (or volume); (c) longitudinal stress vs. time.

2.4.1 Numerical models

As previously made for the case of shock propagation in fluids, also in case of solids, some simple numerical models are developed in order to verify the phenomena evolution.

The numerical model (see Fig. 2.15) reproduces a planar impact, as in a flyer impact test. In more details, a thin disk, named *projectile*, is launched against another disk, named *target*, which is the specimen and is at rest before the impact. Since the diameter is much

greater with respect to the thickness, the only deformation allowed during the impact is that in the thickness direction (*x*-direction). The geometry is modelled with shell elements in a plane strain state. The uniaxial condition is obtained fixing the external node in y direction: in this way the lateral deformation is prevented. Four different impact velocities are investigated: 3, 30, 300 and 3000 m/s. The impact between the target and the projectile generates in the sample a rectangular pressure profile: the discontinuity is imposed to the medium by the load. This is also similar to what happens, for example, in case of detonation of a high content of explosive, which suddenly releases the energy on the material.

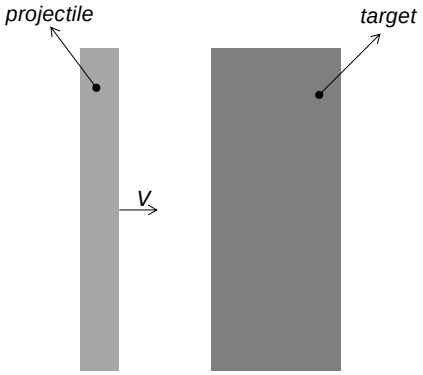

Fig. 2.15: Numerical model of a flyer impact test.

The material strength is described with a linear elasto-plastic model (*MAT_ELASTO_PLASTIC_HYDRO) imposing an isotropic hardening. A linear EOS in density is used to model the hydrodynamic behaviour of the material (*EOS_POLYNOMIAL).

2.4.1.1 Case 1: impact velocity of 3 m/s

In Fig. 2.16 the σ_x vs. *t* curve is reported: since the σ_x stress does not exceed the σ_{HEL} of the material, the material remains in the elastic domain and a single front is generated.

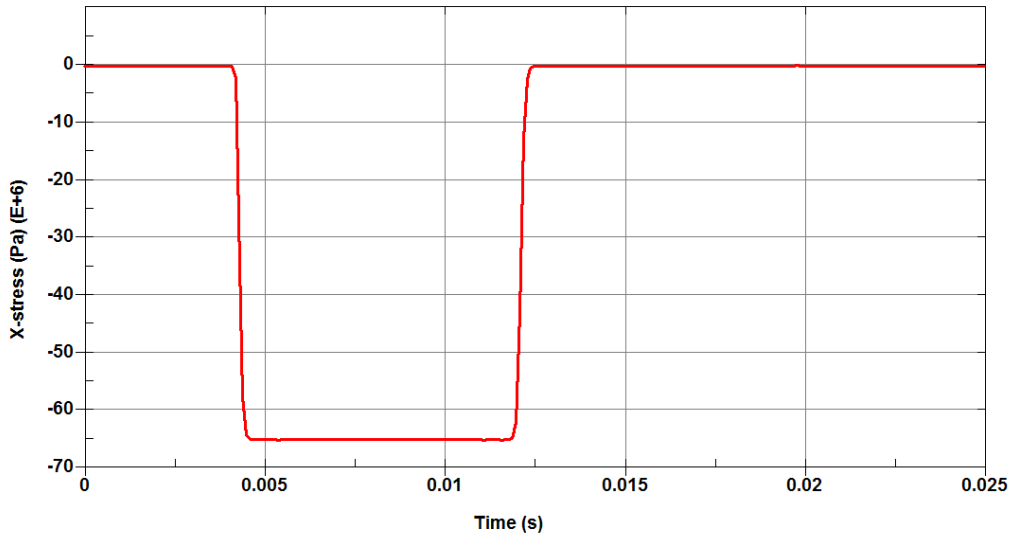

Fig. 2.16: Longitudinal stress vs. time for a fixed longitudinal coordinate (impact velocity of 3 m/s): a single elastic front is generated.

2.4.1.3 Case 2: impact velocity of 30 m/s

In case of 30 m/s impact velocity, the σ_x stress exceeds the σ_{HEL}, so there are two different fronts and plastic deformation occurs.

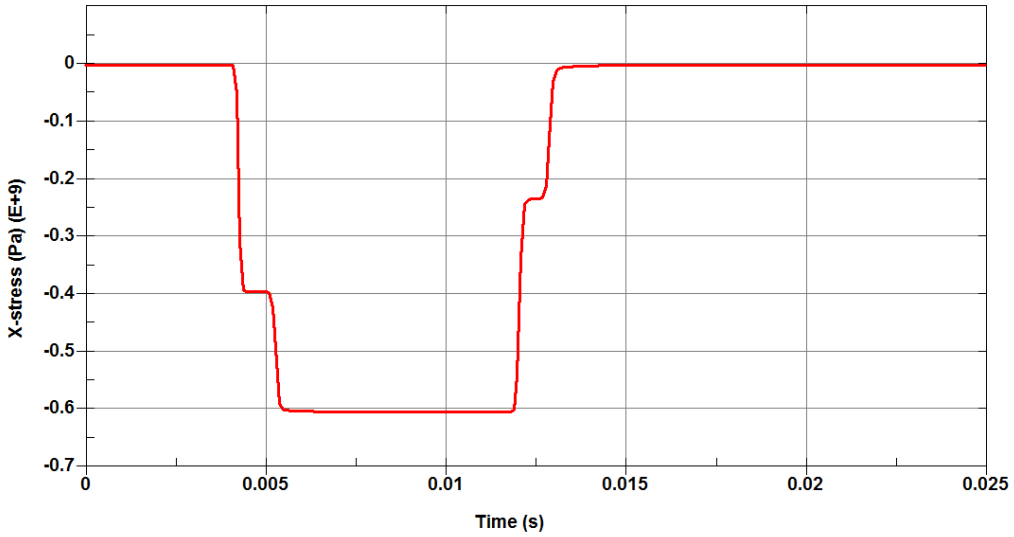

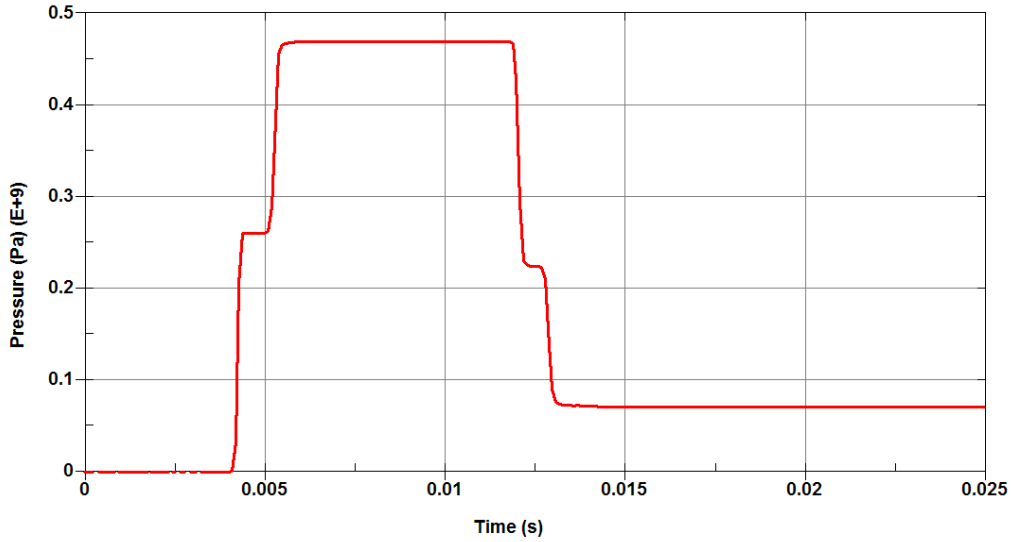

Fig. 2.17: Longitudinal stress vs. time (top) and pressure vs. time (bottom) for a fixed longitudinal coordinate (impact velocity of 30 m/s): two separated wave fronts are generated.

The final value of σ_x is less than two times the σ_{HEL}, so during the unloading the material reaches the σ_x=0 condition before exceeding again the σ_{HEL}. This implies that no plastic deformation occurs during the unloading (see Fig. 2.18), but the material yields only during the loading phase. Looking the results in the σ_x vs. ε_x plane, reported in Fig. 2.19, it is possible to follow the loading and unloading path. At the end of the unloading process, residual plastic deformation remains in the material, in which both pressure and equivalent stress are not equal to zero. In Figs. 2.17-2.19 the results are reported only for one element of the target for sake of clarity.

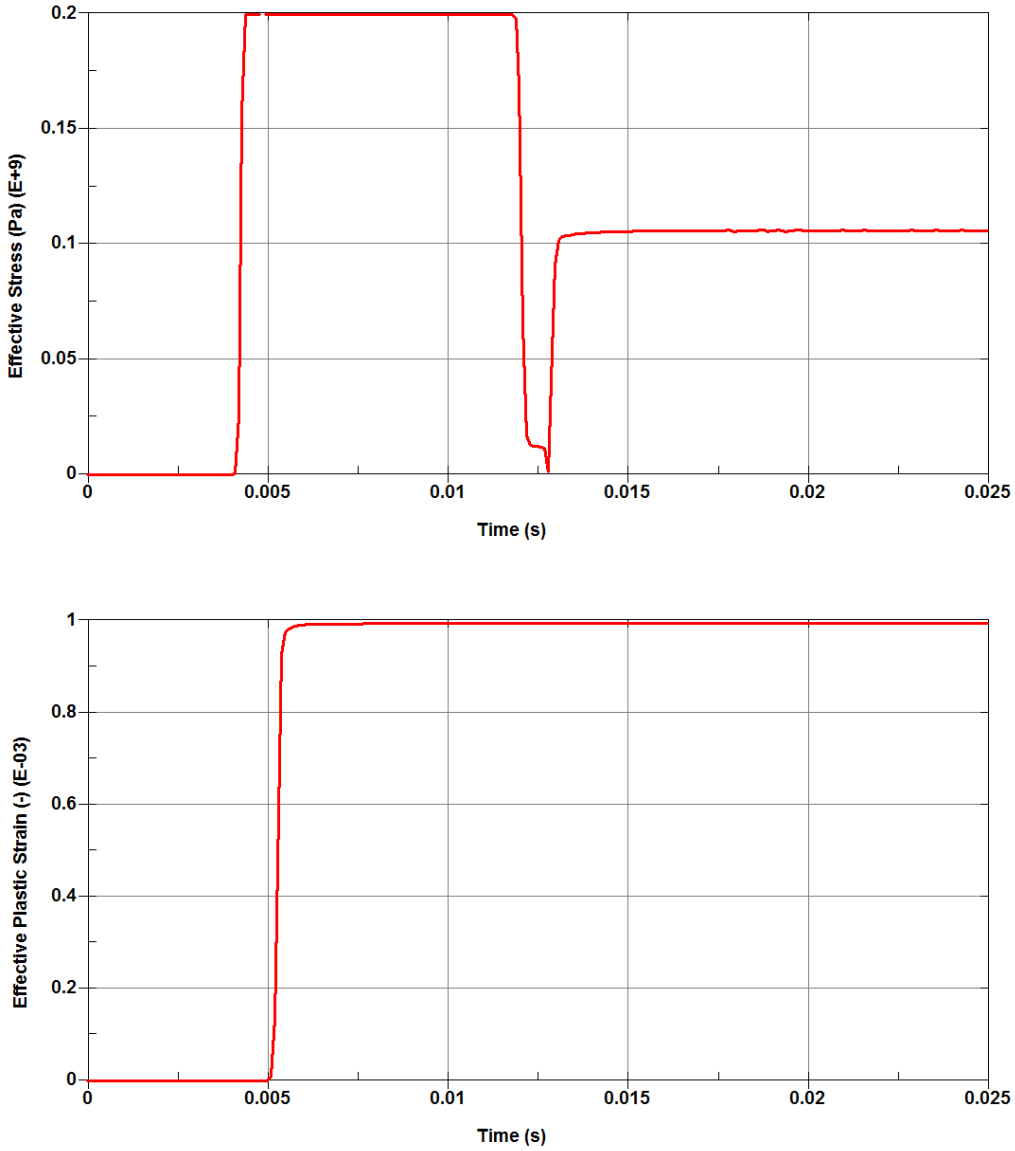

Fig. 2.18: Von Mises stress vs. time (top) and equivalent plastic strain vs. time (bottom) for a fixed longitudinal coordinate (impact velocity of 30 m/s): the material reach only during the loading phase the yielding condition.

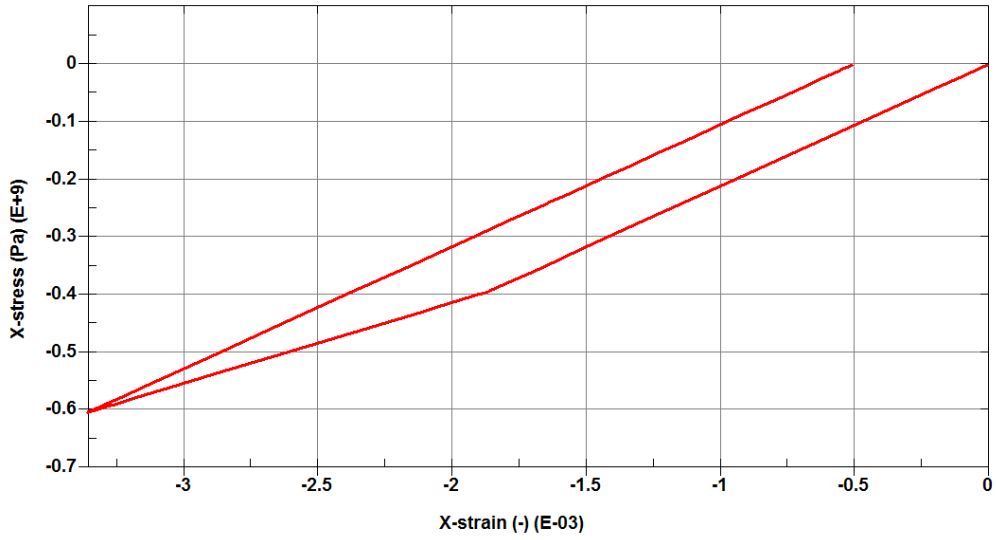

Fig. 2.19: Longitudinal stress vs. longitudinal strain for a fixed longitudinal coordinate (impact velocity of 30 m/s): loading and unloading paths.

2.4.1.3 Case 3: impact velocity of 300 m/s

In case of 300 m/s impact velocity, the σ_x stress exceeds the σ_{HEL}, so there are two different fronts and plastic deformation occurs. The final value of σ_x is greater than two times the σ_{HEL}, so during the unloading the material reaches again the yielding condition. This implies that another plastic wave is generated and the material yields a second time.

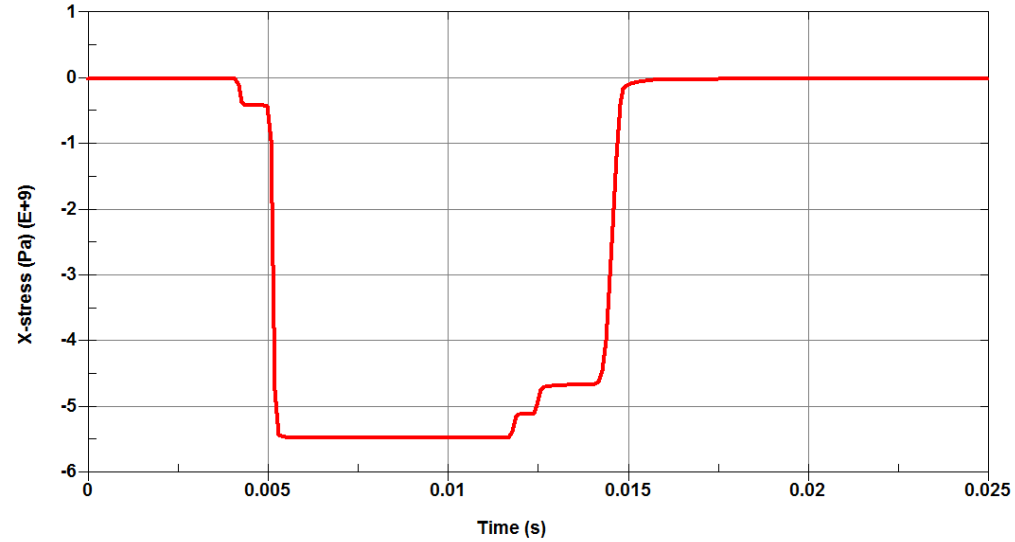

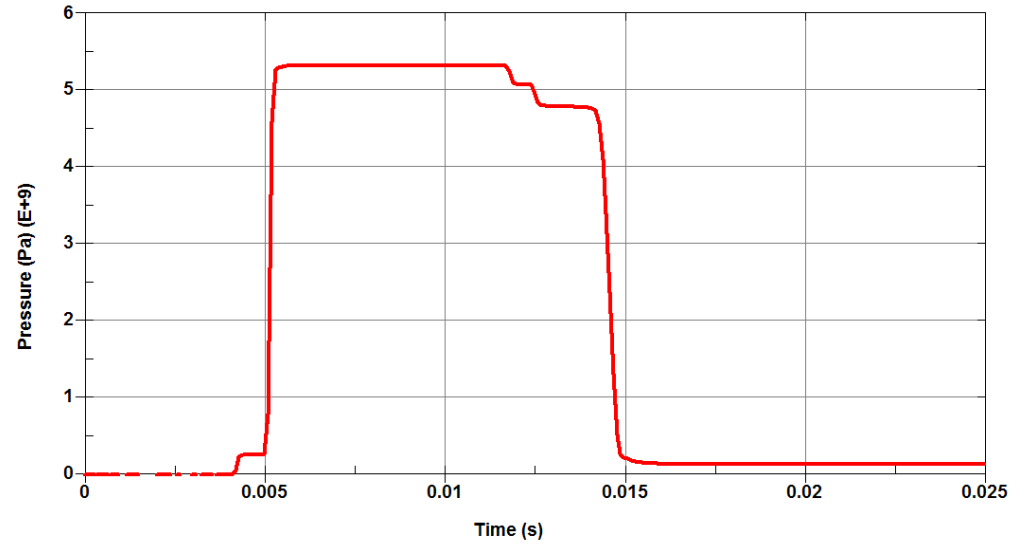

Fig. 2.20: Longitudinal stress vs. time (top) and pressure vs. time (bottom) for a fixed longitudinal coordinate (impact velocity of 300 m/s): two separated wave fronts are generated.

Looking the results in the σ_x vs. ε_x plane, reported in Fig. 2.19, it is possible to follow the loading and unloading path. As for the previous case, at the end of the unloading process, residual plastic deformation remains in the material, in which both pressure and equivalent stress are not equal to zero. In more details, the equivalent stress (Von Mises stress) is limited by the yielding.

In Figs. 2.20-2.22 the results are reported only for one element of the target for sake of clarity.

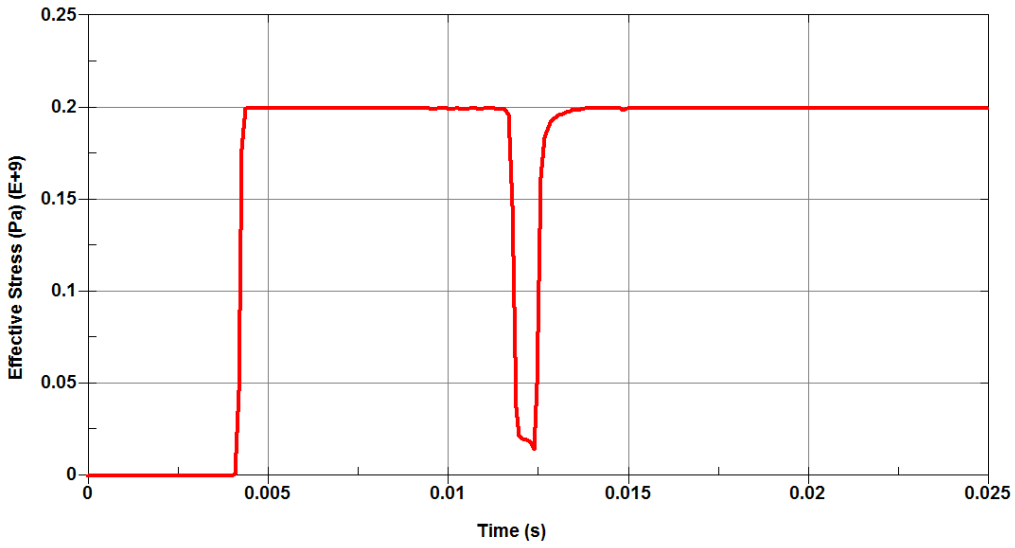

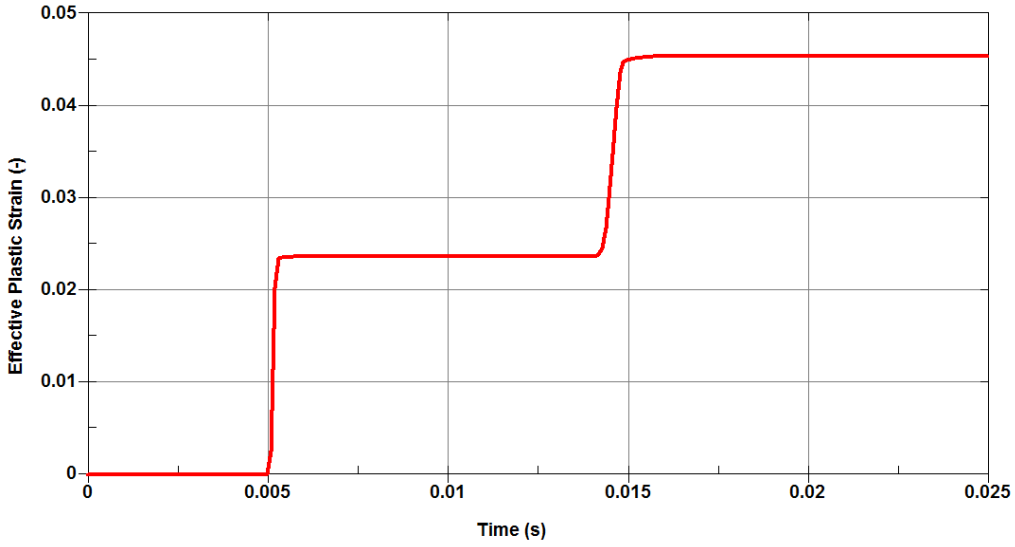

Fig. 2.21: Von Mises stress vs. time (top) and equivalent plastic strain vs. time (bottom) for a fixed longitudinal coordinate (impact velocity of 300 m/s): the material reaches, both during loading and unloading phases, the yielding condition.

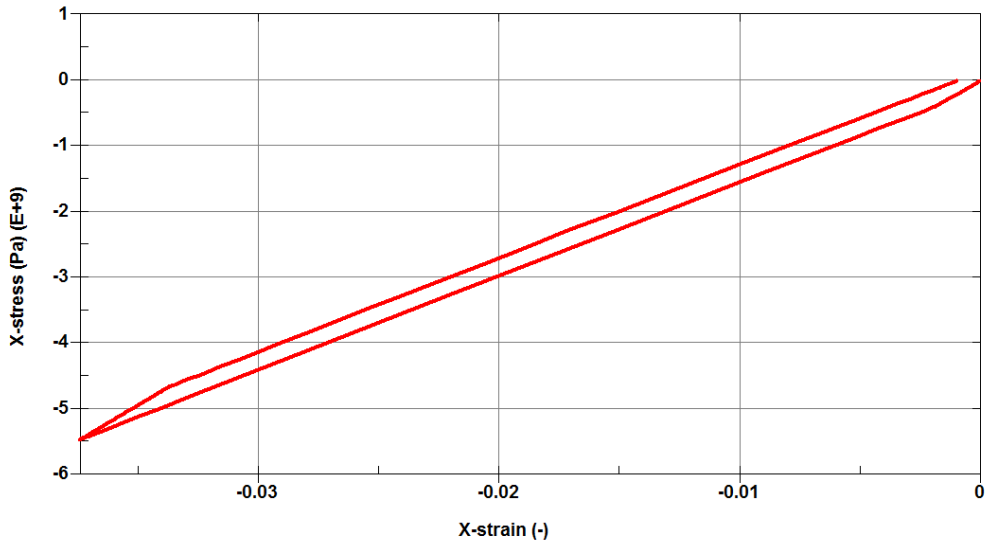

Fig. 2.22: Longitudinal stress vs. longitudinal strain for a fixed longitudinal coordinate (impact velocity of 300 m/s): loading and unloading paths.

2.4.1.4 Case 4: impact velocity of 3000 m/s

The idea is to reproduce a so high velocity impact that the material exceeds the point C of Fig. 2.13. In this case a single shock front is generated. In order to obtain this condition,

it is necessary to modify the numerical model introducing a non-linear stiffening EOS (*EOS_GRUNEISEN). In Fig. 2.23 the pressure vs. time history is reported, in which it is possible to notice the steepen shock front followed by the rarefaction wave. As for the case before, The material plasticize twice: during both the loading and the unloading phases and, at the end of the unloading, residual plastic strain remains in the material, combined with residual pressure and Von Mises stress (limited by the yielding.

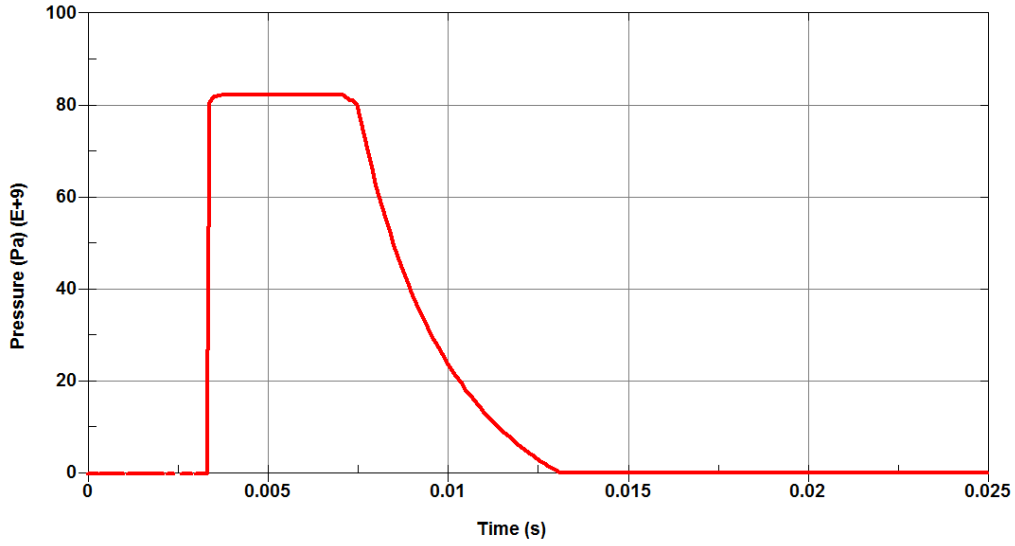

Fig. 2.23: Pressure vs. time for a fixed longitudinal coordinate (impact velocity of 3000 m/s): a single shock front is generated.

2.5 Cylindrical wave

The considerations obtained in the previous paragraphs are intended to be applicable in case of plane wave. In this paragraph the case of waves propagation in a cylindrical geometry along the radius is analyzed [6-10]. Starting from the equilibrium in radial direction of a portion of the cylinder, the wave equation in the elastic domain is:

$$\frac{\partial^2 u}{\partial r^2} + \frac{\partial}{\partial r}\left(\frac{u}{r}\right) = \frac{1}{c^2}\frac{\partial^2 u}{\partial t^2} \tag{2.34}$$

which is equivalent to the partial differential equation of Eq. 2.8 obtained for the case of plane wave. The value of the constant c is:

$$c = \sqrt{\frac{E}{\left(1-\upsilon^2\right)\rho_0}} \quad \text{plane stress}$$
$$c = \sqrt{\frac{E\left(1-\upsilon\right)}{\left(1-\upsilon-2\upsilon^2\right)\rho_0}} \quad \text{plane strain} \tag{2.35}$$

In case of cylindrical waves, the amplitude of the shock decreases with the radius and, in particular, the decrement is proportional to $1/\sqrt{r}$, where r is the radius. As in case of planar waves, since the shock front is subsonic with respect to the material behind, the end of the shock can catch the front and reduce furthermore its amplitude. In contrast with the case of planar wave, in case of cylindrical wave, behind the shock front there is always a negative pressure state (positive hydrostatic stress), which follows the rarefaction wave. In Fig. 2.2 it is possible to notice that when the shock is finished, the material return to the undisturbed condition. This is correlated to the fact that each section of material is moved in the propagation direction parallel to each other.

On the contrary in case of cylindrical geometry, due to the constraint introduced by the axisymmetry, the material is moved toward higher radii. Since the pressure can become negative, this implies that also if the shock compresses the material, it is necessary to have an EOS, which is well defined also in tension. In case of planar wave, this requirement is also needed, but only if the wave is reflected by a free surface. The fact that the material does not return in the undisturbed condition implies that not only the pressure is not zero after the shock, but also that particle velocity and density do not return to the initial values. In particular the material is subjected to a reduction in density, which can lead to substantially change in state of the matter. For this reasons, a multi-phase EOS is needed. If the shock amplitude is moderate, the change in density remains limited: the material is still solid and can support tensile load. When the shock is very strong, the consequent change in density can be significant and the material is not still solid. In this case, it is no longer able to support hydrostatic tensile load and its contribution in terms of pressure becomes null. All the considerations made for the case of cylindrical shock wave propagation, will be useful for the comprehension of the phenomenon evolution in case of high energy particle beam interaction with solid material, discussed in the chapters 5-7.

2.5.1 Numerical models

As performed before to reproduce planar wave propagation in hydrodynamic and elasto-plastic materials, also for the cylindrical wave propagation simple numerical models are constructed.

For simplicity the case analyzed is that of hydrodynamic material (*MAT_NULL and *EOS_POLINOMIAL), in which the material strength is set to zero. The model used is similar of that proposed in the paragraph 2.3.2. The scheme of the model and the initial velocity profile are reported in Fig. 2.24. In the cylindrical model the material is modelled with shell element with an axisymmetric formulation. The piston is a ring to which an initial radial velocity is applied. The same model is also used with a plane strain formulation for the elements in order to be able to compare the results.

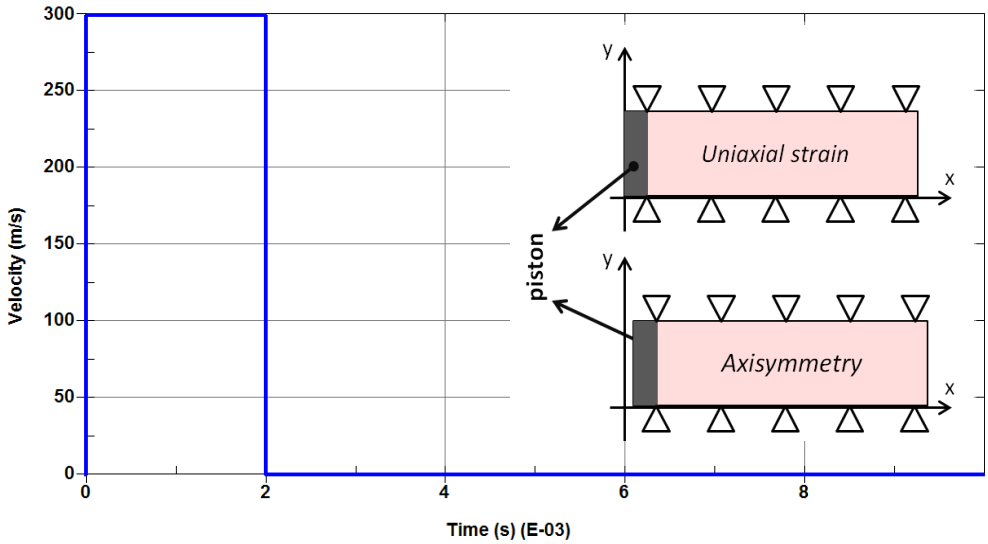

Fig. 2.24: Scheme of the 2D Lagrangian model in uniaxial strain and axisymmetric state; velocity profile impressed to the piston.

The pressure vs. time profile is shown for the same elements situated at different longitudinal (or radial) coordinates for the two cases. In case of planar wave it is possible to notice that the amplitude of the shock remains constant. If elements far from the piston are considered the amplitude is reduced since the end of the shock overtakes the front (it is not the case shown in Fig. 2.25). The pressure, at the end of the shock, returns to zero, as expected.

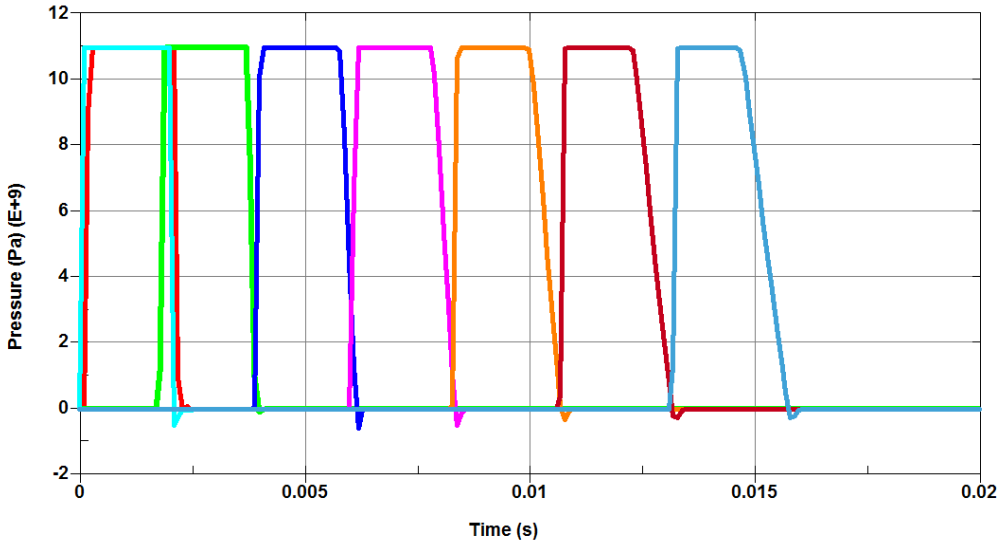

Fig. 2.25: Pressure vs. time curves for element situated at different longitudinal coordinates: uniaxial strain for planar wave.

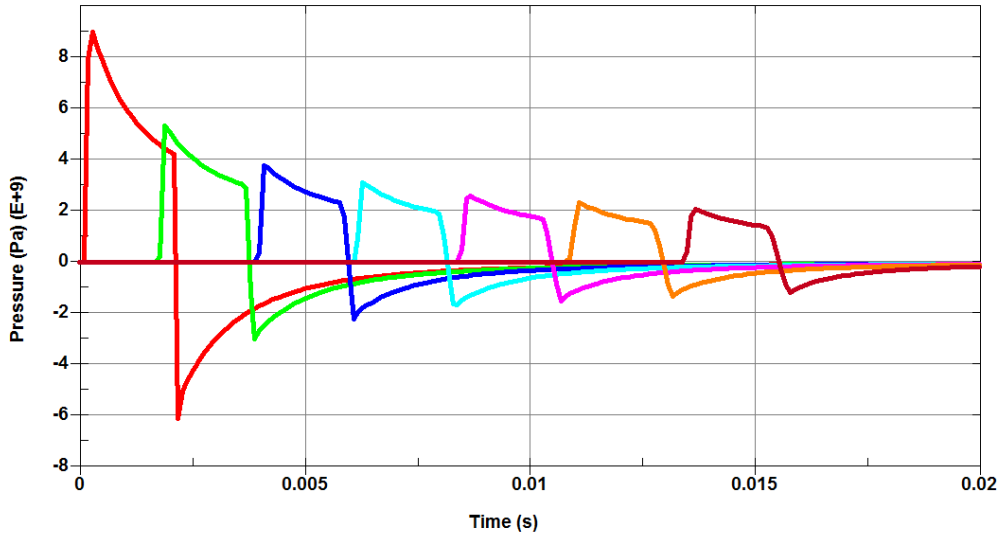

Fig. 2.26: Pressure vs. time curves for element situated at different longitudinal coordinates: uniaxial strain for cylindrical wave.

In Fig. 2.26 the same diagram is reported for the axisymmetric case. As it appears evident there is a strong reduction in the shock amplitude due to the fact that the elements are situated at increasing radii. At the end of the shock the pressure reaches negative values: if no limits are imposed, the material can reach high values of negative pressure. Otherwise, a spall model can be defined: e.g., the negative pressure can be limited

imposing that pressure lower than a threshold P_{min} (with $P_{min} < 0$) are not allowed, see chapter 4. In any case, it is important to remark that, always the material situated behind the shock front experiences hydrodynamic tensile load when the shock is finished.

References

[1] Zukas J. A., "High velocity impact dynamics", J. Wiley & Sons, New York (1990), ISBN 0471514446.

[2] Zukas J. A., "Introduction to hydrocodes", Elsevier Science & Technology (2004), ISBN 0080443486.

[3] Meyers M. A., "Dynamic behaviour of materials", J. Wiley & Sons (1994), ISBN 047158262.

[4] Marsh S. P., "LASL shock Hugoniot data", University of California Press (1990), ISBN 0520040074.

[5] Gladman B. et al., "LS-DYNA® Keyword User's Manual – Volume I – Version 971", LSTC (2007).

[6] Kanel G. I., Razorenov S.V. and Fortov V.E., "Shock -Wave Phenomena and the Properties of Condensed Matter", Springer (2004), ISBN 0387205721.

[7] Chou P.C. and Koening H.A., "Propagation of cylindrical and spherical elastic waves by method of characteristics", NASA technical note, NASA TN D-2644 (1965).

[8] Sievers P., "Elastic stress waves in matter due to rapid heating by an intense high-energy particle beam", CERN libraries, LAB.II/BT/74-2.

[9] Zheng J, et al., "Elastic stress waves of cylindrical rods subjected to rapid energy deposition", J. Mech. Eng. Sci., part C, **218**:359-368.

[10] Whitham G.B., "Linear and Nonlinear Waves", J. Wiley & Sons (1999), ISBN 0471359424.

3. Equation Of State

In this chapter, the concept of Equation Of State (EOS) is introduced, starting from the thermodynamic theory. The main characteristics of the EOS are described, in particular focusing the attention on the definitions, which are, usually, used for the implementation in the most part of the commercial FE and hydrodynamic codes. In the last part of the chapter, an overview of some EOS is reported, with reference to their formulation and the range of applicability. Finally, foe each EOS presented, the trend of the pressure is reported on the basis of the data available in literature. The hydrodynamic behaviour of different materials is compared, over a certain range of variation of the quantities of interest.

In the usual continuum mechanics treatment, the complete stress tensor, which describes the material condition state, is divided into two components: the deviatoric and the hydrostatic tensors. In high strain-rate and shock loading conditions, the choice of the material constitutive equations, which includes both strength model (deviatoric component) and equation of state (hydrodynamic component), is of fundamental importance. In this chapter the attention is focused on the hydrodynamic response of materials.

In impact, shock or generally high strain-rate regime, the material covers a wide range of different possible states. For example, some parts of the material can be subjected to high pressure and temperature and this implies that thermodynamic response prevails on mechanical one. In general, due to the rise in temperature, there is a modification in the material strength, which can be more or less important, depending on how much the material strength can be neglected. In addition also high pressure can influence the material response both in strength and hydrodynamic regime. On the other hand, other parts of material can remain in a low pressure condition, in which is not possible to neglect the mechanical strength, which becomes the dominant part of the material response.

The hydrostatic component of stress is associated to the pressure in the material, which is equal to the trace of the complete stress tensor. Besides, it is also a state variable of the thermodynamic problem. The thermodynamic problems, usually, are described via the definition of an Equation Of State (EOS), which expresses the relation between dependent thermodynamics variables (such as pressure P, internal energy E and entropy S) and independent ones (such as density ρ and temperature T). All these variables define the thermodynamic state of the matter.

3.1 Theoretical and fundamental aspects

The concept of energy is of fundamental importance in thermodynamics [1, 2]. The energy can assume a lot of forms (thermal, kinetics, potential, electric, magnetic, chemical and nuclear), whose sum is the total energy. In case of stationary regime system, during a transformation, the variation of the total energy corresponds to the variation of the internal energy, which is the sum of all the microscopic forms of energy.

The first thermodynamic law states that the energy of an isolated system is constant: the energy can be transferred to the system heating, compressing or adding mass or can be subtracted to the system cooling, expanding or removing mass. Considering an infinitesimal variation of the thermodynamic state, it derives that:

$$dE = \delta Q - \delta W = \delta Q - PdV \tag{3.1}$$

where δQ and δW are the infinitesimal increments of heat supplied to the system (positive) and work done by the system (positive), respectively. The same increment in energy dE can be obtained from different combinations in term of heat and work. The latter is equal to the pressure P multiplied by the variation of volume dV. The internal energy is not univocally defined, but depends from the integration constant, which defines the reference (arbitrary) state.

Starting from an initial state, if the work is done adiabatically (i.e. without any heat transfer) for a fixed quantity of work, the final state is independent on how the work is performed ($dE=dW^{ad}$). Obviously, if on or from an isolated system, no work is performed, the energy remains constant ($dE=0$). On the contrary, if the work is not adiabatic, it is not possible to asses that $dE=dW^{non\text{-}ad}$, since also the heat transfer has to be taken into account.

Some fundamental quantities for the definition of an EOS are related to the derivative

of the dependent variables, which have to satisfy some constraints (e.g. admissible range).

For the thermodynamic stability, the specific heat, defined as:

$$C_v = \left(\frac{\partial E}{\partial T} \right)_v \tag{3.2}$$

has to be positive and to go to infinity in correspondence to phase transitions, since they imply an energy variation at constant temperature (dT=0).

Another important quantity, which assures the mechanical stability, is related to the partial derivative of the pressure with respect to the density at constant temperature, which has to be positive or at least equal to zero in correspondence to phase transitions. Furthermore, this quantity is, also, related to the Bulk modulus of the material.

Otherwise, the partial derivative of the pressure respect to temperature at constant density can be positive or negative. In most cases, this quantity is positive, but for example it is not true during the transformation between water and ice. The density of the ice is lower compared to the density of water: this means that, if heat is transferred to ice along an isochoric transformation, the pressure is reduced.

For a thermodynamic system which is in equilibrium, the state of the system is completely defined if two independent and intensive (that means independent from the system dimensions) variables are known.

Usually, in hydrodynamics, the internal energy is used instead of temperature as independent variable. In this case, the EOS assumes the general form:

$$P = P(\rho, E) \tag{3.3}$$

An EOS represent a set of surfaces, on which it is possible to define one-dimensional paths, which identify isotherm, isobaric, isochoric, isentropic, etc. transformations. In order to obtain the entire surface it is necessary measuring a great number of paths, which can be followed on it.

When an object is subjected to impact, deformation at high strain-rate or high energy deposition, obviously it suffers large changes in it thermodynamic state. For this reason it is necessary to have a multi-phase EOS able to describe a great number of all the possible states of the matter. At extreme loading conditions, the material could be subjected to high-temperature and high-pressure conditions. In this sense, there are, e.g. the cases in which a great amount of energy is deposited in a very short time (order of a few

nanoseconds to a few hundred nanoseconds). Some examples are: deposition of x-ray energy from the detonation of nuclear explosives, high energy particle beams deposition, laser deposition, magnetic flux interaction, etc.

In such extreme conditions, generally, experimental studies are difficult and very expensive (see chapter 8). This limits the possibility to have experimental data in the corresponding range in terms of pressure, temperature and density.

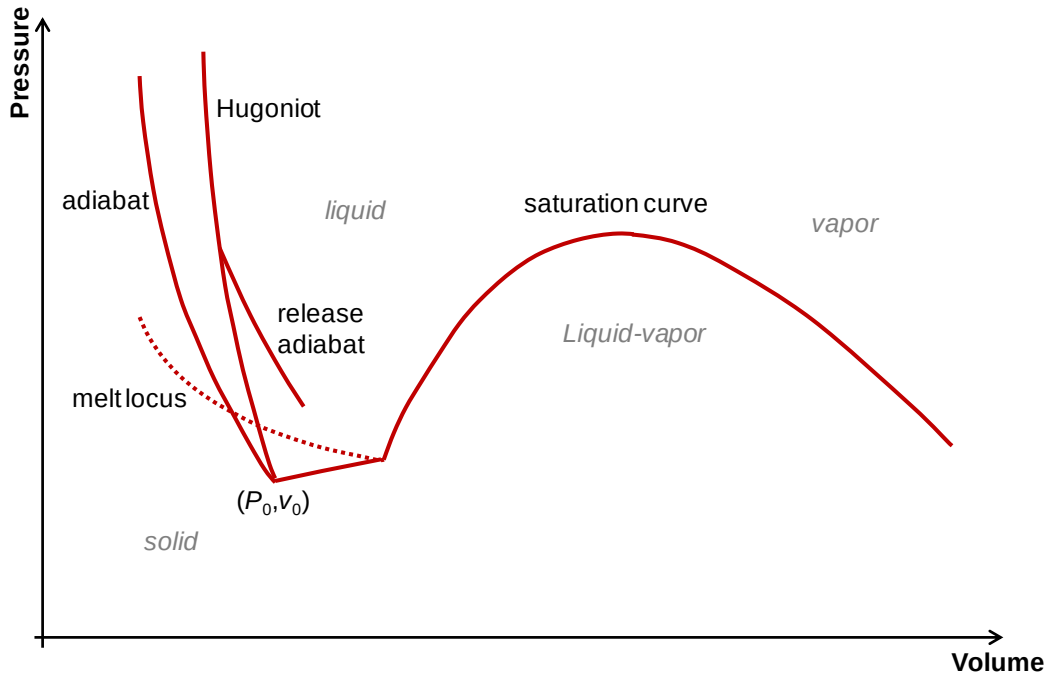

Fig. 3.1: Phase diagrams in the P-V plane: identification of adiabat and Hugoniot paths and different states of matter.

In accordance to this, an ideal EOS has to cover all regions in the P-ρ-E plane (see Fig. 3.1):

- ✓ solid phase;
- ✓ liquid phase (with data on melt locus where solids change to liquids);
- ✓ two-phase liquid-vapour coexisting region (with data on saturation curve);
- ✓ vapour region at high temperatures and expansions;
- ✓ plasma region.

The study of EOS under extreme conditions is an interdisciplinary subject, with

important applications to materials science, astrophysics, geophysics, nuclear physics, plasma physics and applied sciences such as fission, hypervelocity impact, etc. Important branches of physics were developed or originated from the equations of state, while in return more complex formulations of the EOS were due to the development of modern physics [2].

3.2 EOS in FEM

In this paragraph, the EOS is described taking into account the general formulation, which is used in the most part of the commercial FE codes. In particular, the attention is focused on formulations and expressions used in LS-DYNA [4].

In Table 3.1 are reported some of the quantities, which are of interest in the definition of the thermodynamic problem.

Table 3.1: Basic variables needed for the definition of the thermodynamic problem.

Quantity (Units)	**Expression**
Volume (m^3)	V
Mass (kg)	m
Current specific volume (m^3/kg)	$v = V / m = 1/\rho$
Reference specific volume (m^3/kg)	$v_0 = V_0 / m = 1/\rho_0$
Relative volume (-)	$v_r = V / V_0 = \rho_0 / \rho$
Initial relative volume (-)	$v_{r,t=0} = V_{t=0} / V_0 = \rho_0 / \rho_{t=0}$
Volumetric parameter (-)	$\eta = \rho / \rho_0$
Volumetric parameter (-)	$\mu = (v_0 - v) / v = (\rho / \rho_0) - 1 = \eta - 1$

The reference specific volume, v_0, identifies the nominal condition, in which the stress or strain state of the material is null: at zero compression or expansion, the material is in equilibrium with its ambient surrounding. The reference specific volume represents a unique state with respect to which the material stress tensor is computed, so it is very critical in computing the pressure level in the material. It is also associated with the current specific volume *v*, which has the same expression, but it is actualized with respect to the current volume.

The initial reference volume, $v_{r,t=0}$, defines the state of the material at the time t=0, at which the numerical simulation starts. Defining correctly this variable, it is possible to describe an initial condition, which can be different from the reference one. In this way it is possible to simulate the condition, in which the material is mechanically deformed at the initial state. On the contrary with respect to the reference specific volume, the initial reference volume is, therefore, not unique. As for the previous variable, also in this case, it is possible to refer to the same quantity actualized with respect to the current volume, v_r.

The volumetric parameter η assumes value greater than one if the material is compressed ($\rho > \rho_0$), less than one if the material is expanded ($\rho < \rho_0$) and equal to zero if no loads are applied to the material. Similarly, the volumetric parameter μ is positive if the material is being compressed and negative if the material is being expanded. In Table 3.2 the values assumed by the volumetric parameter is summarized in function of the loading condition.

Table 3.2: Range of the values assumed by the volumetric parameters in function of the loading condition.

Quantity	**Compression**	**No load**	**Expansion**
Relative volume v_r	< 1	1	> 1
Volumetric parameter η	> 1	1	< 1
Volumetric parameter μ	> 0	0	< 0

In LS-DYNA, as in other FE codes, such as Autodyn [3], the EOS implemented are defined, in general, as described by the Eq. 3.3. The independent variables are density and internal energy, while the dependent variable is the pressure. On the other hand, the temperature is only a variable which is derived from the internal energy and is not directly computed. The density can be replaced by the specific volume, the relative volume or one of the volumetric parameters. The other point to clarify concerns the type of internal energy to use. In Table 3.3 different definitions of the internal energy are reported.

Table 3.3: Definition of the internal energy.

Quantity (Units)	**Expression**
Absolute internal energy (J)	$E = MC_v T$
Specific internal energy (J/kg)	$e = C_v T$
Specific internal energy per unit of current volume (J/m^3)	$e_v = \rho C_v T$
Specific internal energy per unit of reference volume (J/m^3)	$e_{v_0} = \rho_0 C_v T = e_v v_r$

In general, the absolute internal energy E is not used and one of the other definitions is preferred. According to this, the EOS should be expressed as follows:

$$P = P(v,e) = P(v_r, e_v) = P(\mu, e_{v_0}) \tag{3.4}$$

The type of energy to use depends on the implementation in the EOS routine of the FE code: in LS-DYNA the internal energy per unit of reference volume (e_{v0}) is used, while in Autodyn the specific internal energy (e) is adopted. In conclusion, for what concerns the use of EOS in LS-DYNA, it is necessary to refer to the last formulation of Eq. 3.4.

In more details, the pressure is computed as the sum of two components:

$$P = P_C(\mu) + P_T(\mu, e_{v_0}) = A(\mu) + B(\mu) e_{v_0} \tag{3.5}$$

where, the first term, $P_C(\mu)$, is called *cold curve* and is function of the density. It is hypothetically evaluated along the 0 K isotherm. The second term, $P_T(\mu,e_{v0})$ expresses the dependency of the pressure by both density and internal energy. In particular, in the EOS implemented in LS-DYNA, the cold curve is a generic function of the density and the thermal component is again a generic function in density but it is linear in energy (see Eq. 3.6).

In a FE code with assigned displacement, once the complete strain tensor is known, it is possible to obtain the density, in accordance with the equation [5]:

$$\varepsilon_v = \ln \frac{\rho_0}{\rho} \tag{3.6}$$

The energy is obtained at each time step by the balance equation, which, in LS-DYNA, is directly managed by the EOS routine:

$$\begin{aligned} e_{v_{0,\mathrm{NEW}}} &= e_{v_{0,\mathrm{OLD}}} + \Delta e_{v_0} \\ \Delta e_{v_0} &= \Delta e_{v_{0,\mathrm{dev}}} + \Delta e_{v_{0,\mathrm{hydro}}} + \Delta e_{v_{0,\mathrm{ext}}} \end{aligned} \tag{3.7}$$

This means that, at the current time step, the current specific energy is the sum between the previous value and the increment of energy get in the time interval between two successive time steps. This increment is the sum of the mechanical work made or suffered by the system and the quantity of energy introduced or subtracted by the external of the system. The mechanical work includes both the irreversible and reversible work. The first one is the deviatoric work, which comes from the plastic deformation of the material. The second component is the hydrostatic work, which is correlated to the variation of volume due to a pressure load.

As mentioned before, the consequent variation in term of temperature is evaluated starting from the Eq. 3.2, by the following relation:

$$\Delta T_{\mathrm{NEW}} = \frac{\Delta e_{v_{0,\mathrm{NEW}}}}{\rho_0 c_P} \tag{3.8}$$

in which c_P is the specific heat at constant pressure, which depends on the state of the matter. In LS-DYNA, in the most cases, c_P is a constant: this implies that, for example, if the c_P of the solid is defined, the temperature evaluation is correct only for the solid phase. On the other hand, if the material undergoes phase changes, the temperature evaluation is not correct above the melting temperature.

3.3 Examples

As example, some EOS, usually implemented in the commercial FEM and hydro-codes (e.g. [3, 4]), are reported and divided between analytical and tabular ones. Analytical EOS are, for example: ideal gas law, linear EOS, Mie-Grüneisen [2], GRAY [6], Puff and Tillotson [7]. On the other hand, the SESAME [8] is an example of an EOS defined in tabular form. Depending on the zone in which the entire EOS surface (P-ρ-E) is defined, the different EOS are distinguished from each others on the basis of the field of

application. The ideal gas law is applicable only for the gas zone. If the interest is focused on a limited range in pressure, the EOS which expresses the pressure as linear function of the density (Bulk modulus) can be sufficient. The Mie-Grüneisen allows extending the range of application to higher pressure and also to the liquid phase, but with limitations for expanded liquid or vapour zone. The GRAY is a three-phase EOS, useful for the description of solid, liquid, vapour states and the transition zones. The Tillotson and Puff EOS are suitable if the material has been subjected to a large energy input reaching a shocked state, which is sufficient to completed separate the atoms and to produce an expansion to large volumes, in which the material behaves like a perfect gas. Finally, when wide ranges both in temperature and density have to be considered for the complete description of a lot of states of the matter, with also the correspondent transition zones, the SESAME tables should be used.

In general, EOS are developed using a combination of statistical mechanical and quantum mechanics theories and experimental data. In particular, shock-wave experiments are used in order to investigate a range, which cannot be investigated using other methods.

For simplicity, in the description of some of the most common EOS, the variable, which identifies the internal energy, will be called *E*, without any distinction on the basis of the type.

3.3.1 Ideal gas law

An ideal gas is defined as one in which all collisions between atoms or molecules are perfectly elastic and in which there are no intermolecular attractive forces. One can visualize it as a collection of perfectly hard spheres, which collide but which otherwise do not interact with each other. In such a gas, all the internal energy is in the form of kinetic energy and any change in internal energy is accompanied by a change in temperature. Other assumptions, which are at the basis of the ideal gas law are: the gas is made up of molecules, which are in constant random motion in straight lines, the pressure is due to collisions between the molecules and the walls of the container and the volume occupied by the molecules themselves is entirely negligible relative to the volume of the container. Obviously, there is no such thing as an ideal gas, but many gases behave approximately as it, especially, at ordinary working temperatures and pressures.

The complete state of an ideal gas can be characterized by three state variables:

absolute pressure (*P*), volume (*V*), and absolute temperature (*T*). The relationship between them may be deduced from kinetic theory and is called the ideal gas law:

$$PV = nRT \tag{3.9}$$

in which *n* is the number of moles and *R* is the universal gas constant (8.3145 J/mol/K). An alternative formulation to the previous one is:

$$Pv = R'T = (c_P - c_v)T \tag{3.10}$$

in which the specific volume is used instead of the volume. This implies that the constant *R'* is used, which depends on the gas and is equivalent to the difference between the specific heats at constant pressure and volume. The last equation expresses the ideal gas law in the same form in which it is implemented in LS-DYNA.

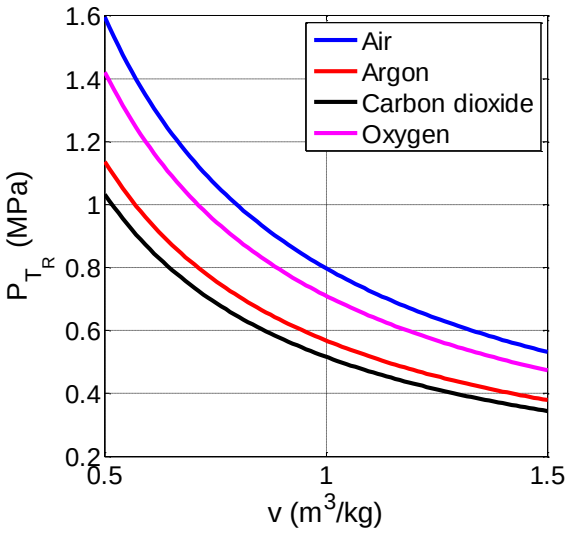

Fig. 3.2: Pressure vs. specific volume curves for T=293.15 K for the gases listed in Table 3.4.

In Table 3.4 the c_P and c_v for some gases are reported and in Fig. 3. 2 the pressure vs. specific volume curves, obtained at constant temperature (T = 20 °C) are reported for the same gases.

Table 3.4: Specific heats and normal density (20°C and 1 atm) for various gases [9]

Gas	c_P **(J/kg/K)**	c_v **(J/kg/K)**	ρ **(kg/m^3)**
Air	1010	718	1.205
Argon	520	312	1.661
Carbon dioxide	844	655	1.842
Oxygen	919	659	1.331

3.3.2 Linear

As mentioned in the chapter 2, a linear EOS can be defined both in density and specific volume. In this paragraph, the EOS linear in density is considered:

$$P(\rho) = K\left(\frac{\rho}{\rho_0} - 1\right) \tag{3.11}$$

where the constant of proportionality is the Bulk Modulus (K). The Eq. 3.11 can be applied for the description of both compression and expansion of materials, but in both the cases, it can be applied only if a small density variation is involved. In more details, the Eq. 3.11 represents the barotropic linear EOS, in which the energy (or temperature) contribution is neglected. A more general form is:

$$P(\rho, E) = K\left(\frac{\rho}{\rho_0} - 1\right) + \gamma_0 E \tag{3.12}$$

in which γ_0 is the Grüneisen parameter (see the next paragraph).

In Table 3.5, the bulk modulus for some materials are reported and in Fig. 3.3 the cold pressure (at E=0) vs. volumetric parameter μ curves are plotted.

Table 3.5: Bulk modulus of various materials [10]

Material	***K* (GPa)**
Aluminium	76
Copper	140
Iron	170
Tantalum	200
Tungsten	310

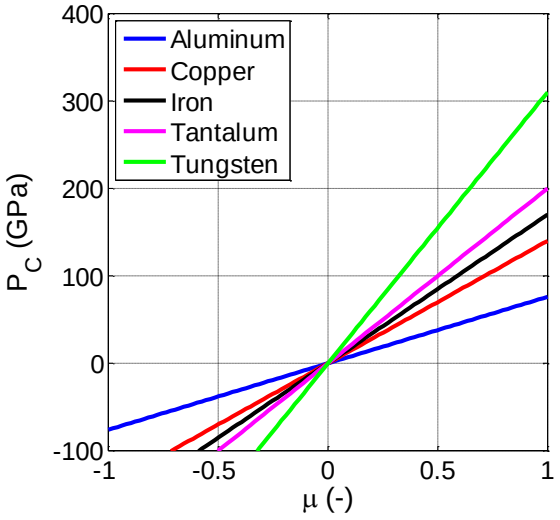

Fig. 3.3: Cold pressure vs. volumetric parameter μ curves both in compression and expansion region for the materials listed in Table 3.5.

A more general formulation implies the definition of a polynomial function, in which the coefficient has to be determined, for example, by interpolation of experimental data or a part of more complex EOS. This type of EOS is implemented in many FEM codes and, often, is expressed in function of the dimensionless volumetric parameter μ:

$$P(\mu, E) = C_0 + C_1\mu + C_2\mu^2 + C_3\mu^3 + (C_4 + C_5\mu + C_6\mu^2)E \tag{3.13}$$

The above equation can be used, imposing specific values to the coefficient, to obtain different formulations. First of all, it is possible to obtain a generic barotropic EOS

imposing $C_4 = C_5 = C_6 = 0$. A linear EOS, such as that of Eq. 3.12, can be obtained imposing $C_0 = C_2 = C_3 = C_5 = C_6 = 0$, $C_1 = K$ and $C_4 = \gamma_0$. The Eq. 3.13 can also be used to model the ideal gas law, in which the thermal variable is the energy instead the temperature, imposing $C_0 = C_1 = C_2 = C_3 = C_6 = 0$ and $C_4 = C_5 = c_P/c_v - 1$. In LS-DYNA, if $\mu < 0$ (expansion), the Eq. 3.13 is automatically simplified with $C_2 = C_6 = 0$.

3.3.3 Mie-Grüneisen

The Mie-Grüneisen equation of state is often used to determine the pressure state of shocked solids. The general expression is:

$$P - P_H = \frac{\gamma}{v}\left(E - E_H\right) \tag{3.14}$$

where H identifies the reference state (e.g. the isothermal state at 0 K or one point on the Hugoniot) and γ is the Grüneisen parameter. The latter can be defined both starting from macroscopic thermo-mechanical considerations and from statistical mechanics. From a macroscopic point of view, supposing to have a system with internal energy E, pressure P, specific volume v and temperature T, the Grüneisen parameter is defined as [11]:

$$\gamma = v\left(\frac{dP}{dE}\right)\Bigg|_v = v\frac{\alpha K}{c_v} \tag{3.15}$$

in which α is equal to the thermal expansion coefficient, c_v the specific heat at constant volume and K the Bulk Modulus at constant temperature. From this, it is possible to conclude that γ is a measure of the change in pressure produced by a change in energy under the condition of constant volume.

As approximation, it can be considered that the ratio γ/v is constant [12]:

$$\frac{\gamma}{v} = \frac{\gamma_0}{v_0} \tag{3.16}$$

where γ_0 and v_0 are calculated at zero pressure. Another possible definition, which considered a first order volume correction of the previous equality, gives [13]:

$$\gamma = \gamma_0 \frac{v}{v_0} + a\left(1 - \frac{v}{v_0}\right) \tag{3.17}$$

One of the possible forms, which is the formulation used in the most part of FE codes, in which the Mie-Grüneisen EOS can be written is:

$$P(\mu, E) = \frac{\rho_0 C_0^2 \mu \left[1 + \left(1 - \frac{\gamma_0}{2}\right)\mu - \frac{a}{2}\mu^2\right]}{\left[1 - (S_1 - 1)\mu - S_2 \frac{\mu^2}{1+\mu} - S_3 \frac{\mu^3}{(1+\mu)^2}\right]^2} + (\gamma_0 + a\mu)E \tag{3.18}$$

where ρ_0 is the solid density, C_0 the elastic sound speed (intercept of the U_S vs. u_P relation), γ_0 the Grüneisen parameter, a is the first order volume correction to γ_0 and the coefficients S_i define the cubic U_S vs. u_P relationship. The Eq. 3.18 is valid only for compressed material. The definition for expanded material is:

$$P(\mu, E) = \rho_0 C_0^2 \mu + (\gamma_0 + a\mu)E \tag{3.19}$$

In Table 3.6 the parameters needed to plot the Mie-Grüneisen EOS are reported for various materials [13]. In Fig. 3.4 the cold pressure (at E=0) vs. specific volume curves are reported for the material listed in Table 3.6, for the compression region.

Table 3.6: Parameters for the Mie-Grüneisen EOS [13].

Material	ρ_0 **(kg/m^3)**	C_0 **(m/s)**	γ_0 **(-)**	a **(-)**	S_1 **(-)**
Aluminium 6061-T6	2703	5240	1.97	0.48	1.400
OFHC copper	8930	3940	2.02	0.47	1.489
Stainless steel 304	7900	4570	1.93	0.50	1.490
Tantalum	16690	3410	1.67	0.42	1.200
Titanium alloy (Ti6Al4V)	4419	5130	1.23	0.17	1.028
Tungsten	19300	4030	1.67	0.38	1.237

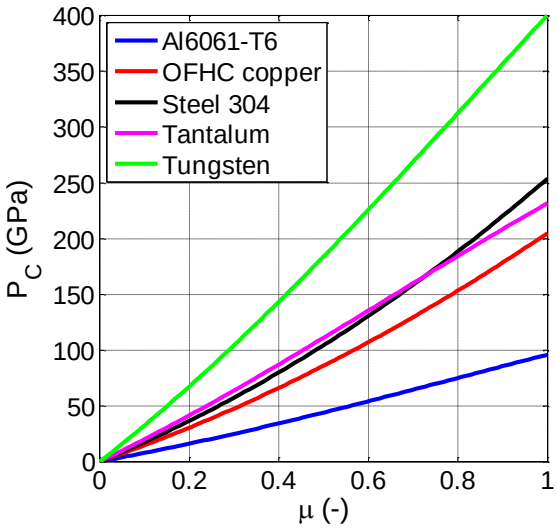

Fig. 3.4: Cold pressure vs. volumetric parameter μ curves in the compression region ($\mu > 0$) for the materials listed in Table 3.6.

Comparing Figs. 3.3 and 3.4 (which are plotted in the compression region in the same range of μ), it is possible to notice that, as expected, for limited values of compression, the two formulations (Eqs. 3.11 and 3.18) give the same results. Otherwise, for large compression, the linear EOS underestimates the pressure. In the expansion region, the two formulations are equivalent.

3.3.4 GRAY (Grovers-Royce-Alder-Young)

The GRAY EOS is a three-phase equation of state developed for metals by Royce [6]. The EOS is layout in the plane *P-v-E*, where *P* is the dependent variable and *v* and *E* are the independent variables. The EOS parameters are given by the author for several materials, among which aluminium, titanium, stainless steel, nickel, copper, tantalum, tungsten and lead.

This EOS was obtained for the description of high-temperature and high-pressure conditions, which can be reached e.g. in case of sudden high energy deposition in the material. The idea used by the developers was thinking about the entire equation of state as divided in three distinct regions.

- ✓ Material compressed adiabatically or by shock processes. This can be considered, relatively, a cool process (few elettronvolts): most of the energy is

stored elastically during the compression. For this region, the standard Mie-Grüneisen EOS can be used and shock-waves techniques were applied for the experimental investigation.

- ✓ Material subjected to high pressure in high temperature but normal density conditions. This can be the case in which the energy deposition is so rapid, that the deposition time is shorter than the characteristic hydrodynamic time of the heated system. The material has no time to react: the density does not change and pressure and temperature grow up in accordance with the amount of energy introduced in the system.
- ✓ Material subjected to expansion in high temperature but low pressure conditions. In this case, the deposition time allows the material to expand, lowering the pressure. The same condition is typical of the rarefaction phase, which always follows a sudden energy deposition, when it finished.

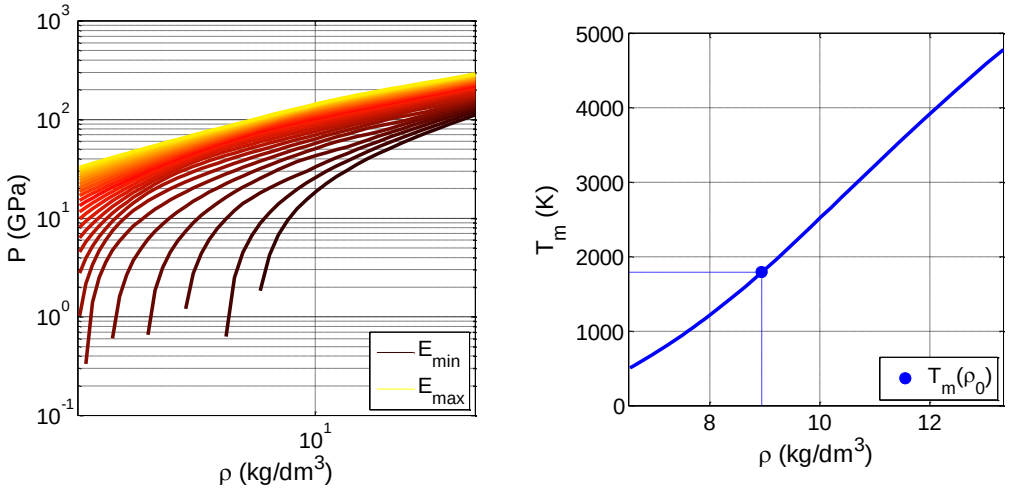

Fig. 3.5: Pressure vs. density varying the internal energy for copper (left); melting temperature in function of density (right). The dot point has coordinates (ρ_0,T_{m0}).

The GRAY EOS covers the solid-liquid and liquid-vapour regions: solid, liquid, hot liquid, transition between solid and liquid and that between liquid and vapour phases are described. The distinction between solid-liquid and liquid-vapour regions is made on the basis of the specific volume. The different states of matter in the solid-liquid region are identified in function of the energy. The melting temperature is considered to be a function of the density and has a different formulation for compressed or expanded materials.

For the complete formulation, see [6]. This EOS is not implemented neither in LS-DYNA nor AUTODYN, but e.g. it is implemented in RADIOSS. In Figs. 3.5 and 3.6, the pressure vs. specific volume curves varying the specific energy and the melting temperature in function of the density are plotted for copper and tungsten.

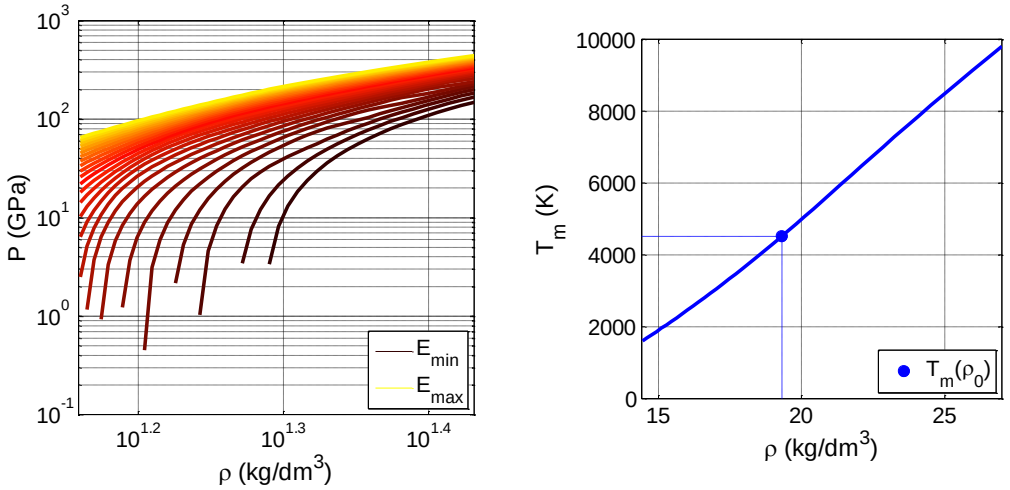

Fig. 3.6: Pressure vs. density varying the internal energy for tungsten (left); melting temperature in function of density (right). The dot point has coordinates (ρ_0,T_{m0}).

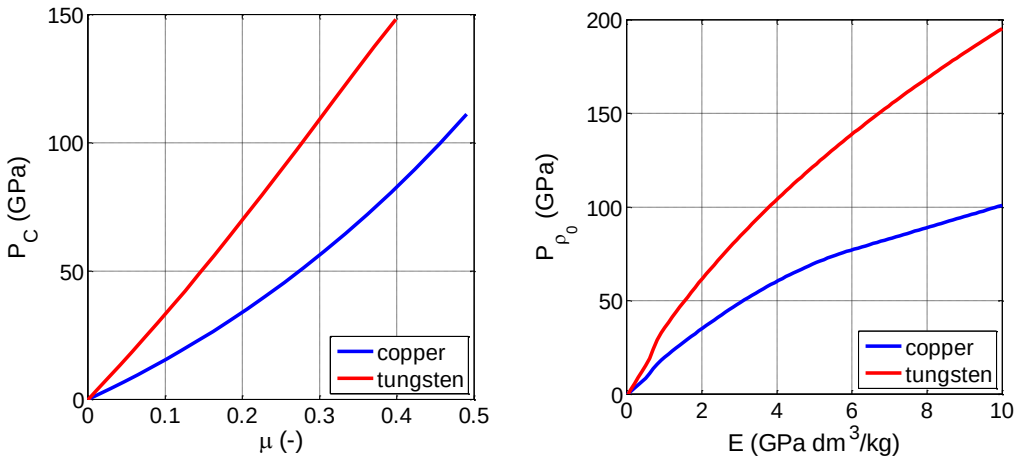

Fig. 3.7: Cold pressure vs. volumetric parameter μ (compression region) and pressure at the solid nominal density vs. internal energy curves: comparison between copper and tungsten.

In Fig. 3.7, the cold pressure (at $E = 0$) vs. density and the pressure vs. internal energy at the solid density are compared for the two materials. As it is possible to notice, comparing the Figs. 3.4 and 3.7 for copper and tungsten, the GRAY EOS and the Mie-

Grüneisen one give very similar results in the compression region. This is due to the fact that, as mentioned before, the formulation of the GRAY EOS is obtained starting from the other one.

3.3.5 Tillotson

The Tillotson EOS [3] was developed for describing the state of materials subjected to hypervelocity impacts. In more details, it is able to reproduce the normal density conditions, the shocked states (compression) and also the expansion phase, in which the material could melt or vaporize, depending on the amount of energy stored during the shock. Also in this case the dependent variable is the pressure, which is considered to be function of energy and density, in the form of the dimensionless parameter μ.

Looking the *P-v* plane, as reported in Fig. 3.8, the complete EOS is divided into four regions. The region to the left of the Hugoniot can only be reached by adiabatic (non-shocked) compression and is not relevant for impact problems. It is, therefore, excluded from the formulation. Besides, this equation of state does not describe the material behaviour at pressures less than zero. The different formulations have to respect the constraint of ensuring continuity in pressure and its first derivative at the boundary. For the complete formulation, see [3]. This EOS is implemented in AUTODYN, but not in LS-DYNA.

The region indicated as I represents the compressed shocked states ($\mu > 0$) of the material and extends vertically until pressures of about 150 GPa.

The region indicated as II describes a material, which is shocked to an energy less than the sublimation energy E_s ($\mu < 0$, $E < E_s$) and will therefore, return to zero pressure as a solid, during the adiabatic release.

The region indicated as IV describes the expansion phase ($\mu < 0$), corresponding to a condition in which the material is shocked to an energy E_s' ($E > E_s'$) sufficiently large to ensure that it will expand as a gas at very large expansions. For very high specific volumes it tends to the ideal gas law.

In the region indicated as III ($\mu < 0$, $E_s < E < E_s'$), the pressure is evaluated as the average between that of regions II and IV.

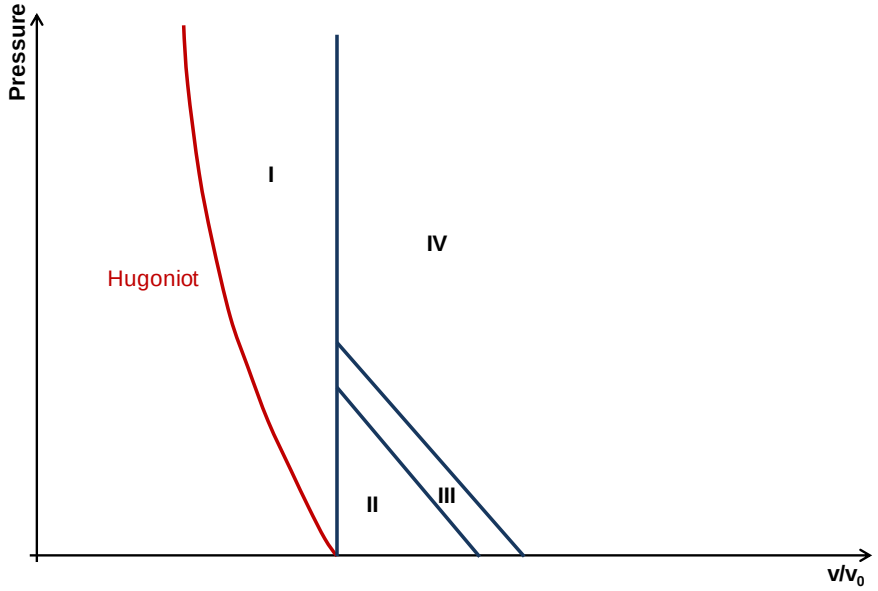

Fig. 3.8: Pressure vs. relative specific volume plane defined by the Tillotson EOS.

3.3.6 Puff

As the Tillotson EOS, also the Puff EOS was developed for the description of states of matter involved by cold to hot shock and high expansion. Differently from the previous one, only three regions are defined. In reference to Fig. 3.8, the region described by the Puff EOS are those indicated as I, II and IV (the region III is neglected). This means that the only sublimation energy E_s is considered. It is however important to underline that the equations, which define the pressure in each region, are not the same of those proposed for the Tillotson EOS. For the complete formulation, see [3].

3.3.7 SESAME

The SESAME is a library of EOS, in which the thermodynamic properties of a large number of materials (about 150) are reported in form of table. The EOS are obtained for different types of materials, such as simple elements, compounds, metals, minerals, polymers, mixtures, etc.

The thermodynamic data stored in the library include tables of pressure P and internal energy E (in many cases, also the Helmholtz free energy A is supplied). These dependent variables are expressed in function of density ρ and temperature T. The typical density and

temperature ranges are from 10^{-6} to 10^{4} g/cm^3 and 0 to 10^{5} ev, respectively, but it depends on the considered material. The EOS contained in the SESAME library are multi-phase and allow the description of all the state of the matter: solid, liquid, gas, plasma and their transitions.

Since the dependent variables are defined over so wide ranges of density and temperature, and due to the fact that diverse kinds of phases and materials are included, the global EOS of a material should be formed using various combinations of different theoretical models, depending on the region.

In Figs. 3.9 and 3.10 the EOS in the *P*-ρ and *P*-*E* planes varying the temperature are reported for copper and tungsten.

The EOS for copper is reported and described in [14]. In the SESAME library different EOS for copper can be found. For the study presented in the next chapters, the table used is the 3320. It is defined between 0 and 500 g/cm^3 in density and between 5 and 10^{8} K in temperature.

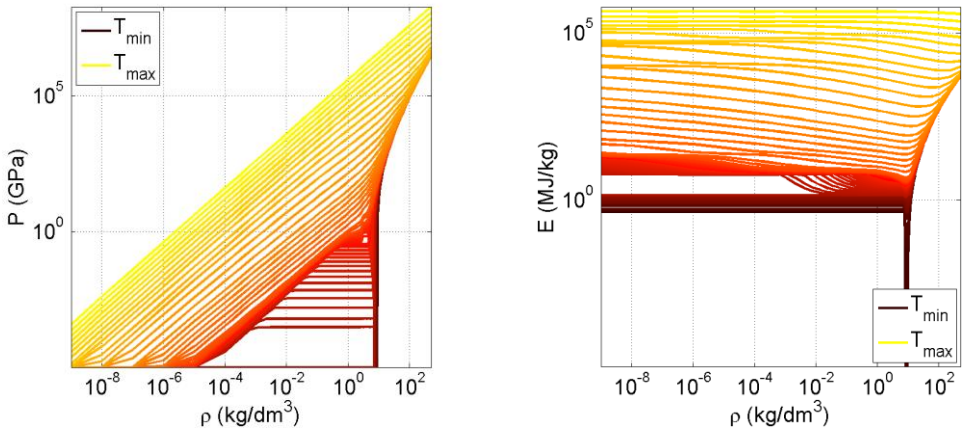

Fig. 3.9: Pressure vs. density and specific energy vs. density planes varying the temperature for copper [14].

The EOS for tungsten is reported and described in [15]. For the study presented in the next chapters, the table used is the 3550. It is defined between 0 and 500 g/cm^3 in density and between 5 and 10^{8} K in temperature.

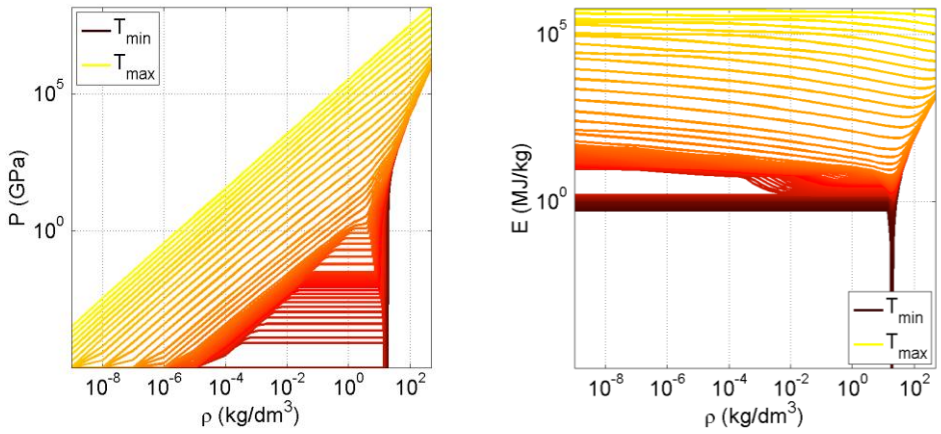

Fig. 3.10: Pressure vs. density and specific energy vs. density planes varying the temperature for tungsten [15].

References

[1] Adkins C.J., "Equilibrium thermodynamics", Cambridge University Press (Cambridge Cambridgeshire and New York), (1983) ISBN 0521254450.

[2] Eliezer S., Ghatak A. K. and Hora H., "Fundamentals of Equations of State", World Scientific Pub Co Inc. (2002), ISBN 9810248334.

[3] "ANSYS AUTODYN User's Manual – Release 2010", ANSYS Inc. (2010)

[4] Gladman B et al., "LS-DYNA® Keyword User's Manual – Volume I – Version 971", LSTC (2007)

[5] Hosford W.F., "Mechanical Behavior of Materials" Cambridge University Press (209), ISBN 0521195691.

[6] Royce E.B., "GRAY, A THREE-PHASE EQUATION OF STATE FOR METALS", Technical Report UCRL-51121, California Univ., Livermore. Lawrence Livermore Lab. (1971).

[7] Tillotson J. H., "Metallic equations of state for hypervelocity impact", General Atomic Report, Rep GA. 3216, 139 pp. Gen. Dyn. Corp., San Diego, California (1962).

[8] Holian K.S., "T-4 Handbook of Material Properties Data Bases, Vol. Equations of State" LA-10160-MS Los Alamos National Laboratory (1984).

[9] http://www.engineeringtoolbox.com/spesific-heat-capacity-gases-d_159.html

[10] http://www.webelements.com/periodicity/bulk_modulus/

[11] Harris P., et al., "Some physics of the Grüneisen parameter", Technical report n. 4423 (1972).

[12] Meyers M. A., "Dynamic behaviour of materials", J. Wiley & Sons (1994), ISBN 047158262.

[13] Steinberg D.J., "Equation of State and Strength Properties of Selected Materials", Lawrence Livermore National Laboratory, UCRL-MA-106439, (1996)

[14] Kerley, G.I., "Equations of State for Copper and Lead", KTS02-1 (2002).

[15] Kerley, G.I., "Equations of State for Be, Ni, W, and AU", SANDIA REPORT SAND 2003-3784 (2003).

4. Strength material models

In this chapter, the concepts at the basis of the definition of strength material models are described, with particular reference to the high strain-rate and shock-wave regime. In this perspective, in the first part, an overview of all the variables of interest in such kind of problems is examined. Then, the most common strength models, usually implemented in commercial FE codes, are examined. In particular, the attention is focused on the meaning of the model parameters and the availability of data for different materials, for which the plastic behaviour is analyzed and compared. After this, also some failure models, which should to be defined in a numerical model for the complete description of the material behaviour, are presented. In the final part of this chapter, a procedure for the material model identification, based on a numerical inverse method, is presented.

As discussed in the previous chapter, in the usual continuum mechanics treatment, the complete stress tensor, which describes the material condition state, is divided into two components: the deviatoric and the hydrostatic tensor. In this chapter the attention is focused mainly on the deviatoric component, which concerns the phenomena associated with the material strength, in particular in both plasticity and failure regime. In order to understand high strain-rate response of metallic materials, a constitutive model, which is applicable in wide range of strain, strain-rate and temperature, is needed. Together with this requirement, also the simplicity in obtaining the model parameters from experimental data is a fundamental aspect.

In general, a phenomena in which high strain-rate or shock conditions are reached, the choice of the material constitutive equations (strength model and equation of state) is of fundamental importance: all the mechanical and thermodynamic variables that play a key role in the material deformation process have to be taken into account. For the visco-

thermo-plastic behaviour description, the definition of constitutive relations is needed, in which the flow stress is defined in function of all the variables of interest. Usually, in plasticity, the independent variables are: deformation (both plastic and volumetric), strain-rate, temperature and pressure.

As a matter of fact, this type of phenomenon is strongly thermo-structural coupled: the structural-mechanics material conditions produce the rise in temperature that consequently modifies the mechanical material response. In particular, due to the rise in temperature, there is a modification in the effect of the strain-rate on the flow stress. In addition high pressure condition can be reached, influencing the material response both in strength and hydrodynamic regime. Finally, the strain-rate becomes important since the phenomena occur in a quite short time and usually is also associated with high level of deformation and, eventually, damage.

In past decades a lot of material models, for the description of the deviatoric behaviour, are proposed. The classification makes a distinction between empirical, semi-empirical and physically-based models. The empirical models have not any physical basis, but are obtained by interpolation of the experimental data. On the other hand the physically-based models are obtained starting from the transformation in the material occurring during a deformation process. A model such that proposed by Johnson-Cook (J-C) [1] is purely empirical model and it is one of the most widely used. An example of semi-empirical model is the Zerilli-Armstrong (Z-A) model [2], that is obtained on the basis of the dislocation mechanics theory and presents a different formulation for Body Centered Cubic (BCC) and Face Centered Cubic (FCC) materials. Another example of semi-empirical model is the Steinberg-Cochran-Guinan-Lund (S-C-G-L) model [3, 4], which was first developed for the description of high strain-rates behaviour [3], and after extended to low strain-rates [4]. A completely physical-based more complex model is the Mechanical Threshold Stress (MTS) model [5, 6], for which the stress is described on the basis of the dislocation theory. Most of these material models are usually implemented in commercial FE codes, such as LS-DYNA [7] and AUTODYN [8].

When the material overcomes its elastic limit, it enters in plasticity: from a macroscopic point of view, this corresponds to an appreciable distortion of the material, from a microscopic point of view this implies the generation of slip band and, finally, from an atomic point of view it corresponds to dislocation movement. Loading the material in these conditions causes the generation, movement and accumulation of

dislocation, which implies permanent deformation inside the material, is occurring. Two types of obstacles can prevent the dislocation motion inside the lattice: long and short range barriers, see [9].

The short range barriers are strictly correlated to the material structure and can be surmounted by increasing, thermally, the energy of system. As a matter of fact the increment of the energy increases the amplitude of the vibration of the atoms around their lattice position. This increases the probability that an atom reaches a new equilibrium condition in another site, facilitating in this way the dislocation motion. The thermal energy educes the energy offered by short-range barriers, decreasing the force required to move the dislocation. The strain-rate has an opposite effect with respect to the temperature: the dislocation has less time to overcome the obstacle, reducing the effect of the thermal energy and, consequently, increasing the force required.

On the other hand, the long range barriers are correlated to point defects, such as solute or vacancies, precipitates, boundary or the presence of other dislocations. This type of obstacle cannot be overcome by additional thermal energy: the energy required to move the atoms past long-range dislocation is orders of magnitude higher.

Accordingly to this, the total flow stress, which represents the material strength to deformation, can be considered as the sum of two components:

$$\sigma_y = \sigma_{\text{th}} + \sigma_{\text{ath}} \tag{4.1}$$

in which σ_{th} is the thermal component correlated to the short range interaction and σ_{ath} is the athermal component correlated to the long range interaction. Since, depending on the crystal lattice structure, the dislocation motion in high strain-rate condition is different, it is reasonable to expect different responses for Body Centered Cubic (BCC), Face Centered Cubic (FCC), Hexagonal Close Packing (HCP) and others.

In general, a visco-thermo-plastic model expresses the flow stress as a combination of athermal and thermal components. The athermal part of the stress can be in general correlated with strain, strain-rate, temperature and pressure, while the thermal component identifies the temperature influence on the strain-rate effects on the flow stress.

Before entering in more details into the description of some material mode, it is necessary to make some considerations about the problems, which can be found using strength material model, especially in FE codes. First of all, there is a great problem related to the availability of comparable data for different materials in different models.

As a matter of fact, the most part of these models were obtained during the decade between 1980 and 1990 and they were often calibrated and tested only for one or few materials. The materials used are generally pure metals (such as copper, iron and tantalum) or their alloys (such as brass). However, in general, the available data are for materials generally used in military or nuclear applications. Otherwise, it is very difficult to find data for other materials or alloys. Another problem is related to the comparison between the parameters obtained for different models. This is mainly due to the fact that the model parameters depend upon the microstructural material properties or on the chemical composition, in case of alloy. For example, the mechanical behaviour of copper depends on the grain dimension: this means that the parameters of two different models are strictly comparable only if the material is exactly the same. Another point of importance regards the range of applicability of the model parameters that can be found in literature, especially in case of empirical models, in which the parameters are obtained fitting the experimental data. As a matter of fact, the value of the obtained parameters strongly depends on the range in which the independent variables (such as strain, temperature and strain-rate) varied as well as the type of tests performed. The last problem is strictly correlated to the implementation of the constitutive material model in a FEM code. In a code like LS-DYNA [7], a lot of material models are implemented, but not always the formulation is completely the same of the original one, and this makes the correlation with materials parameters quite difficult. Besides, in some cases, the parameters present different interpretation or range of applicability.

4.1 Johnson-Cook

Several authors used the J-C model, or its modified formulations, in order to investigate and describe problems such as ballistic impacts or, more in general, problems in which the strain-rate component was relevant.

The J-C model [1] is the simplest model able to predict the mechanical behaviour of the materials under different loading conditions. Besides, as mentioned before, it is one of the most used material models, so it is implemented in many FEM codes and it is quite easy to find in literature the values of J-C parameters for different materials. In the J-C model only the athermal stress component is taken into account and the flow stress is defined as follows:

$$\sigma_y = \left(A + B\varepsilon_{\mathrm{pl}}^{n}\right)\left(1 + C\ln\frac{\dot{\varepsilon}_{\mathrm{pl}}}{\dot{\varepsilon}_0}\right)\left(1 - \left(\frac{T - T_r}{T_m - T_r}\right)^{m}\right) \tag{4.2}$$

In more details, *A* is the elastic limit strength, *B* and *n* are the work hardening parameters and influence the slope of the flow stress in the plastic domain. The parameter *n* usually assumes values between 0 (for perfectly plastic model) and 1 (for a piecewise linear model). *C* expresses the strain-rate sensitivity coefficients and $\dot{\varepsilon}_0$ is, in the original formulation, set equal to 1. The thermal effects are described in function of the thermal softening coefficient *m*, the actual temperature *T*, the reference temperature, at which there are not any thermal effects T_r and the melting temperature, at which the material mechanical strength goes to zero T_m. In this condition, the material loses its shear strength and starts to behave like a fluid. The thermal parameter *m* determines the concavity of the temperature function: if $m < 1$ the function is convex, if $m > 1$ it is concave and if $m = 1$ the temperature influence is linear.

The formulation implemented in LS-DYNA is exactly the same of that reported in Eq. 4.2. The difference with respect to the original formulation regards the parameter $\dot{\varepsilon}_0$. In more details, in LS-DYNA [7], $\dot{\varepsilon}_0$ represents the quasi-static strain-rate threshold, which, ideally, represents the highest strain-rate for which the strain-rate effects on the flow stress are negligible. For strain-rate less than this value, there are not any strain-rate influences (the second terms of the Eq. 4.2 is identically equal to 1).

The J-C model is a multiplicative model, in which the effects of plastic strain, strain-rate and temperature are uncoupled. It is clear from the Eq. 4.2 that, a strain-rate or temperature variation implies only a scaling and not a modification in the shape of the strain hardening curve. This means, also, that temperature and strain-rate influences are considered to be constant for any plastic strain value. Moreover, the J-C model does not take into account any influence of the thermal and strain-rate history. Obviously, these are simplifying assumptions. The J-C model is also quite inaccurate to model the material behaviour in case of high pressure conditions. As a matter of fact, it neglects the influence of pressure and changes in volume on the flow stress. Besides, it considers the melting temperature as a constant, while the solid-liquid transition is influenced by the density. Finally it is too simplistic, since it does not consider the different material response in function of the crystal lattice.

Table 4.1: J-C model parameters for various materials [1]

Material	**Melting Temperature (K)**	***A*** **(MPa)**	***B*** **(MPa)**	***n*** **(-)**	***C*** **(-)**	***m*** **(-)**
OFHC copper	1356	90	292	0.31	0.025	1.09
Cartridge brass	1189	112	505	0.42	0.009	1.68
Nickel 200	1726	163	648	0.33	0.006	1.44
Armco Iron	1811	175	380	0.32	0.060	0.55
Electrical iron	1811	290	339	0.40	0.055	0.55
1006 steel	1811	350	275	0.36	0.022	1.00
2024-T351 aluminium	775	265	426	0.34	0.015	1.00
7039 aluminium	877	337	343	0.41	0.010	1.00
4340 steel	1793	792	510	0.26	0.014	1.03
S-7 tool steel	1763	1539	477	0.18	0.012	1.00
Tungsten alloy	1723	1506	177	0.12	0.016	1.00

In Table 4.1 the results obtained from experimental data (torsion varying strain-rate and dynamic tension varying temperature tests) by Johnson and Cook in the original work [1] are summarized.

It is important to underline that, in the original formulation, the coefficient $\dot{\varepsilon}_0$ was not considered as a material property, but just as a factor (equal to 1 s^{-1}, as mentioned before) to make the variable $\dot{\varepsilon}_{pl}$ dimensionless. So, in the original formulation the J-C model was

a 5 parameters model. The reference temperature considered in [1] was the room temperature. The material models obtained fitting experimental data were validated on the comparison between computed results with data for Taylor impact tests.

In Fig. 4.1 the J-C model for four materials (OFHC copper, Armco iron, 2024-T351 aluminium and tungsten alloy) is reported. In particular the strain-hardening curves of the materials are compared, as well as both the strain-rate and the temperature coefficients (respectively called $C_{S\text{-}R}$ and C_T).

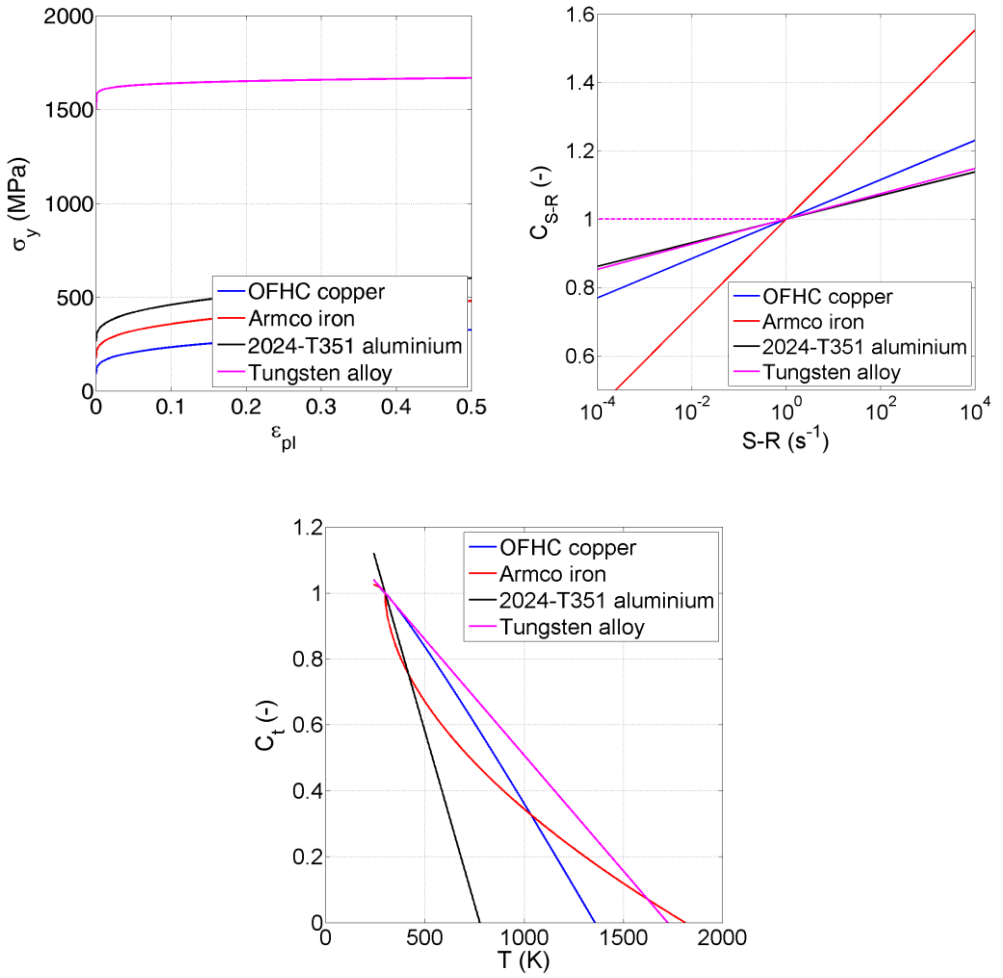

Fig. 4.1: J-C model for OFHC copper, Armco iron, 2024-T351 aluminium and tungsten alloy: (a) strain hardening, (b) strain-rate coefficient and (c) temperature coefficient.

From the diagrams of Fig. 4.1 it is possible to conclude that, the tungsten alloy has the highest yield stress but with the low strain-hardening effect. The iron has the highest strain-rate sensitivity, while tungsten and aluminium alloys have more or less the same

dependency. In Fig. 4.1, in the diagram of the coefficient $C_{S\text{-}R}$, the dashed line represents the trend assumed by the coefficient in the LS-DYNA code, for the same values of the other parameters.

For what concerns the thermal softening, three different behaviours are shown. For the aluminium and tungsten alloys the temperature coefficient decreases linearly, increasing the temperature. For Armco iron the function defining the temperature coefficient is convex, while, for OFHC copper it is slightly concave. For all the materials, the coefficient becomes equal to 0 in correspondence of the respective melting temperature.

4.2 Zerilli-Armstrong

The Z-A [2] model is based on simplified dislocation mechanics, and like the J-C model, neglects pressure and density influences and considers the shear modulus and the melting temperature to be constant. At difference from J-C model, it takes into account also the thermal component of the stress. Since it is partially physical-based, it has a different flow stress formulation for FCC and BCC materials.

The flow stress is expressed as:

$$\sigma_y = \Delta\sigma_G + B\sqrt{\varepsilon_{pl}}\,\mathrm{e}^{(-\beta_0+\beta_1\ln(\dot{\varepsilon}))T} + \frac{k_e}{\sqrt{l}} \qquad \text{(FCC)}$$

$$\sigma_y = \Delta\sigma_G + B\sqrt{\varepsilon_{pl}}\,\mathrm{e}^{(-\beta_0+\beta_1\ln(\dot{\varepsilon}))T} + \frac{k_e}{\sqrt{l}} \qquad \text{(FCC)} \tag{4.3}$$

where l represents the polycrystal grain diameter and $\Delta\sigma_g$, B_0, B_1, β_0, β_1, K_0, n and k_e are experimental constants based on a dislocation mechanics analysis of the plastic deformation mechanism operative in the two different crystal lattice structures. In accordance to the division of the entire flow stress in thermal and athermal components, the Eq. 4.3 becomes:

$$\sigma_y = \sigma_{\text{ath}} + B\sqrt{\varepsilon_{pl}}\,\mathrm{e}^{(-\beta_0+\beta_1\ln(\dot{\varepsilon}))T} \qquad \text{(FCC)}$$

$$\sigma_y = \sigma_{\text{ath}} + B\mathrm{e}^{(-\beta_0+\beta_1\ln(\dot{\varepsilon}))T} \quad \text{(BCC)} \tag{4.4}$$

In the original work, these constitutive equations are applied to reproduce the deformed shape of cylinders subjected to Taylor impact tests and dynamic tensile results. The data were obtained for Armco iron and copper and the results were reported in Table 4.2.

Table 4.2: Z-A model parameters for various materials [2]

Material	$\Delta\sigma_G$ **(MPa)**	B **(MPa)**	β_0 β_1 **(kK-1)**	K_0 **(MPa)**	k_e **(mm$^{1/2}$MPa)**	n **(-)**
Copper	46.5	890	2.8 0.115	-	5	-
Armco Iron	0	1033	6.98 0.415	266	22	0.289

Looking the set of Eq. 4.4, it is possible to well appreciate the differences between the two formulations of the Z-A model depending on the lattice structure.

For FCC material (such as copper, aluminium, lead, etc.), the thermal component of stress is strongly affected by plastic strain. Otherwise, the athermal component is constant: the yield stress (e_{pl} = 0) does not change for any temperature or strain-rate variations (see Fig. 4.2).

On the contrary, in case of BCC material (such as tantalum, tungsten, etc.), the athermal component is function of the material hardening, which is not influenced by temperature and strain-rate, while the yield strength depends on the them (see Fig. 4.2).

In Fig. 4.2, the model prediction of the mechanical behaviour is reported for copper and Armco iron. The above mentioned consideration can be easily understood looking five different cases both for copper and Armco iron, obtained varying temperature and strain-rate. The cases analyzed are: T=298 K @ 10^{-3}, 1 and 10^{3} s^{-1} and 1 s^{-1} @ 240, 298 and 1000 K. For copper the grain dimension considered is 37 μm, for the Armco iron it is 100 μm. In case of copper all the curves start at the same point, but the shapes are different, since the hardening is influenced by temperature and strain-rate. In case of Armco iron, the yield stress changes, but variation in temperature and strain-rate produces simply a scaling of the stress-plastic strain curves.

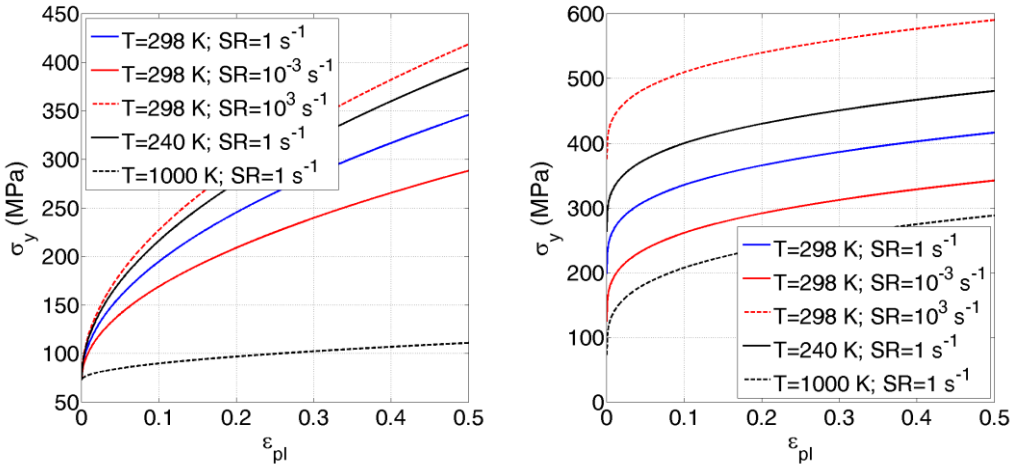

Fig. 4.2: Z-A model for copper (left) and Armco iron (right): effect of strain-rate and temperature variations.

In LS-DYNA, the formulation is a little bit different from that reported in Eq. 4.4:

$$\sigma_y = C_1 + \left[\left(C_2\sqrt{\varepsilon_{pl}}\,\mathrm{e}^{(-C_3+C_4\ln(\dot{\varepsilon}))T}\right)+C_5\right]\frac{\mu(T)}{\mu(293)} \qquad \text{(FCC)}$$

$$\sigma_y = C_1 + C_2\mathrm{e}^{(-C_3+C_4\ln(\dot{\varepsilon}))T} + \left[C_5\left(\varepsilon_{pl}\right)^n + C_6\right]\frac{\mu(T)}{\mu(293)} \qquad \text{(BCC)} \qquad (4.4b)$$

$$\frac{\mu(T)}{\mu(293)} = B_1 + B_2T + B_3T^2$$

The last equation is a polynomial expression to represent the temperature dependency of the flow stress yield, which was not considered in the original formulation. Considering $B_1 = 1$ and $B_2 = B_3 = 0$ and then considering $C_5 = 0$ for FCC materials and $C_6 = 0$ for BCC materials, the flow stresses, both for FCC and BCC material assume the same form of Eq. 4.4.

4.3 Steinberg-Guinan & Steinberg-Lund

A more accurate model is the S-G material model [3] in which both the flow stress and the shear modulus are function of temperature, strain and also pressure. The principal

equations of the model are [10]:

$$\begin{aligned}
&\sigma_y = \sigma_{\text{ath}} \, G/G_0 \\
&G/G_0 = \left[1 + h_1 P v^{1/3} - h_2 \left(\frac{E - E_c}{c_p} - 300 \right) \right] \\
&\sigma_{\text{ath}} = \sigma_0 \left[1 + \beta \left(\varepsilon_{pl,i} + \varepsilon_{pl} \right) \right]^n < \sigma_{\text{MAX}} \\
&T_m = T_{m0} \exp\left[2a(1 - v) \right] v^{-2(\gamma_0 - a - 1/3)}
\end{aligned} \tag{4.5}$$

where v is the relative volume, β and n are the work-hardening parameters and $\varepsilon_{pl,i}$ is the initial equivalent plastic strain, normally equal to zero. The temperature T is defined as the difference between the total energy (E) and the energy along the 0 K isotherm (E_c, see [3] for the definition), divided by the specific heat of solid (c_P): $T = (E\text{-}E_c)/ c_P$. The subscript 0 refers to the condition in which T=300 K, P=0 and ε=0, the reference state. h_1 and h_2 are proportional to the derivative of the yield stress respect to the pressure and the derivative of the shear modulus respect to the temperature, respectively. Also for this model, if the temperature overcomes the melting temperature then the material strength goes to zero, but in this case the melting temperature is not constant but is a density function. A unique formulation, independent from the lattice structure, is defined.

The S-G model is strain-rate independent: this means that only the athermal stress component is taken into account. This aspect is explained in [3]. The authors considered that the increase of the strength with strain-rate should have a limit, that is, there is a certain strain-rate, beyond which strain-rate has no longer significant effects. As a matter of fact the authors found that this limits was about 10^5 s^{-1} in strain rate (or, equivalently, 10 GPa in shock induced experiments). They also explained in [3], that the rapid decrease of rate dependent effects with increasing dynamic stress may be due to the increase in temperature with increasing stress.

In Tables 4.3-4.5, the model parameters for some materials (both BCC and FCC), as reported in [3], are summarized. Table 4.3 contains the parameters for the athermal strain-hardening part. Table 4.4 contains the shear modulus and its partial derivative respect to pressure and temperature. Finally, Table 4.5 contains the parameters for the definition of the melting temperature function.

Table 4.3: S-G model parameters for various materials for the strain hardening function [3, 10]

Material	σ_0 **(GPa)**	σ_{max} **(GPa)**	β **(-)**	n **(-)**
Al 6061-T6	0.29	0.68	125	0.10
Gold	0.02	0.225	49	0.39
OFHC (1/2 hard) copper	0.12	0.64	36	0.45
Lead	0.008	0.1	110	0.52
Molybdenum	1.6	1.52	20	0.15
Stainless steel (304)	0.34	2.5	43	0.35
Tantalum	0.77	1.1	10	0.1
Titanium	0.71	1.45	780	0.065
Tungsten	2.20	4.0	7.7	0.13

Table 4.4: S-G model parameters for various materials for the flow stress and shear modulus dependence by pressure and temperature [3, 10]

Material	G_0 **(GPa)**	h_1 **(TPa^{-1})**	h_2 **(kK^{-1})**
Al 6061-T6	27.6	65	0.62
Gold	28	38	0.31
OFHC (1/2 hard) copper	47.7	28	0.38
Lead	8.6	116	1.16
Molybdenum	125	11.4	0.152
Stainless steel (304)	77	26	0.45
Tantalum	69	14.5	0.13
Titanium	43.4	11.5	0.62
Tungsten	160	9.4	0.14

Table 4.5: S-G model parameters for various materials for the melting temperature function [3, 10]

Material	T_{m0} **(K)**	γ_0 **(-)**	a **(-)**
Al 6061-T6	1220	1.97	1.5
Gold	1970	2.99	2.4
OFHC (1/2 hard) copper	1790	2.02	1.5
Lead	760	2.74	2.2
Molybdenum	3660	1.59	1.3
Stainless steel (304)	2380	1.93	1.4
Tantalum	4340	1.67	1.3
Titanium	2260	1.23	1.0
Tungsten	4520	1.67	1.3

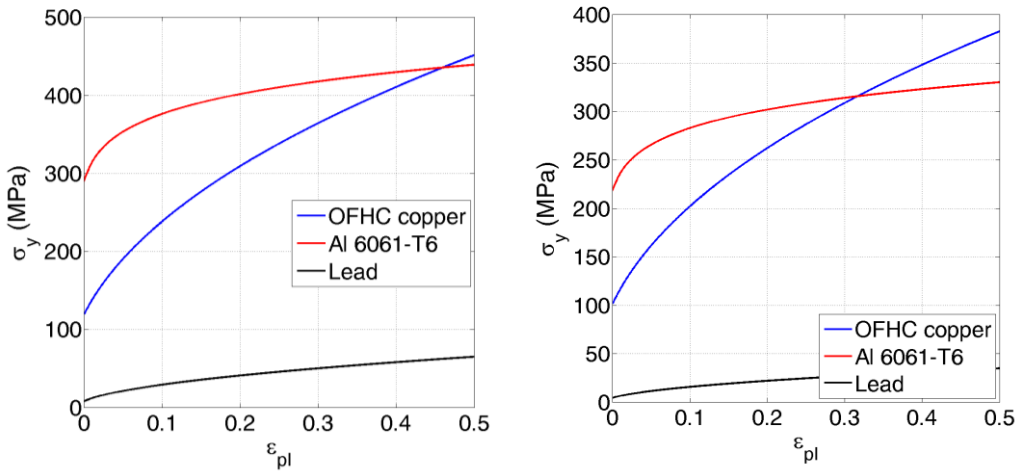

Fig. 4.3: S-G model for FCC materials, such as Al 6061-T6, OFHC (1/2 hard) copper and lead for two different temperatures: 300 K (left) and 700 K (right); $\varepsilon_{pl,i}$ = 0, P = 0 GPa.

In Fig. 4.3 and 4.4, the comparison between different materials for two temperatures are reported (pressure influence is neglected). In Fig. 4.3, three FCC materials are compared until the 50% of plastic strain. In Fig. 4.4 the same curves are shown for four

BCC materials. Comparing the two classes of materials, it can be concluded that, generally, in case of BCC material, the maximum strength is higher. In both cases, the temperature effect implies a reduction of the strength of the material and, consequently, the material has to reach higher values of plastic strain, before reaching the saturation condition.

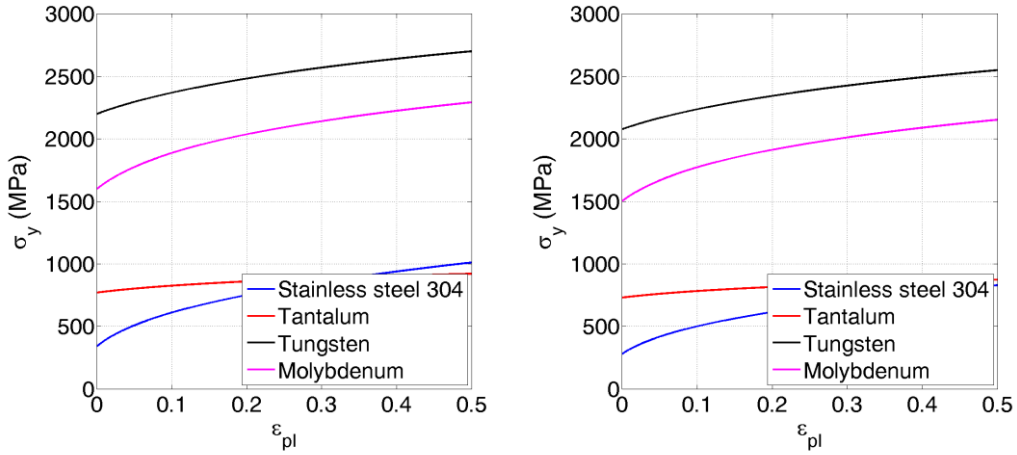

Fig. 4.4: S-G model for BCC materials, stainless steel, tantalum, tungsten and molybdenum for two different temperatures: 300 K (left) and 700 K (right); $\varepsilon_{pl,i}$ = 0, P = 0 GPa.

In LS-DYNA, the formulation is a little bit different from that reported in Eq. 4.5:

$$\begin{aligned}
\sigma_y &= \sigma_0^{'}\left[1 + b^{'}Pv^{1/3} - h\left(\frac{E_i - E_c}{3R^{'}} - 300\right)\right]\mathrm{e}^{\frac{fE_i}{E_m - E_i}} \\
\sigma_0^{'} &= \sigma_0\left[1 + \beta\left(\varepsilon_{pl,i} + \varepsilon_{pl}\right)\right]^n < \sigma_{\mathrm{MAX}} \\
G/G_0 &= \left[1 + bPv^{1/3} - h\left(\frac{E - E_c}{3R^{'}} - 300\right)\right]\mathrm{e}^{\frac{fE}{E_m - E}} \\
T_m &= T_{m0}\exp\left[2a\left(1 - v\right)\right]v^{-2(\gamma_0 - a - 1/3)}
\end{aligned} \tag{4.5b}$$

The coefficient *b* and *b'*, which define, respectively, the pressure/volume influence on the shear modulus and the yield stress, are considered to be different. The same was reported by Steinberg in the original work [3], while in [10], the author made the simplification assuming that the two coefficients are equal.

The other difference is related to the temperature influence. The heat capacity of solid is calculated starting from $R' = R\rho_0/A$, where R is the gas constant, ρ_0 the solid density and A the atomic weight. In the original formulation, there was not the exponential term,

defined in function of the total energy and the melting energy (E_m). Imposing $f = 0$, the set of equation 4.5b becomes identical to that of Eq. 4.5.

In [4], the model previously described was modified: the strain-rate sensitivity was added to the model proposed in [3], extending its validation in strain-rate range until 10^{-4} s^{-1}. The first equation reported in Eq. 4.5 was modified as follows:

$$\begin{aligned} \sigma_y &= \sigma_{\text{th}}\left(\dot{\varepsilon}_{pl}, T\right) G/G_0 + \sigma'_{\text{ath}} f'\left(\varepsilon_{pl}\right) G/G_0 \\ \sigma'_{\text{ath}} &= \sigma'_0\left[1+\beta\left(\varepsilon_{pl,i}+\varepsilon_{pl}\right)\right]^n < \sigma'_{\text{MAX}} \end{aligned} \tag{4.6}$$

in which σ_{th} is the thermally activated part of the stress, which is function of both temperature and strain-rate. The second term is the athermal component, which is similar in form to that of S-G model (third equation of Eq. 4.5).

In case of FCC materials, the thermal component is small, so the Eq. 4.6 coincides with the S-G model, in which σ_A is equal to the Hugoniot elastic limit. On the contrary for BCC material, the thermally activated part can be large and has to be taken into account.

In more details, the thermal component is obtained on the basis of the Hoge and Mukherjee formulation:

$$\dot{\varepsilon}_{pl} = \left(\frac{1}{C_1} \exp\left[\frac{2U_K}{k_b T} \left(1 - \frac{\sigma_{\text{th}}}{\sigma_P} \right)^2 \right] + \frac{C_2}{\sigma_{\text{th}}} \right)^{-1} \qquad \left(\sigma_{\text{th}} < \sigma_P\right) \tag{4.7}$$

in which σ_P is the Peierls stress, the parameters C_1, C_2 and U_k are phenomenological and depends on the mobile dislocation density, the Burgers vector, the average distance between barriers and the scattering of lattice phonons. The first term expresses the strain-rate in the discrete obstacle cutting regime, the second term expresses the linear relation between the thermal stress component and the strain rate in the phonon drag regime (very high strain-rate). The model is coupled in temperature and strain-rate for what concerns the discrete obstacle regime, while the phonon drag regime is temperature independent.

A lot of data for BCC materials for the S-L model can be found in [10] and some of them are summarized in Tables 4.6-4.9.

Table 4.6: S-L model parameters for various materials for the athermal component [10]

Material	σ'_0 **(GPa)**	σ'**max (GPa)**	β **(-)**	n **(-)**
Molybdenum	0.9	1.6	20	0.15
Steel (4340 RC 38)	1.0	2.5	2	0.5
Tantalum	0.375	0.450	22	0.283
Tungsten	1.1	1.5	24	0.19
Vanadium	0.150	0.830	10	0.10

Table 4.7: Density and S-L model parameters for various materials for the flow stress and shear modulus dependence by pressure and temperature [10]

Material	ρ_0 **(kg/dm^3)**	G_0 **(GPa)**	h_1 **(TPa^{-1})**	h_2 **(kK^{-1})**
Molybdenum	10.2	125	11.4	0.152
Steel (4340 RC 38)	7.81	80.1	20.6	0.3
Tantalum	16.69	69	14.5	0.13
Tungsten	19.3	160	9.38	0.138
Vanadium	6.1	48.1	10.2	0.206

Table 4.8: Specific heat and S-L model parameters for various materials for the melting temperature function [10]

Material	c_P **(J/kg/K)**	T_{m0} **(K)**	γ_0 **(-)**	a **(-)**
Molybdenum	243	3360	1.59	1.3
Steel (4340 RC 38)	448	2310	1.67	1.2
Tantalum	135	4340	1.67	1.3
Tungsten	129	4520	1.67	1.3
Vanadium	464	2640	1.40	1.2

Table 4.9: S-L model parameters for various materials for the athermal component [10]

Material	C_1 (μs^{-1})	C_2 (GPa μs)	U_k (eV)	σ_P *(GPa)*
Molybdenum	35.2	1.2	0.372	1.67
Steel (4340 RC 38)	3.6	2.4	0.31	0.70
Tantalum	0.71	2.4	0.31	0.82
Tungsten	0.71	12	0.31	1.60
Vanadium	0.071	12	0.31	0.80

In Fig. 4.5, the SL model for molybdenum, tantalum and tungsten are compared in terms of thermal stress vs. strain-rate in semi-log plane. The tantalum and stainless steel show quite similar strain-rate sensitivity. In case of tungsten, the strain-rate sensitivity is higher. Besides, for tungsten, the thermal stress behaviour varying the temperature (300, 600 and 900 K) is also analyzed. From the diagram of Fig. 4.5 (right), it is possible to conclude that: increasing the temperature the material is less strain-rate sensitive until higher value of strain-rate. After the threshold at which the material becomes strain-rate sensitive, then the slope of the thermal stress vs. strain-rate curve increases with temperature.

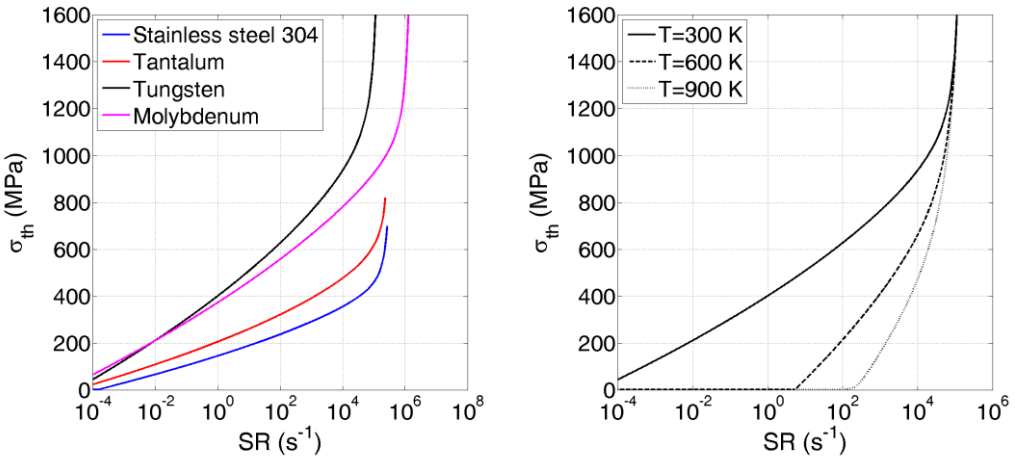

Fig. 4.5: S-L model: (left) comparison between stainless steel, tantalum and tungsten for the thermal stress component; (right) thermal stress component for tungsten at different temperatures for tungsten.

In Fig. 4.6 (left) the S-L and S-G model in the athermal component are compared for tantalum, tungsten and molybdenum, which are three materials for which it is possible to find both the models parameters (see [3, 10]). The athermal component in case of S-L model is low with respect to the S-G model, since in the S-L model the strain-rate contribution has to be summed (thermal component, see Eq. 4.6). On the contrary, the S-G model is thought to be applied in case of so high strain-rate that the sensitivity of strain-rate becomes negligible. In Fig 4.6 (right), the comparison is made in terms of flow stress (thermal plus athermal components), in correspondence to a strain-rate equal to 10^5 s^{-1}, which is the limit for the applicability of the S-G model, as indicated in [3]. A strain-rate equal to 10^5 s^{-1} corresponds to a thermal stress equal to 617 MPa for tantalum, 1424 MPa for tungsten and 926 MPa for molybdenum. As it is possible to appreciate, the comparison between the two models is better for the tantalum, for which S-G and S-L model becomes identical over 10^5 s^{-1}.

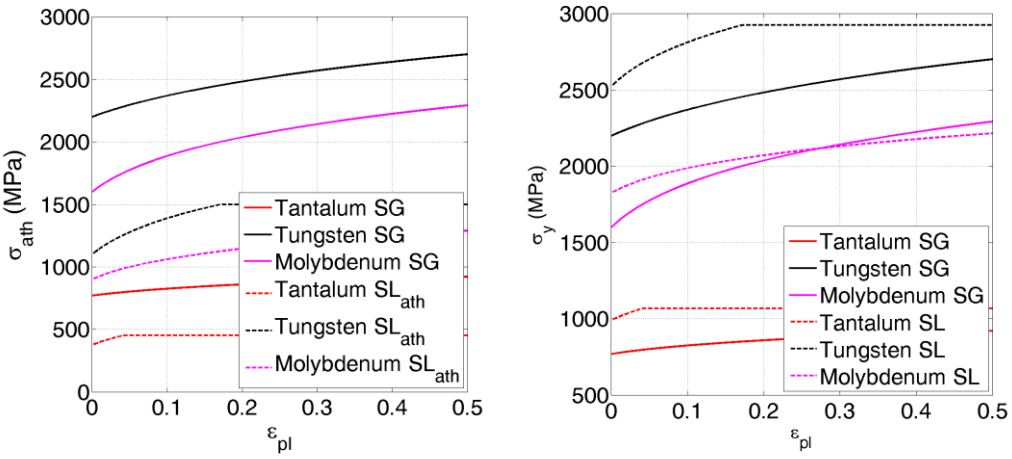

Fig. 4.6: S-G model vs. S-L model in case of tantalum, tungsten and molybdenum (BCC materials): (left) for the athermal component; (right) for the complete flow stress. The parameters are: T=300 K, $\varepsilon_{pl,i}$ = 0 and P = 0 GPa and for the diagram on the right a strain-rate of 10^5 s^{-1} is considered.

4.4 Failure model

A failure model can be associated to a strength material model in order to simulate the behaviour of a real material, which cannot support stresses greater than its limits.

The factors which influence the material failure are: the material properties and microstructure, the applied load (type of stress, strain-rate and temperature conditions) and

the ambient environment. Usually, depending on the failure mode, the materials are classified as brittle (such as ceramics or glass) or ductile (such as metals or polymers). The former class is characterized by having small plastic deformation and nearly flat fracture surfaces, which originates from a single crack propagation. Materials belonging to the latter class show large plastic deformation, usually with necking phenomena, and the cup-and-cone shaped failure surface, which are the results of nucleation, growth and coalescence of voids in the material.

The failure models can be divided into two categories [11]. In the first one the material is supposed to fail when locally it overcomes a limit for one or a certain number of variables (such as strain to fracture, tensile hydrostatic stress, maximum principal stress, etc.). This type of failure mechanism could be used to describe brittle failure or phenomena such as spalling. The second category includes the failure models based on the cumulative damage of the material: the material starts to be damaged if some limits on its properties are overcome. Than the damage evolution is controlled by a damage parameters, which can increase until the unity value is reach and this means that the material is completely failed. This type of failure mechanism could be used to describe ductile failure. Example of this category of failure models, which will be discussed more in depth later, are Johnson-Cook (J-C) model [12] and Bao-Wierzbicki (B-W) model [13].

4.4.1 Constant threshold model

In this paragraph, some failure models, in which the material is considered to be failed when locally it overcomes a limit for one or a certain number of variables are treated.

The strain to fracture is considered as one of the most important factors, which are involved in the failure process of a material. For this reason, the most simple failure model implies that fracture occurs when the equivalent plastic strain reaches an imposed critical value. The failure condition is:

$$\varepsilon_{eq} = \sqrt{\frac{2}{3}\left(\varepsilon_1^2 + \varepsilon_2^2 + \varepsilon_3^2\right)} = \varepsilon_f \tag{4.8}$$

in which ε_1, ε_2 and ε_3 are the principal strains. This model neglects any other influence on the failure, including triaxiality, temperature and strain-rate effects. Moreover, it implies

an equal behaviour both in tension and compression.

Another similar criterion is based on the maximum shear stress. As a matter of fact, it is widely recognized that fracture occurs on a plane in which the shear stress is maximum. In this case, the failure models assume the formulations:

$$\tau_{\mathrm{MAX}} = \max\left(\frac{\sigma_1 - \sigma_2}{2}, \frac{\sigma_2 - \sigma_3}{2}, \frac{\sigma_1 - \sigma_3}{2}\right) = \tau_f \tag{4.9}$$

in which σ_1, σ_2 and σ_3 are the principal stresses.

Similar failure models can be defined considering, instead of equivalent plastic strain or maximum shear stress, principal stress or strain.

Also the pressure can be used as failure parameter on which defining a failure model. The spalling defines the failure of a material in case of high hydrostatic tensile loads, which usually characterized all the phenomena in which a high compressive wave is reflected into a tensile one by a free surface. In this case, the negative pressure (correspondent to a hydrostatic tensile stress state) is lower bound. The material fails if:

$$p = -\frac{\sigma_1 + \sigma_2 + \sigma_3}{3} = p_{\mathrm{MIN}} \tag{4.10}$$

in which σ_1, σ_2 and σ_3 are the principal stresses. The pressure value for spalling failure for different materials can be found in [10] and are summarized in Table 4.10

Table 4.10: Spalling failure data for different materials [10]

Material	p_{MIN} **(GPa)**	**Material**	p_{MIN} **(GPa)**
Al 6061-T6	1.2	Molybdenum	1.5
OFHC copper	1.2	Tantalum	4.4
Lead	0.06	Titanium	2.5
Steel 4340	3.2	Tungsten	0.9

4.4.2 Johnson-Cook

The J-C failure model [12] was developed by Johnson and Cook in order to represent the effect of various parameters on the strain to fracture. It is a cumulative-damage fracture model considering strain, strain-rate, temperature and pressure influence: it accounts for the path dependence by accumulating damage during the deformation process. The material damage is evaluated defining the damage parameter *D* as follows:

$$D = \Sigma \frac{\Delta \varepsilon_{pl}}{\varepsilon_f} \tag{4.11}$$

in which $\Delta\varepsilon_{pl}$ is the equivalent plastic strain increment and ε_f is the equivalent strain to fracture for fixed conditions of plastic strain, strain-rate, temperature and pressure. The material is considered fractured if $D = 1$.

The strain at fracture is defined by the expression:

$$\varepsilon_f = \left(D_1 + D_2 \exp\left(D_3 \sigma^*\right)\right)\left(1 + D_4 \ln \frac{\dot{\varepsilon}_{\mathrm{pl}}}{\dot{\varepsilon}_0}\right)\left(1 - D_5 \left(\frac{T - T_r}{T_m - T_r}\right)\right) \tag{4.12}$$

which is very similar in the form to the strength material model of Eq. 4.1. The dimensionless variable $\sigma^* = \sigma_m / \sigma_{VM}$ is the ratio between the average of the three nominal stresses (equal to $-P$) and the Von Mises stress, which represents the triaxiality state of the loading condition. The Eq. 4.12 is defined for constant values of the variable σ^*, $\dot{\varepsilon}_{\mathrm{pl}}$, T and for σ^* less equal to 1.5. The five constants used to define the fracture behaviour are the parameter D_1,..., D_5, obtained by fitting experimental and numerical data of tensile and torsion tests. In Table 4.11 the coefficients for OFHC copper, Armco iron and 4340 steel are reported (see [12]). Since the coefficient D_3 is negative, the first term of the Eq. 4.12 indicates that the strain to fracture decreases increasing the hydrostatic tension.

In Fig. 4.7 the curves strain to failure vs. normalized stress are reported for the three materials at different strain-rate and temperature combinations (T=298 K @ 10^{-3}, 1 and 10^3 s^{-1} and 1 s^{-1} @ 240, 298 and 1000 K) in the triaxiality range between -0.2 to 1.5 (the same range shown by the authors in [12]). From the results it appears evident that the pressure over stress ratio is of fundamental importance in the definition of the strain to

fracture. In particular, when the pressure component increase, the strain to fracture decrease rapidly. The temperature and strain-rate effects, otherwise, seem to be less important.

Table 4.11: J-C cumulative-damage model parameters for various materials [12]

Material	D_1	D_2	D_3	D_4	D_5
OFHC copper	0.52	4.89	-3.03	0.014	1.12
Armco Iron	-2.20	5.43	-0.47	0.016	0.63
4340 steel	0.05	3.44	-2.12	0.002	0.61

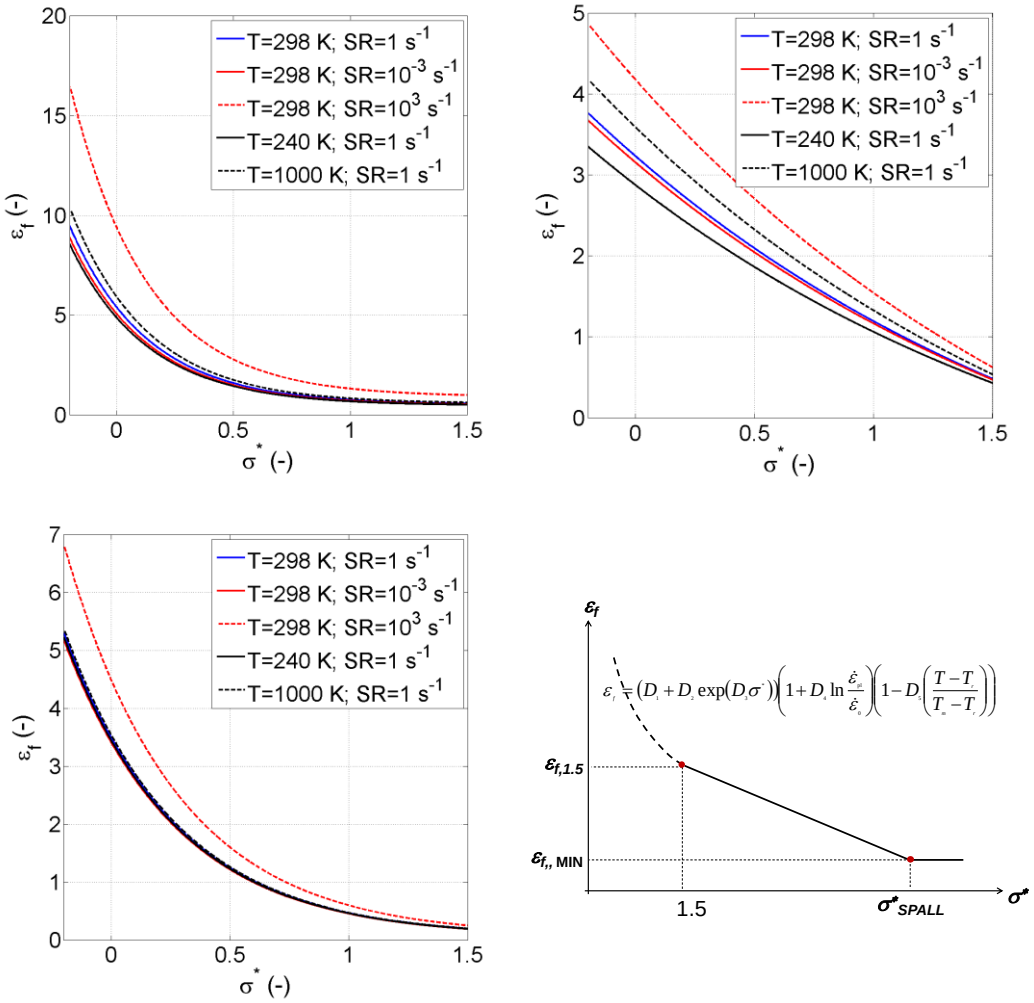

Fig. 4.7: J-C cumulative-damage model for different materials: OFHC copper (top left), Armco iron (top right) and 4340 steel (bottom left), with model parameters reported in Table 4.10; failure model in the range $\sigma^* > 1.5$: linear decreasing until the spall condition is reached (bottom right)

For high values of hydrostatic stress, or σ^* >1.5, a different formulation should be used. In this range, a linear decrease of the strain at fracture increasing σ* is used until a minimum threshold of strain ε_{fMIN}. The point at the transition between the two behaviour is calculated from Eq. 4.12 with σ^* = 1.5. The final point, correspondent to ε_{fMIN} is σ^* = σ^*_{spall}, which is defined as σ_{spall} /σ_{VM}. The trend of the failure model extended also in this range is reported in Fig. 4.7. In this case only a qualitative behaviour is shown since no data for this region are available in [12].

4.4.3 Bao-Wierzbicki

The strain intensity and the triaxiality level are the most important aspects to consider in the description of the fracture behaviour of ductile material. Usually, the strain to fracture is considered to be a good indicator and different works can be found in literature with the purpose to describe the influence of triaxiality. Generally, the investigation is limited to the ranges characterized by high positive values of triaxiality and negative ones.

The B-W failure model [13] was developed with the aim to extend the description in a wide range of triaxialities, based on the results obtained from different types of tests. This work was not proposed to obtain specific description of the fracture behaviour of different materials, but with the aim to describe the methodology and the procedure, which could be applied for any materials.

In [13], the analysis was conducted on 2024-T352 aluminium alloy. In more details, the triaxiality (σ^*) range investigated was between -1/3 and 0.95. The lower boundary is imposed by the compression test condition, in which fracture does not happen for any value of equivalent strain. For negative stress triaxiality (between -1/3 to 0) compression and upsetting tests were performed. For the low stress triaxiality (between 0 and 0.4) pure shear tests, combined shear and tension tests on a plate with a circular hole were performed. The triaxiality equal to zero was obtained from pure shear test, in which the hydrostatic component is null. In high triaxiality regime (between 0.4 and 0.95) conventional tensile tests were performed. The numerical simulations of all these types of tests were performed and the analysis of the fracture ductility was performed on them. The fracture locus describing the strain to fracture (ε_f) in function of the average stress

triaxiality obtained in each type of test was obtained fitting experimental and numerical results.

Table 4.12: Cumulative-damage B-W model: calibration of the fracture locus for Al 2024-T351 [13]

Range of σ^*	**Strain to fracture, ε_f**
$-\frac{1}{3} < \sigma^* < 0$	$\varepsilon_f = 0.1225\left(\sigma^* + \frac{1}{3}\right)^{-0.46}$
$0 \le \sigma^* < 0.4$	$\varepsilon_f = 1.9\sigma^{*2} - 0.18\sigma^* + 0.21$
$0.4 \le \sigma^* < 0.95$	$\varepsilon_f = 0.15\sigma^{*-1}$

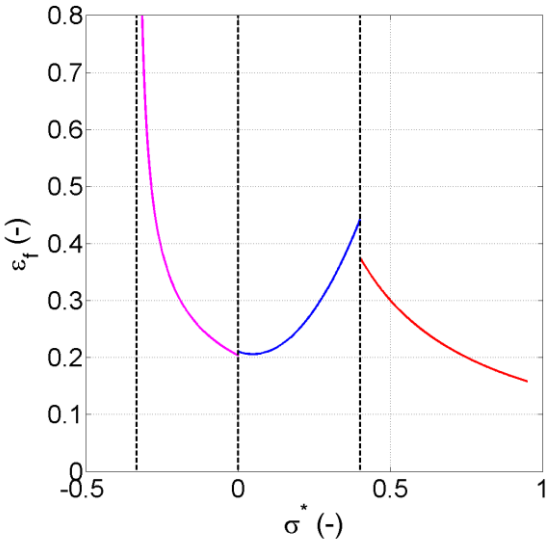

Fig. 4.8: B-W cumulative-damage model for Al2024-T351. Dependence of the strain to fracture on the stress triaxiality: identification of the different ranges.

Fig. 4.8 shows the result obtained for the investigated material in terms of ε_f vs. σ^* curve. The functions used to fit the experimental data are summarized in Table 4.12. The results show that for negative triaxialities, the strain to fracture decreases, until reaching a minimum in correspondence to pure shear test condition. Moreover, the strain to fracture goes to infinity for the limit given by the compression tests. In this region the shear fracture dominates the failure mechanism. In the high triaxiality range, the failure is governed by the formation of void and again the strain to fracture decreases, increasing

the triaxiality state. Between these two ranges, the fracture occurs due to a combination between shear and void growth and the strain to fracture increase with the triaxiality. The transition depends on the material and in this case it was found to be placed for σ^*=0.4.

4.5 Parameter identification

The main objective of this paragraph is describing a reliable method to be applied for getting strain-hardening, thermal and strain-rate parameters for a material model. The main objective is to be able to correctly reproduce the deformation process that occurs in high strain-rate scenario, in which the material reaches also high levels of plastic deformation and temperature.

If the material model is completely physically-based the model parameters are correlated to the physics and chemical material properties. Otherwise, if the material model is empirical (phenomenological), it is necessary to obtain the model coefficients and, usually, the approach is fitting analytically the experimental data. With this standard approach, the quality of the results could be affected by geometrical effects, that lead to non uniform stress-strain field within the specimen, and thermo-mechanical coupling in case of high strain-rates, when the thermal softening effects become more relevant. On the other hand, a numerical inverse method is useful to extract material strength parameters from experimental results in all the cases in which the stress and strain fields are not correctly described or predictable with an analytical model. Usually, this happens in specimens with no regular shape, in specimens in which some instability phenomena occur (e.g. the necking phenomena in tensile tests) or in dynamic tests, in which the strain-rate field is not uniform due to the stress wave propagation. Besides, the inverse method is also useful in case of high strain-rate tests, in which the adiabatic heating due to plastic work conversion into heat leads to thermal softening phenomena.

4.5.1 Numerical inverse method

The methodology used and described in this paragraph is based on a numerical inverse method, which is particularly useful to reproduce experimental results when the stress-strain fields in the specimen cannot be correctly described via analytical models. Furthermore, this procedure is useful to take into account thermal phenomena generally

affecting high strain-rate tests, in which the heat conversion of plastic work produces an adiabatic overheating. So, the applicability of this method is particularly indicated in special fields, such as aerospace engineering, ballistic, crashworthiness studies or particle accelerator technologies.

The use of a numerical inverse method for the material model parameters identification is now widespread thanks to the larger computing power available at lower cost. In any case, the difficulty is often the understanding of which are the best strategies to choose for taking advantage of the capabilities of the optimization methods applied to problem like system parameters identification. For this reason, the attention is focused on evaluating the most suitable strategy of material model parameters optimization to obtain the best fit between experimental data and numerical results. In this regards, it is important to determine which material model parameters can be considered as optimization variables and, for each of them, the most suitable range of variation.

It is important to remark that a material characterization must count on a specified analytical model from which the number of strength parameters and the types of experimental tests to be performed depend. For this reason, it is very important that experimental tests and numerical modelling go hand in hand in order to avoid both an inadequate and an overflowing number of data. So, first of all it is necessary to choose the material model on which it is consequently possible to plan the experimental tests. Then, the numerical model of each experimental test is built. The next aspect is the evaluation of the most suitable strategy of the parameters optimization, estimating the influence of each model parameter on both the stress-strain relationship and the optimization error. Finally, once the best optimization strategy has been identified, it is possible to apply the numerical inverse method to extract the model parameters for the investigated material.

The main steps of the procedure are: performing the experimental tests at different speeds and temperatures and optimizing the material parameters via numerical FEM simulation of the experimental tests, using the commercial code LSOPT [14] for the optimization phase and LS-DYNA [7] for the numerical simulations.

The numerical FE model-based optimization should be useful in order to avoid the following simplifying assumptions:

- ✓ uniaxial stress and strain inside the specimen. Actually, three-axial stress and strain fields inside the specimen are caused by the friction between specimen and testing equipment (see Fig. 4.9);

- ✓ constant strain-rate inside the specimen. Actually the strain rate is not constant and uniform during dynamic tests, thus influencing stain-rate sensitivity parameters;
- ✓ uniform temperature inside the specimen. Actually the temperature has a certain distribution proportional to the distribution of plastic strain inside the specimen, and the effect is even higher for dynamic tests. This should be considered to identify material strength parameters (see Fig. 4.9).

In the case presented, the chosen material model for the numerical simulation is the J-C model because since it very simple it is able to predict the mechanical behaviour of the materials under different loading conditions. Besides, as mentioned before, it is one of the most used material models, so it is implemented in many FEM codes.

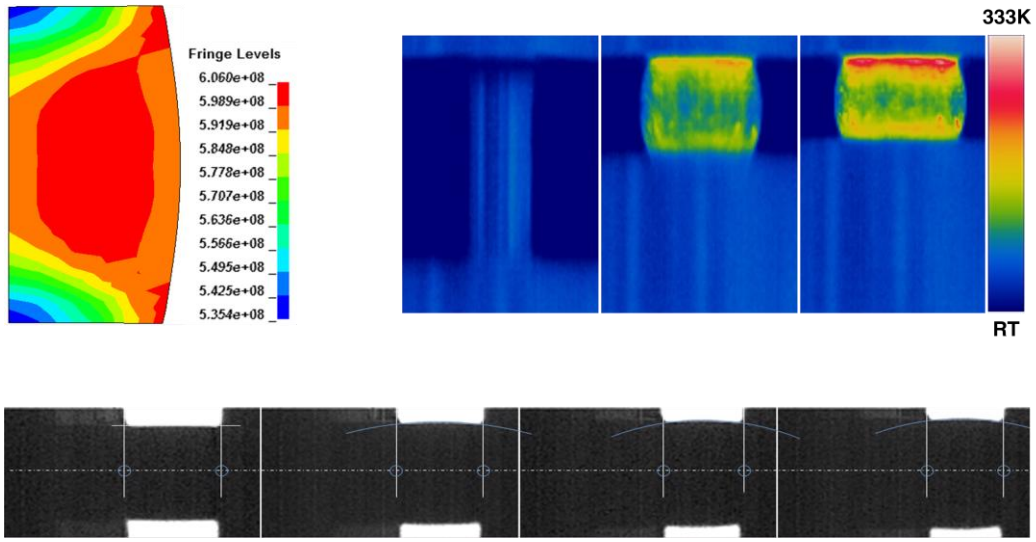

Fig. 4.9: Von Mises stress distribution (MPa) in a test nominally performed at 10^3 s^{-1}, left; temperature distribution over the specimen during a compression test performed at 100 mm/s filmed with a thermo-camera, right; sequence of steps of compressive experimental test performed with SHPB filmed with high velocity camera (20.000 fps): due to the friction between specimen and testing equipment the deformation is not uniform (barrelling, bottom).

As mentioned before, the objective of this paragraph is to describe a general methodology, which can be applied for different materials, when the J-C model is used in a wide range of temperatures and strain-rates. For this reason, the treatment is general, without any reference to a particular material or set of data. The application of this methodology can be found in [15], in which it is applied to the mechanical characterization of an alumina dispersion strengthened copper, known by the trade name GLIDCOP®.

Several authors used the J-C model, or its modified formulations, in order to investigate and describe problems such as ballistic impacts or, more in general, problems in which the strain-rates component is relevant. Different methods for the material model calibration starting from experimental data were also suggested. A lot of different types of materials have been described using the J-C model, such as steels [16, 17], aluminium alloys [18, 19], titanium alloys [20, 21], OFHC copper [22, 23], tungsten alloy [24] and super alloys [25], with mainly application in automotive, aerospace, nuclear and military fields. In some cases, the experimental data were fitted on the basis of the analytical formulation of the material model, while other works performed the calibration of FEM models starting from experimental results.

Recently, a multi-objective procedure for the material model identification has been proposed in [24]. In this paragraph, a similar approach is presented, but differently from [24], the method is based on the use of FE models.

According to the fact that the J-C material model is uncoupled in plastic strain, strain-rate and temperature effects, the experimental tests are managed exchanging one parameter at a time. So, experimental tests are performed at different speeds at room temperature and different temperatures at quasi-static loading conditions.

Any problems concerned to the damage and the failure of the specimen are neglected. In this way, under the hypothesis that the mechanical behaviour of the material is the same both in compression and in tension, it is chosen to consider only the compressive behaviour.

4.5.2 Multi-objective optimization

As mentioned before, this procedure implies that the experimental data are processed via a numerical inverse method based on FE numerical simulations. The main objective of an inverse optimization method is the determination of a selected set of unknown parameters in a numerical model: starting from a trial point, the unknown parameters are estimated iteratively by comparing experimentally measured with numerically computed quantities for the same material test conditions. The material characterization is reached varying the material strength parameters of the FE model, that reproduces the experimental loading and constraint conditions, and comparing the model results with the experimental data trying to obtain the best correlation. The great advantage of this

procedure is that no hypothesis about the internal specimen stress-strain field is made: in fact, the comparison is made in terms of macroscopic quantities that, in general, are force and displacement. The main disadvantage of the inverse methods is the high computational costs that these algorithms need: the optimization algorithms must perform iteratively a certain number of FE simulations, until the convergence is reached. Besides, the number of iterations dramatically increases when the degrees of freedom of the problem grow up or the trial parameters are far from the optimum ones.

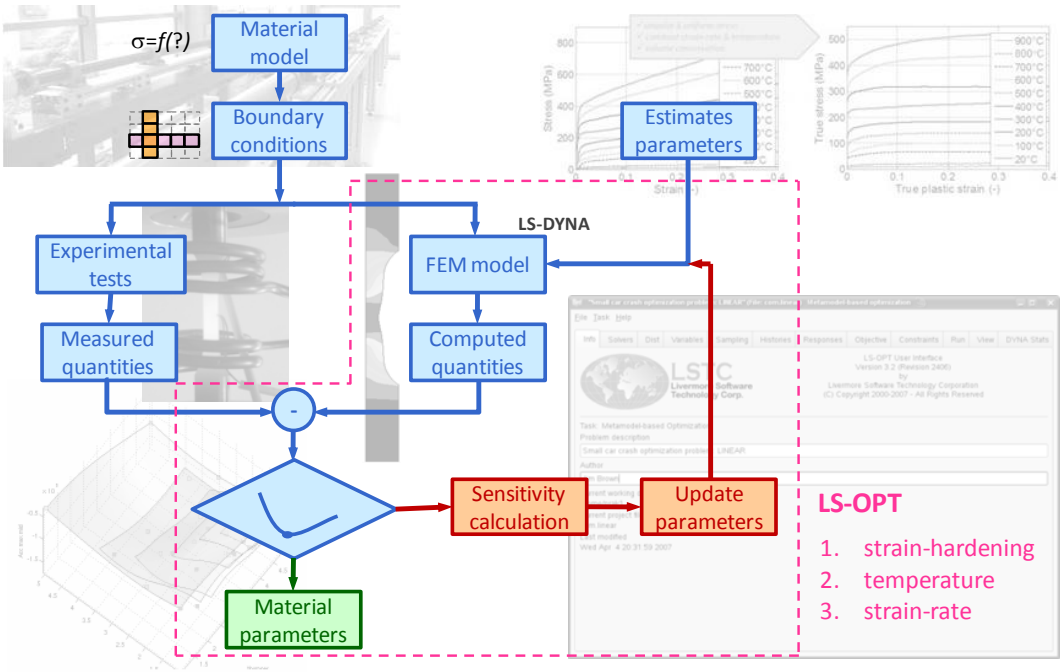

Fig. 4.10: Scheme of the numerical inverse method applied for the identification of the J-C model parameters.

The optimization of the parameters can be performed with a dedicated algorithm included in the software LS-OPT [14], that manages the parameters variation strategy, runs the numerical simulation, analyzes the results and extracts the optimum set of parameters for each iteration.

In particular, if a FE-based numerical inverse method is applied to a model like the J-C model, it requires necessarily a Multi-Objective Optimization (MOO), in which different objectives have to be satisfied simultaneously. As a matter of fact, both the thermal softening and the strain-rate parameters have to be estimated considering the variation of the corresponding properties (temperature and strain-rate) on the basis of multiple curves.

From these considerations, one could intend to perform a single optimization step to achieve the complete material model parameters identification. Actually, the problem is that a MOO could have different solutions, depending on the relative importance of the parameters and their influences on the global fit result, so this strategy is not easy to manage. The scheme of the procedure is reported in Fig. 4.10.

4.5.2.1 Steps of the optimization

Since J-C model is a multiplicative model it would be possible to optimize separately each set of parameters. So, a first optimization would be performed in order to extract the strain dependence. Then the thermal parameters would be obtained on the basis of the static tests at different temperatures. Finally, the last optimization would be done to extract the strain-rate coefficients from the dynamic tests. The scheme of the procedure is reported in Fig. 4.10.

Before starting with the optimization, since J-C model is a purely empirical model it is important to decide which of the parameters should be considered as optimization variables without any physical interpretation.

For what concerns the strain-hardening effect, three parameters (A, B and n) are available to perform the data fit and different procedures can be used: all the strain-hardening coefficients can be optimized or one of them can be fixed a priori and the other two optimized. As shown in [15], the latter method produce good results when A is fixed and B and n are optimized. This implies that the J-C model is able, after optimization of the other two parameters, to recover the estimate of the parameter A. Starting from this consideration and with the aim to achieve a higher level of uniqueness in the results (with three degrees of freedom, different sets of parameter could produce similar results), it is considered a good strategy fixing the parameter A a priori. The evaluation of A can be performed on the basis of the experimental data in case of quasi-static tests and A can be set equal to the yield strength or as the end of the linear behaviour.

In the J-C model, the temperature influence is expressed by the last term of the Eq. 4.2. The temperature parameters can be found on the basis of the experimental data obtained at different temperature in quasi-static loading conditions. The temperature parameters influence on the optimization process can be investigated starting from the experimental results, expressed in the dimensionless form, which is the ratio between the true stress-effective plastic strain curve for the experimental test at temperature T and the curve

corresponding to the experimental test performed at the lowest temperature. An example is reported in Fig. 4.11. Usually, the only J-C temperature parameter that is considered as an optimization variable is *m*. This approach could lead to a bad fit, due to the fact that a single degree of freedom could not be sufficient. An improvement could be achieved considering also T_m as an optimization variable: the addition of a variable adds a degree of freedom that allows achieving a better fit to the experimental data. A further improvement could be obtained if the temperature range considered for the optimization is limited. This range reduction is possible if the material strength is considered negligible under a fixed level or if, in the final application the material is supposed to work in a limited range in temperature. The result obtained from the combination of the last two aspects is shown in Fig. 4.11 with the dashed line.

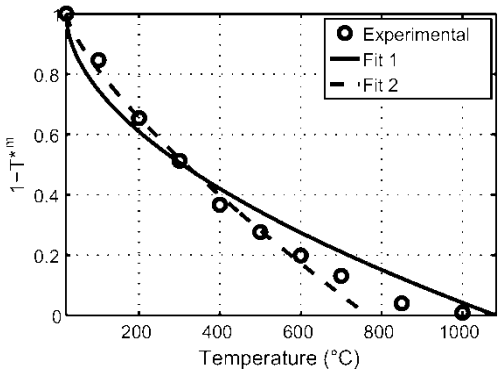

Fig. 4.11: Thermal softening term: fit of the experimental data, expressed in the dimensionless form, that is the ratio between the true stress-effective plastic strain curve for the experimental test at temperature T and the curve corresponding to the experimental test performed at the lowest temperature.

Another important consideration is about the possibility of optimizing *B*, *n*, *m* and T_m (for a fixed *A*) at the same time. In fact, if the strain dependence optimization is done on the experimental result of the test performed at the lowest temperature, it implies that this shape will be assigned to all the other curves at different temperatures. The temperature dependence optimization thus only generates the best scale function. On the other hand, if all the parameters are optimized at the same time, the reference shape is not constrained a priori, but it is left free to be optimized. This last optimization strategy is, however, quite critical considering that some variables have similar influences on the results. In this case, as mentioned before, the optimized solution could not be unequivocal.

Finally, the second term of the J-C model (Eq. 4.2) expresses the strain-rate influence on the material flow stress. Usually, only the parameter *C* is considered as an optimization

variable, while $\dot{\varepsilon}_0$ is set equal to 1 s^{-1}. In LS-DYNA, as discussed in the paragraph 4.1, this choice would mean that the strain-rate influence is neglected for all the experimental set data with strain-rate less than unity. If also $\dot{\varepsilon}_0$ is used as optimization variable, an improvement in the experimental data fit could be obtained, with the same considerations made for the temperature influence.

In Fig. 4.12, the results of the application of this procedure to the experimental campaign on GLIDCOP Al-15 are reported. The tests in temperature are performed in the range between 20° C and 1000 °C at quasi static loading conditions, obtained via a standard electro-mechanical machine. The tests in strain-rate cover a range between 10^{-3} and 10^{3} s^{-1}. The highest value of strain-rate is obtained via Split Hopkinson Pressure Bar setup. The diagrams show the comparison between experimental (markers) and numerical (solid line) load vs. stroke curves both varying temperature and strain-rate. This result corresponds to the case in which: B and n are optimized on the basis of the quasi-static data, m and Tm on the basis of the data in the limited range between 20 and 700 °C and C and $\dot{\varepsilon}_0$ on the basis of the data varying the strain-rate.

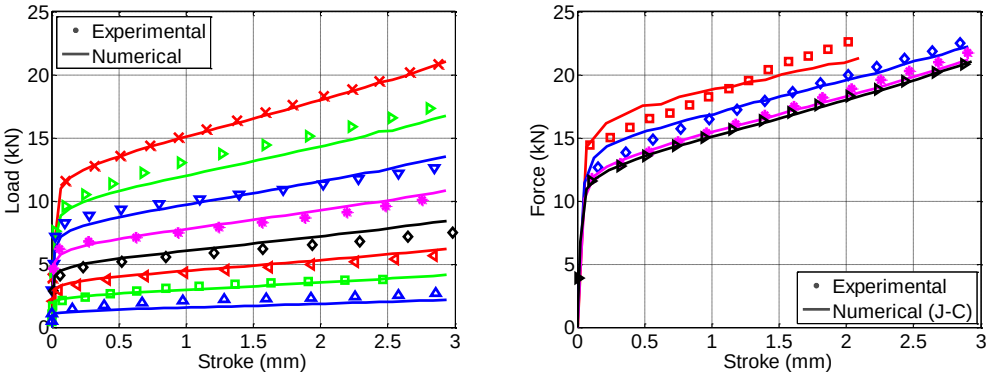

Fig. 4.12: Comparison between experimental data and numerical results for the tests at different temperatures: ✕ 20 °C, ▷ 100 °C, ▽ 200 °C, ✳ 300 °C, ◇ 400 °C, ◁ 500 °C, □ 600 °C and △ 700 °C.. Comparison between experimental data and numerical results for the tests at different strain-rates (case 2): □ 10^{3} s^{-1}, ◇ 10 s^{-1}, ✳ 10^{-1} s^{-1}, ▷ 10^{-3} s^{-1} (right).

References

[16] Johnson, G. R. and Cook, W. A., "A constitutive model and data for metals subjected to large strains, high strain rates and high temperatures", 7th International Symposium on Ballistic, 541-547 (1983).

[17] Zerilli, F.J. and Armstrong, R.W., "Dislocation-mechanics-based constitutive relations for material dynamics calculations". *Journal of Applied Physics*, Vol. 61 (1987).

[18] Steinberg, D.J., Cochran, S.G. and Guinan, M.W., "A constitutive model for metals applicable at high-strain rate". *Journal of Applied Physics*, **51**:1498 (1980).

[19] Steinberg, D.J. and Lund, C.M., "A constitutive model for strain rates from 10^{-4} to 10^{6} s^{-1}". *Journal de physique*, Symposium C3, (1988) **49**:433-440

[20] Follansbee, P.S. and Kocks, U.F., "A constitutive description of the deformation of copper based on the use of the mechanical threshold". *Acta Metallurgica*, **36** (1):81–93 (1988).

[21] Regazzoni, G., Kocks, U.F. and Follansbee, P.S., "Dislocation kinetics at high strain rates". *Acta Metall.* **12**:2865-2875 (1987).

[22] Gladman B et al., "LS-DYNA® Keyword User's Manual – Volume I – Version 971", LSTC (2007).

[23] "ANSYS AUTODYN User's Manual – Release 2010", ANSYS Inc. (2010).

[24] Kirk M. and Natishan M. E., "Predictive Material Modeling: Combining Fundamental Physics Understanding, Computational Methods and Empirically Observed Behavior", ASTM International, (2003) ISBN: 978-0803134720.

[25] Steinberg, D.J., Equation of State and Strength Properties of Selected Materials, Lawrence Livermore National Laboratory, UCRL-MA-106439, (1996).

[26] WierzbickiT., Bao Y., Lee Y.W. and Bai Y., "Calibration and evaluation of seven fracture models", International Journal of Mechanical Sciences **47**:719–743 (2005).

[27] Johnson, G. R. and Cook, W. A., Fracture characteristic of three metals subjected to various strains, strain rates, temperature and pressure. *Eng. Fract. Mech.* (1985) **2** (1): 31-48

[28] Bao, Y., Wierzbicki, T., On fracture locus in the equivalent strain and stress triaxiality space. Int. J. Mech. Sci. (2004) **46**: 81-98

[29] Stander, N., Roux, W., Goel, T., Eggleston, T., Craig, K. (2009) LS-OPT® User's manual – A Design Optimization And Probabilistic Analysis Tool For The Engineering Analysist, Version 4.0, Livermore Software Technology Corporation (LSTC)

[30] Scapin M., Peroni L., Peroni M., "Parameters identification in strain-rate and thermal sensitive visco-plastic material model for an alumina dispersion strengthened copper", International Journal of Impact Engineering 40-41:58-67 (2012).

[31] Dey, S., Børvik, T., Hopperstad, O. S., Leinum, J. R. Langseth, M., "The effect of target strength on the perforation of steel plates using three different projectile nose shapes", International Journal of Impact Engineering, **30**:1005-1038 (2004).

[32] Dey, S., Børvik, T., Hopperstad, O., J. R. Langseth, M., "On the influence of constitutive relation in projectile impact of steel plates", International Journal of Impact Engineering, **34**:464-486 (2007).

[33] Børvik, T., Clausen, A. H., Eriksson, M., Berstad, T., Hopperstad, O. S., Langseth, M., Experimental and numerical study on the perforation of AA6005-T6 panels, International Journal of Impact Engineering, **32**:35-64 (2005).

[34] Williams, B. W., Simha, C. H. M., Abedrabbo, N., Mayerb, R., Worswick, M. J., "Effect of anisotropy, kinematic hardening, and strain-rate sensitivity on the predicted axial crush response of hydroformed aluminium alloy tubes", International Journal of Impact Engineering, **37**:652-661 (2010)

[35] Hubert, W., Meyer, JR. and Kleponis, D. S., "Modeling the high strain rate behaviour of titanium undergoing ballistic impact and penetration", International Journal of Impact Engineering, **26**:509-521 (2001).

[36] Milani, A. S., Dabboussi, W., Nemes, J. A., Abeyaratne, R. C., "An improved multi-objective identification of Johnson–Cook material parameters", International Journal of Impact Engineering, **36**:294-302 (2009).

[37] Frutschy, K. J., Clifton, R. J., "High-temperature pressure-shear plate impact experiments on OFHC copper", J. Mech. Phys. Solids, **46**\10:1723-1743 (1998).

[38] Zhang, B., Shim, V. P. W., "Determination of inelastic heat fraction of OFHC copper through dynamic compression", International Journal of Impact Engineering, **37**:50-68 (2010).

[39] Rohr, I., Nahme, H., Thoma, K., Anderson Jr., C. E., "Material characterisation and constitutive modelling of a tungsten-sintered alloy for a wide range of strain rates", International Journal of Impact Engineering, **35**:811-819 (2008).

[40] Macdougall, D., Determination of the plastic work converted to heat using radiometry, Experimental Mechanics, **40**:298-306 (2000)

5. High energy particle beam impacts

In this chapter the shock-wave propagation in matter, due to the interaction of high energy particle beams with solid targets is analysed. The main objective of this study is to build safe and reliable numerical models able to estimate the damage provoked by such events in the Large Hadron Collider (LHC). In the first part of the chapter, there is a general introduction on the LHC and an overview on the study performed on it. Then, the interaction between intense beams and solid targets is investigated from a qualitative and phenomenological point of view. This allows the comprehension of the involved phenomena, which is necessary for the construction of the numerical model, described in the last part of the chapter.

This work is developed in accordance with the European project EuCARD (European Coordination for Accelerator Research & Development), which is co-funded by the European Commission within the Framework Programme 7 Capacities Specific Programme. In more details, the Work Package (WP) 8 is involved. The WP8, named ColMat, Collimations & Materials for higher beam power beam, has as main objectives the development of material and machine components related to collimation system and intercepting devices.

Particle accelerators [1] act as microscopes for such a complex research. They are complex machine used to accelerate and collide charged elementary particles (electrons, protons and ionized atoms) at very high kinetic energy, generating a multitude of short life sub-atomic particles. The investigation of matter in these extreme conditions can be compared with the status of the universe in the first moments after the “Big Bang”. The higher the energy of the colliding beams, the wider the spectrum of the generable sub-atomic particles. It is in this perspective that the project of building the Large Hadron

Collider (LHC) [2] at the European Organization for Nuclear Research (CERN, Geneva) was approved.

The LHC [3, 4] is a circular accelerator with a 26.659 km circumference situated at the border between Switzerland and France at an average depth of 100 m underground (see Fig. 5.1). This machine mainly accelerates and collides two counter-circulating proton beams. Each proton beam consists of up to 3×10^{14} protons at 7 TeV (project condition), so when the protons collide the collision energy is 14 TeV. In nominal operating conditions, the beam has 2808 bunches each having 1.15×10^{11} protons. The bunch length is 0.5 to 1 ns and the time between two successive bunches is 25 ns, so the duration of the bunch train is about 72 μs.

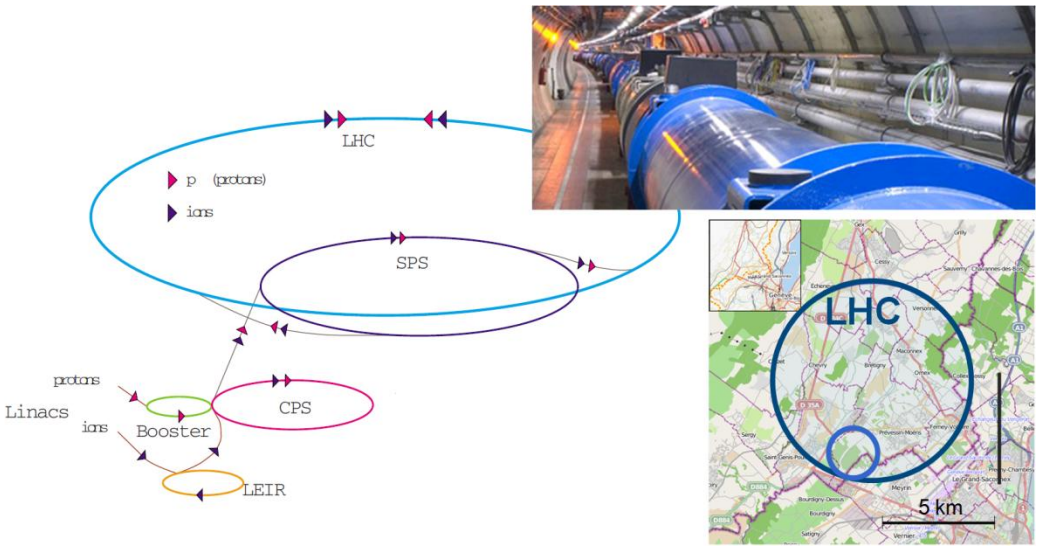

Fig. 5.1: The Large Hadron Collider: injection complex.

The total energy stored in each beam at maximum energy is about 350 MJ, two orders of magnitude higher than other machine such as Tevatron or HERA [4]. This large amount of energy (sufficient to melt more than 500 kg of copper) is potentially destructive for accelerator components having direct interaction with particles (e.g. the collimation system) in case of uncontrolled beam loss. Accidental events, in which a fraction of the proton beam is lost and directly impacts e.g. on the collimator jaws, should occur with a low probability, however, an assessment of possible structural damages is needed. An accurate prediction of the reliability and robustness is quite difficult, since beam-induced damage for high energy and high intensity impacts occurs in a regime in which the possibility to perform experimental tests is limited. For this reason, it is of fundamental

importance to develop reliable methods and accurate models to estimate the damage occurring during a beam impact.

When high energy particles are passing through a material, they lose energy by ionization and eventually interact inelastically generating a particle shower composed by particles at lower energy. As the speed of secondary particles decreases, the energy is transferred to the material lattice increasing its temperature. This provokes a dynamic response of the structure, entailing thermal stress waves and thermally induced vibrations, with in some cases the failure of the component. The pressure and temperature increase and the materials may reach its melting temperature or vaporize. The remaining part of the material is characterized by high values of plastic strain, strain-rate and temperature.

These considerations exemplify the complexity of the problem, which needs a multi-physics approach to be completely examined. As a matter of fact, different subjects are involved, such as physics, thermodynamics, engineering and materials science.

In order to correctly simulate the thermo-mechanical response of the material it is necessary to take into account both the hydrodynamic behaviour, adopting a dedicated Equation Of State (EOS), and the deviatoric behaviour, resorting to a dedicated strength material model.

5.1 State of the art

Before describing the implemented methods, a short discussion about the approaches developed by other researchers is presented. As a matter of fact, in literature different approaches to solve similar problems can be found.

In [5] the study of the thermo-mechanical effects induced in solids by high energy particles beams is carried out via two different approaches: an analytical method and a numerical one. Regarding the numerical approach, the thermo-structural analysis is performed using the commercial code ANSYS. The starting point of the analysis is the energy map on the component calculated using FLUKA code, which is converted in a thermal power distribution and used as input for the solution of the thermal problem, so the temperature distribution is calculated as a function of space and time. The results of temperature analysis are used as nodal loads for the structural analysis, so dynamic thermal stresses and displacements are evaluated. Finally, a quasi-static analysis is performed in order to calculate potential permanent deformations of the structure. As an

example, in Fig. 5.1, the temperature distribution on the jaw assembly of a collimator of the LHC, obtained in [5] for the accidental case of injection error is reported. This is then used for estimating the permanent deflection of the metal support.

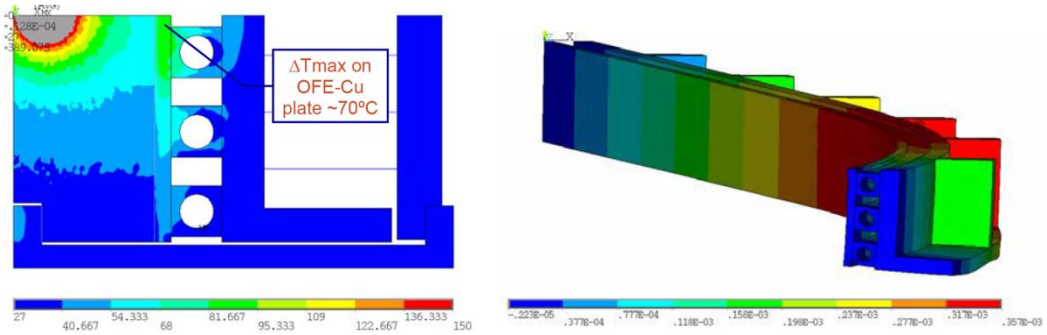

Fig. 5.2 Temperature distribution (°C) after the thermal shock at the hottest cross-section of the jaw assembly (left); residual deflection of the metal support (right).

A similar approach is carried out in [6, 7], in which the energy calculation on the material, resulting from high energy particles beam impact with a solid target is performed via MARS code. From the energy map the temperature rise is calculated and used in LS-DYNA (for an explicit analysis) or ANSYS (for an implicit analysis) code to calculate the dynamic stresses in the target.

It is important to note that, in these two approaches, the calculation of the temperature from the energy map is performed without using an equation of state, but simply considering the transformation in a solid material and using, as conversion factor, the heat capacity at constant volume for the solid phase. Actually, since the energy levels involved are very high, the material could undergo changes of state, so the use of an equation of state is needed in order to correctly evaluate the state of the material.

In this sense, a lot of works were performed by Tahir and co-authors (see e.g. [8-11]). The same type of analysis was performed on different materials (carbon, copper and tungsten), target dimensions and beam parameters (particle energy, standard deviation of the Gaussian distribution of the beam intensity, number of bunches). In all of these works the energy map calculation was performed using FLUKA code and the material response was numerically simulated via the hydro-code BIG-2, in order to calculate pressure, temperature and density on the hit material. To do this a sophisticate three-phase equation of state is used, see e.g. the EOS for copper reported in Fig. 5.3. The limitations are represented by the fact that BIG-2 is only a two-dimensional code with a pure hydrodynamic solver, so the deviatoric part of the stress is neglected. This assumption can

be valid in the part of the material closer to the beam impact point, while the strength of the material is by no means negligible in the remaining portion of material.

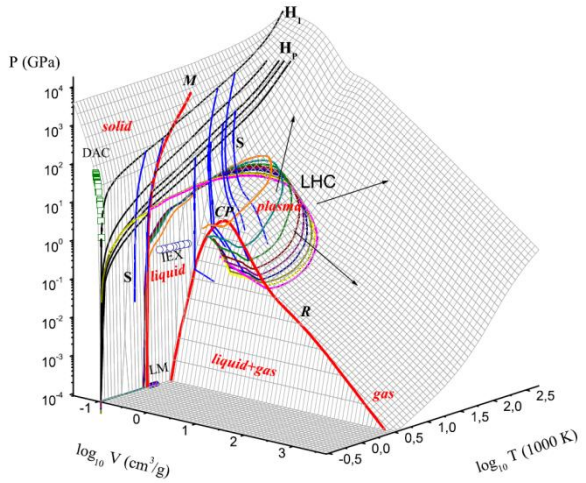

Fig. 5.3 EOS surface in the pressure-volume-temperature for copper [11].

As example of result obtained by Tahir and his co-authors, in Fig. 5.4, the results for the case in which a cylindrical solid target is irradiated along its axis by one of the two proton beams at 7 TeV of the LHC. The results are shown after 9500 ns from the impact in terms of energy deposited, pressure, density and state of the matter.

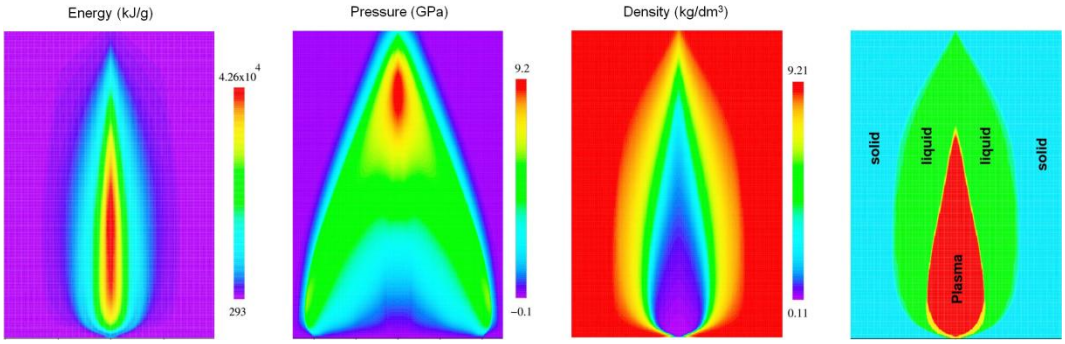

Fig. 5.4 Results obtained in [11] for the case of impact of the full LHC beam against a cylindrical copper target impacted at the centre of one face: 4 cm of radius (→), 500 cm of length (↑), the radial dimension is amplified.

Ryazanov et al. [12] developed a work complementary to the work of Tahir et al. [8], in which both theoretical and numerical models were developed in order to describe the consequences in the materials of the LHC collimation system in case of multi-bunch 7 TeV proton beam impact. In more details, the study was for the estimation of physical and

mechanical properties changes: the interaction between the material and the high energy beam produces the formation of a cascade of secondary fast particles that leads to the formation of shock-wave and radiation damage in the material. In [12], as first approximation, only the shockwave formation was considered from a pure hydrodynamic point of view for a two-dimensional model representing a cylindrical geometry. This theoretical model takes in account phenomena such as the ionization, the electronic excitation and the energy transfer from the excited electronic subsystem to the ionic one, due to the electron-phonon coupling. Besides, in [12], some preliminary numerical results of the distributions of density, pressure and temperature were also shown.

The purpose of this study is to analyze simultaneously the two aspects: the deviatoric behaviour and the hydrodynamic one, using the FE code LS-DYNA. LS-DYNA [13] is a general purpose transient dynamic finite element program including an implicit and explicit solver with thermo-mechanical and highly non-linear capabilities. This code is often used to solve impact problems also for nuclear applications and particle accelerator technology. In this sense a previous study is developed in [14], in which a coupled mechanical, thermal and electro-magnetic simulation is performed. So, the problem is quite different, but the approach can be similar. In fact, also in [14] the problem is linked with a rise in temperature that can melt or vaporize a portion of material. The difference is the cause of the heating: the temperature does not rise due to the impact of a high energy proton beam, but due to the Joule effect induced in material by a current. The simulations are performed using the LS-DYNA code, in which there is the possibility to implement a user-defined EOS. In [14] the three-phase equation of state GRAY is implemented and the input energy distribution comes from the electromagnetic solver.

5.2 Interaction between a particle beam and a solid target

As mentioned in the introduction, the energy stored in LHC is unprecedented and potentially destructive for the accelerator equipments having direct interaction with high energy particles. High energetic beams may interact with several components present in particle accelerators, so it is of primary importance to predict the extension of the possible damage.

In general, in case of interaction between high energy particles (protons) beam and a metallic material three main dynamic response regimes may occur. This depends on

several parameters, mainly the deposited energy, the energy density, the interaction duration and the material strength. The first possibility is the case in which the induced stress waves and the vibrations remain in the elastic domain. In this case the deposited energy density is low, the changes in density are negligible and the stress waves travel in the material at the speed of sound. On the other hand, for medium energy levels, the stress waves are generated in the plastic domain. This implies that the velocity of the waves is lower than the elastic domain speed and permanent deformations occur in the component, also once the load is over. The last case implies that a large amount of energy is delivered on the component. In the matter there is the initiation of shock-waves, in which there is a nearly discontinuous change in the characteristic of the medium (pressure, temperature and density). The discontinuity moves with a supersonic velocity and this makes the mass transport phenomenon to become relevant. Besides, in the material close to the hit zone the encountered temperatures are very high and two possible situations can arise, see Royce [15]. If the energy deposition is very quick, such that the deposition time is shorter than the system hydrodynamic characteristic time, the material density remains near to the normal density (isochoric transformation). Nevertheless, the temperature and the pressure increase and reach very high value. Once the hydrodynamic rarefaction process starts, the material can expand reaching lower values of density and pressure. This same evolution there is also in case of slow energy deposition process: the material reaches directly a condition characterized by low pressure and density because the hydrodynamic characteristic time is faster than the energy deposition rate.

LHC is a complex machine and the type of thermal load depends of intensity of the particle loss and on the radiation field. In normal situations, a low intensity continuous proton impact on a material generates simply a constant energy deposition over a long period (from some second up to few hours). In this case thermal stresses and deformations take place, but no dynamic response can usually be observed. If the rate of interaction increases (e.g. in case of abnormal beam impacts), energy is rapidly deposited in time-scales of the order of microseconds or nanoseconds. This load condition typically entails a dynamic response of the structure. The resulting thermal stresses and deformations may affect the integrity or the proper functionality of the hit equipments. From this it is clear that an in-depth thermo-mechanical analysis is strongly necessary.

Interaction between high energy particle beams and solids can be considered from a structural point of view as an energy deposition inducing a sudden non uniform

temperature increase. In function of which part of material is investigated the behaviour is different (see Fig. 5.4 and 5.5).

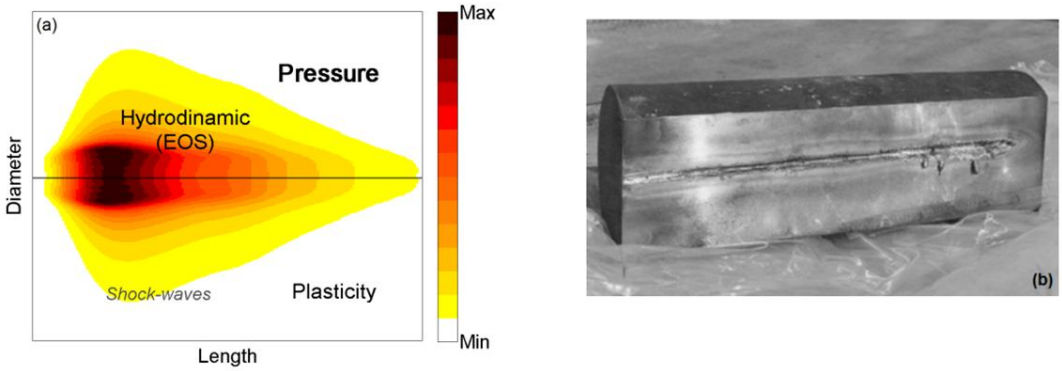

Fig. 5.5 Pressure distribution in case of impact between the high energy beam and a solid target (a); damage on a metal target due to the impact (b).

In the material part closest to the beam, the pressure and temperature increase and the materials could arrive at its melting temperature or vaporize, depending on the loading condition. The material response in this case is correctly described only using an equation of state, which is able to describe the hydrodynamic behaviour, while in this portion of material the deviatoric stress is totally negligible. On the other hand, the remaining part of the material, which remains solid, is characterized by high values of plastic strain, strain-rate and temperature, so the response is related with the strength material model used.

The evaluation of thermal loads on the hit material is performed by the FLUKA Team at CERN, using the FLUKA particle physics MonteCarlo simulation package [16, 17]. Then, the FLUKA result is used as input for the thermo-mechanical analysis.

5.2.1 Material requirements

Given the extreme loading conditions, the materials of the machine components, which can directly interact with the beam, should have particular properties; see the report written by Schmidt et al. [18]. The ideal material used for this application and generally in nuclear applications (e.g. see [19, 20]), should present good electrical and thermal conductivities, low ability to absorb elementary particles, low coefficient of thermal expansion and, finally, good mechanical properties, such as high stiffness, strength and shock resilience. Moreover, the performance issues are essentially and directly correlated

to the material abilities to maintain these key properties also in more extreme conditions (i.e. accidental cases), in which they should also absorb the beam-induced shock.

Usually, in order to cope with all the material requirements, a composite approach is used. Results of experimental irradiation studies performed on several materials were presented by Schmidt et al. in the report [18]. These studies showed that carbon composite exhibits dramatic reduction of the stability of the thermal expansion coefficient in case of high level of radiation. Similar problems were found also in graphite, in which the radiation produces also the reduction of thermal and electrical conductivities. On the other hand, encouraging results in case of proton irradiation were obtained for copper, GLIDCOP® (alumina dispersion strengthened copper), Invar, Ti-6Al-4V alloy and AlBeMet. Currently, the research is oriented on metal-diamond materials, such as copper-diamond, molybdenum diamond and silver-diamond, since these types of materials should satisfy all the above-mentioned requirements [21].

5.3 Numerical model

In such extreme cases the understanding of the phenomenon evolution is fundamental, for the prediction of the damage on hit targets consequent to a high energy deposition. In order to achieve this goal, numerical models, using the FE code LS-DYNA are built. The case studied regard the impact of 8 or more bunches of protons at 7 or 5 TeV from LHC.

The proton beam of LHC is not continuous, but it is divided in bunches. Each bunch contains at maximum 1.15×10^{11} protons and has a time duration of 0.5 or 1 ns, while the distance between bunches is a multiple of 25 ns (can be 25, 50, 75, ...). In all the cases analyzed and reported in the next chapters, the bunch length is considered to be 0.5 ns and the bunch spacing 25 ns: high luminosity is obtained only with 25 ns spacing.

The examined targets are cylinders with 1 m of length and 5 mm of radius made in copper or tungsten (see chapter 6) and parallelepipeds (21×35×1000 mm) made in tungsten (see chapter 7). For both the target types, the protons beam at 7 TeV impacts perpendicular at the centre of one face. Another case is also considered, in which a more complex structure, representing a Target Collimator tertiary (TCT) [22], is investigated. In this case, the geometry is a parallelepiped in tungsten, which is the insert of a C-structure made in copper. On this structure, the case analyzed regards the impacts of a 5 TeV proton beam near to the free surface in tungsten.

In general, the built numerical models represent the irradiated parts of bigger components. This means that the external surface is not modelled as a free surface, so there are not any reflections to the boundary, simulating, in this way, the presence of other material. In general, these cases represent an abnormal situation in which the beam impacts at full power directly against the solid target. The cylindrical geometry is investigated using a 2D-axisymmetric model, while for the parallelepiped a 3D model is used. As example, in Fig. 5.6, the scheme of the 2D-axisymmetric model is reported.

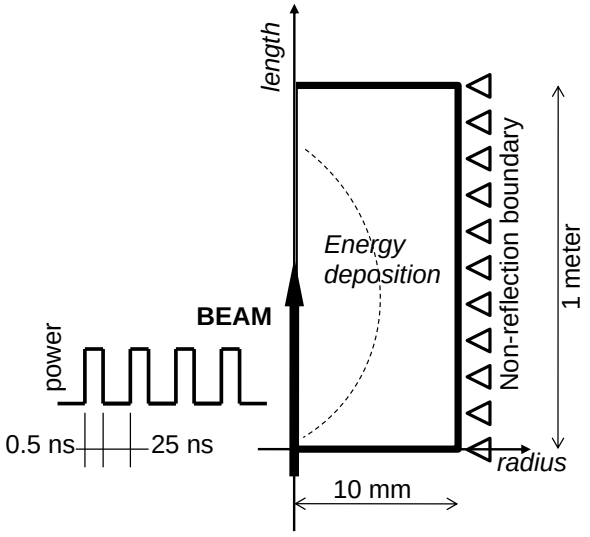

Fig. 5.6: Numerical model: cylindrical bar (10 mm of radius and 1 m of length) hit perpendicularly in the centre of one face. The dashed line identifies qualitatively the area hit by the beam, in which the energy deposition is more significant.

As mentioned before, the evaluation of thermal loads on the impacted material is performed by the FLUKA Team at CERN, using the statistical code, called FLUKA [16, 17], which is based on the Monte-Carlo method. The FLUKA code calculates the map of the energy density absorption in the matter in function of the spatial coordinates. The value of energy (GeV/cm^3) is calculated for each bin (element mesh) in which the considered target is divided. The calculation takes into account a large number of primaries (e.g. 70000), ensuring statistical errors not exceeding a few percents over the whole target component and much lower in the peak region, for the adopted scoring mesh and then the results are normalized to one ideal proton. This means that, sampling from a Gaussian distribution, adding all the contributions up, and dividing by the number of sampled particles, FLUKA result turns out to be representative of the whole distribution. The FLUKA results regard the interaction between the matter and a single proton. Finally,

it is possible to rescale the FLUKA map by the real bunch intensity (e.g. 1.15×10^{11} protons).

The provided FLUKA maps are used as starting point in the thermo-mechanical simulations, under the hypothesis of isolated bunches. This means that the reactions generated by the first bunch are assumed to be finished before the arrival of the second bunch and so on. The assumption is reasonable since a relativistic particle takes about 3 ns to cover 1 m in vacuum. The particles decays, generated for each primary collision, are not yet spent in the time between two successive bunches (25 ns) but most of them are far enough (5-8 m) to no longer be considered. This is true excluding the low energy neutrons, the nuclear reactions products in case of fragmentation and any particles with a decay time of about nanosecond or microsecond.

The FLUKA calculation can be strictly considered correct only for the first bunch, which impacts against the pristine material, on which the calculation is performed. The next bunches encounters a material, with differences in some chemical, physical and mechanical properties with respect to the pristine one, due to the energy absorption. In order to acquire the skills needed to deal with this issue, in the first numerical simulations, the energy map calculated for the first bunch is used without modifications also for the successive ones (see chapter 6). Then, the improvement in the numerical simulations leads to take into account for the modification of the material properties. To do this a routine for the soft coupling between FLUKA and LS-DYNA is developed in collaboration with the FLUKA Team at CERN (see chapter 7).

In all the cases, as mentioned before, the main goal is to simulate both the hydrodynamic and the mechanical response of the material hit by the proton beam. As a consequence, the numerical models need for the definition of both the EOS and the strength material model of the materials involved in the impact.

5.3.4 EOS

In the FE code LS-DYNA [13], as anticipated in the chapter 3, several EOS are implemented, which however, are suitable for the description of the thermo-mechanical behaviour of materials in limited parts of the entire $P = f(\rho,E)$ surface.

For the case of high energy particle beam interaction with matter, given the high amount of energy introduced in the material, it is necessary to extend the EOS definition,

in order to cover wide ranges in density and energy. For this reason, the best solution is to use the SESAME EOS [23].

Unfortunately, in LS-DYNA, this tabular EOS is not implemented. The problem is solved performing an interpolation on the basis of the formulation of one of the EOS implemented in the FE code. The simplicity in its formulation and the fact that it is the only one for which (in LS-DYNA) it is possible to define a power profile in function of time lead to choose of a polynomial formulation (*EOS_POLYNOMIAL_WITH_ENERGY_LEAK). The need of the definition of a power profile in function of time is correlated to the beam profile itself, especially in case of multi-bunch impact.

The coefficients of the interpolation are obtained ad hoc for each element of the numerical model and are updated before the impact of the new bunch. This procedure is based on the fact that different simulations are performed for the impact of each bunch. The management of the procedure is performed by an external routine developed in Matlab. The routine deals with: generation of the numerical model, assignment to each element of the FE mesh of the correct energy coming from the FLUKA map, interpolation of the tabular EOS, running of the simulations, analysis of the results and definition of the restart procedure. In the following, the procedure for the polynomial coefficients identification is described.

First of all, it is necessary to specify that the interpolation is performed ad hoc for each element, since in LS-DYNA the only way to introduce an external energy into the model is passing through the EOS routine.

In order to limit the computational time taken for the interpolation, a maximum number of 10000 EOS is used in LS-DYNA simulations. If the FLUKA model has more than 10000 bins, then a discretization algorithm is applied before the energy assignment to the FE elements. The polynomial coefficients identification is repeated before the simulation of the impact of each bunch, so once for each simulation. This is correlated to the fact that, since the great amount of energy introduced in the material by a bunch, the state of the matter in the P-ρ-E plane can vary a lot in comparison to the previous state.

The scheme for the polynomial coefficients identification is summarized below, in reference to the scheme of Fig. 5.7. The case reported to explain the procedure regards the confined impact (the impact occur inside the target and not near to a free surface). In Fig. 5.7, the pressure vs. internal energy plane, varying the density, is reported. The gray lines

in the background represent the isodensity curves defined by the SESAME EOS. The dashed lines identifies the deposition phase (bunch duration) and the solid lines the expansion phase (time between two successive bunches).

In Fig. 5.7, the impact of two bunches is reported: this corresponds to an equivalent number of simulations. As mentioned in the introduction, the deposition phase is isochoric. The arrival of the bunch pulse, obviously, modified the precedent matter condition: in particular, there is an increment in the energy of the matter. Since the impact is quite short, the hydrodynamic response of the material cannot start, so the jump in energy is done along the density curve characteristic of the previous state. This implies that a new value in pressure is reached, which is univocally identified from the new energy and density conditions. The global result is that instantaneously the material reaches a different (greater) pressure. This means that is not strictly necessary to perform the numerical simulation of this phase. As a matter of fact, knowing the starting condition in terms of energy and density, the final state, in terms of pressure, is reached keeping the density constant and transforming the deposited energy into a pressure load. In conclusion, the final state, on the EOS, in which each element is after the bunch arrive, is known a priori and can be used to identify the range where performing the interpolation.

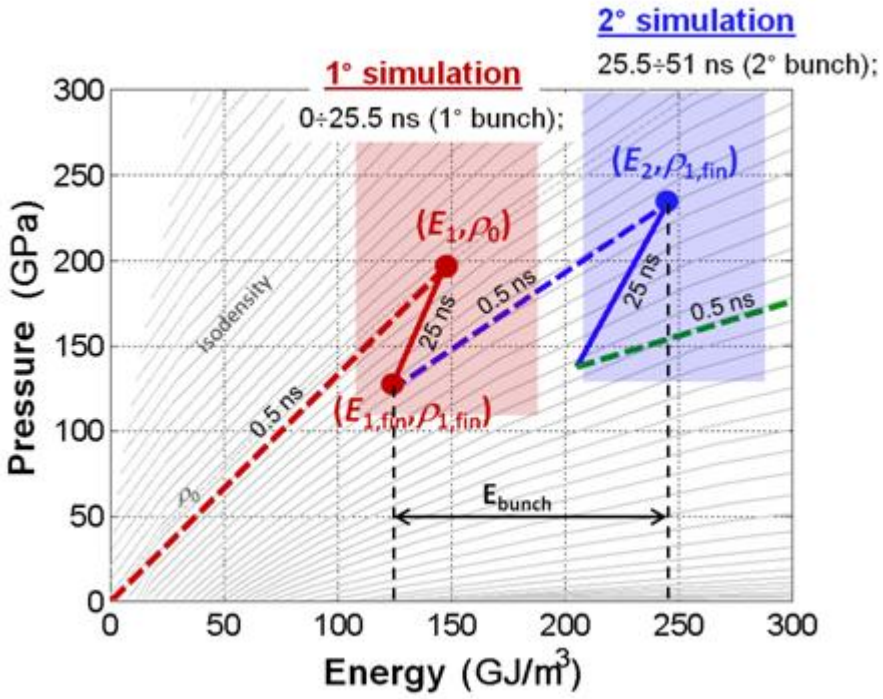

Fig. 5.7: Scheme of the procedure applied for the identification of the polynomial coefficients.

In Fig. 5.7, the case of the element, in which the maximum level of energy is deposited, is reported. The first simulation starts from the condition ρ_0 and $P_0 = 0$, and the final state after the deposition is defined by the point (E_1, ρ_0), where E_1 is the energy obtained from the FLUKA map for that element. At this point a reasonable interval in density and energy (red rectangle) is considered and the interpolation is performed. The same is then applied for the second simulation and so on. Between the two interpolations, there is the expansion time, in which the bunch is finished and the hydrodynamic response of the material can start (see solid line). This phase needs to be simulated in a FE code. At the end of the first simulation, the element reaches the condition identified as (E_{1fin}, ρ_{1fin}), from which the second simulation starts.

The EOS used for the interpolation is linear in density both for the cold curve and the thermal influence:

$$P = C_0 + C_1\mu + (C_4 + C_5\mu)E \tag{5.1}$$

Several methods for the coefficient identification have been analyzed (see e.g. 24, 25), but in this chapter only one is reported. Once the ranges in density and energy are fixed, each isochoric curve is interpolated with a linear function, in accordance to the fact that the Eq. 5.1 expresses the pressure as a linear function of the internal energy for a fixed density. The second step implies that all the intercept obtained (one for each density in the range), is interpolated with a linear function in order to obtain the coefficients C_0 and C_1. The same procedure is then applied also for the slopes, in order to get the coefficients C_4 and C_5.

5.3.2 Material strength

Since the energy distribution (and consequently also the pressure distribution) is not uniform on the hit component, the pressure gradients induce plasticity: the definition and the choice of the material strength model is of fundamental importance.

The part of the component external to the impacted zone and that, after the end of the deposition phase, is still solid is subjected to plasticity. In order to provide a complete and comprehensive description of the problem, the material model should take into account all the mechanical variables of interest for the stress flow evolution.

In the case study considered, the material results to be heavily deformed in a very short

time and in a very high temperature condition. In addition, the phenomenon has a strong thermo-structural coupling: the rise in temperature modifies the mechanical material response. As a matter of fact, the material properties may depend strongly upon the local temperature and for these problems it becomes necessary to compute the temperature throughout the material. Usually, due to the rise in temperature, there is a modification in the effect of the strain-rate on the flow stress, jointed with thermal softening effects (mechanical strength reduction). Besides, the process is characterized by the generation of a shock front that, travelling through the hit component, invests the solid part and implies a mass transport process with a significant density modification. Finally, given the high levels of pressure, also the pressure could influence the mechanical material response.

From these considerations it follows that the constitutive relation for the deviatoric behaviour of the material should consider as variables: the strain (both effective plastic and volumetric strains), the strain-rate, the temperature and the pressure. In addition, it could be important to take into account the modification of the mechanical properties due to material irradiation. As a matter of fact, during the development of particles cascades in the irradiated material, defects, such as vacancies and interstitials, are produced. The consequence is the accumulation of radiation defects forming clusters of point defects, such as dislocation loops and vacancy voids, which lead to a significant degradation of physical mechanical material properties.

The cases of high energy deposition in the materials, analyzed in details in the chapters 6 and 7 have the aim is to provide a preliminary description of the phenomenon evolution. In this perspective a simplified approach will be followed, taking into account only the effects of plastic strain, strain-rate and temperature on the flow stress, using the J-C model (see chapter 6), and also the pressure and density influence, using the S-G model (see chapter 6 and 7). On the other hand, the estimation of the reduction in the mechanical properties resulting from the material irradiation is neglected.

In addition also failure models will be defined used, in order to model the damage in the solid state. Besides, it will be necessary to introduce a spall model in order to correctly simulate the failure under hydrostatic tensile stresses. This condition can be reached in the material placed behind the shock front as consequent of the propagation of cylindrical pressure waves or when the impact occur near a free surface. Finally, it will be necessary to avoid that the elements that reach low value of density (density for which the material is not still solid) could be subjected to negative pressure and too large deformation of the

Lagrangian mesh. In this sense, an element erosion criterion will be defined with the condition that if at the same time both the pressure and the volume strain (that is correlated to the density) become lower than the corresponding imposed limits, then that element is deleted.

References

[1] Wiedemann H., "Particle Accelerator Physics I", Springer, Berlin (1993).

[2] Petterson T.S., Lefèvre P., "The Large Hadron Collider: conceptual design. CERN Desktop Publishing Service, Geneve (1995).

[3] "LHC Design Report, Vol. I, The LHC Main Ring", CERN Editorial Board (2004)

[4] "LHC Design Report, Vol. III, The LHC Injector Chain", CERN Editorial Board (2004)

[5] Dallocchio A., "Study of thermo-mechanical effects induced in solids by high energy particle beam: analytical and numerical methods", PhD Thesis, Politecnico di Torino (2008).

[6] Bennett J.R.J., Booth C.N., Brownsword R.A. et al., "LS-DYNA calculation of shock in solid", Nucl. Phys. B (Proc. Suppl.) 155:293-294 (2006).

[7] Bennett J.R.J., Skoro G.P., Booth C. et al., "Thermal shock measurements and modeling for solid high-power targets at high temperatures", Nucl. Mater. 377:285-289 (2008).

[8] Tahir N.A., et al., "Impact of 7-TeV/c large hadron collider proton beam on a copper target", Journal of Applied Physics, 97 (2005).

[9] Tahir N.A., et al., "Simulation studies of impact of SPS beam with collimator materials", Proceedings of EPAC08 (2008).

[10] Tahir N.A., et al., "Simulation of full impact of the Large Hadron Collider beam with a solid graphite target", Laser and Particle beams, 27: 475-483 (2009).

[11] Tahir N.A., et al., "Large Hadron Collider at CERN: Beams generating high-energy-density matter", Physical Review E, 79 (2009).

[12] Ryazanov A.I. et al., "Shock wave propagation near 7 TeV proton beam in LHC collimator materials", Proceeding of the Workshop on High Intensity High Brightness Hadron Beams 2006 (HB2006), Tsukuba, Japan, 29 May - 2 June 2006 (2006).

[13] Gladman B. et al., "LS-DYNA® Keyword User's Manual – Volume I – Version

971", LSTC (2007).

[14] Le Blanc G., Petit J., Chanal P. et al., "Modelling the dynamic magneto-thermomechanical behavior of materials using a multi-phase EOS", 7th European LS-DYNA Conference (2008).

[15] Royce E.B., "GRAY, A THREE-PHASE EQUATION OF STATE FOR METALS", Technical Report UCRL-51121, California Univ., Livermore. Lawrence Livermore Lab. (1971).

[16] Battistoni G., Muraro S., Sala P.R., Cerutti F., Ferrari A., Roesler S., Fasso` A. and Ranft J., "The FLUKA code: Description and benchmarking", Proceedings of the Hadronic Shower Simulation Workshop (2006), Fermilab 6--8 September 2006, M. Albrow, R. Raja eds., AIP Conference Proceeding 896, 31-49, (2007).

[17] Fasso A., Ferrari A., Ranft J. and Sala P.R., "FLUKA: A Multi-Particle Transport Code", CERN-2005-10, INFN/TC_05/11, SLAC-R-773 (2005).

[18] Schimdt R., Assmann R.W., Bertarelli A., Ferrari A. and Weterings W., "Summary of the CERN Workshop on Materials for Collimators and Beam Absorbers", LHC Project Report 1164, (2007).

[19] Simos N. et al., "Irradiation damage studies of high power accelerator materials", Nucl. Mater. 377:41-51, (2008).

[20] Yoshimura K., "R&D works on high-power targetry for neutrino factories", Nucl. Mater. 343:14-20, (2005).

[21] Bertarelli A. et al., "Research and Development of Novel Advanced Materials for Next-generation Collimators", IPAC'11, San Sebastián (2011).

[22] Redaelli, S. et al., "Operational performance of the LHC collimation", Proceedings of HB2010 (2010).

[23] Holian K.S., "T-4 Handbook of Material Properties Data Bases, Vol. Equations of State" LA-10160-MS Los Alamos National Laboratory (1984).

[24] Scapin M., Peroni L., Dallocchio A., "Damage evaluation in metal structures subjected to high energy deposition due to particle beams", 9th International Conference on Damage Assessment of Structures (DAMAS2011), Oxford (UK), (2011).

[25] Scapin M., Peroni L., Dallocchio A. "Thermo-mechanical modelling of high energy particle beam impacts", ACE-X 2010, Paris (F), (2010).

6. 2D-axisymmetric modelling

In this chapter, the numerical simulation of the high energy deposition on cylindrical bars, hit perpendicular at the centre of one face by 8 protons bunches of the LHC at 7 TeV is performed. Two cases are analyzed, varying the material of the target (copper and tungsten). For each case a Lagrangian 2D axisymmetric simulation is performed, starting from the energy deposition map. The results are shown in terms of both hydrodynamic and deviatoric quantities. Some results are reported also for the validation of the polynomial interpolation performed. At the end of the chapter, some considerations on the density influence on the energy absorption are made, comparing different target materials.

The numerical simulations of cylindrical targets, made in copper and tungsten, impacted perpendicular at the centre of one face are performed in LS-DYNA [1]. The case analyzed involved 8 proton bunches at 7 TeV (σ = 0.88 mm) of the LHC, which impact directly the target: the total duration of the deposition phase is about 200 ns. This duration corresponds to the time before the protection system starts dump the beam. The numerical simulation reaches 1 μs, in order to simulate also the expansion phase in free conditions (without any bunch impact). The geometry considered is a cylinder 1 m long and with a radius of 10 mm.

The fact that both the target geometry and the load applied, in terms of energy deposition, are axisymmetric allows treating the problem as axisymmetric, reducing the 3D problem to a 2D one, as e.g. performed in [2].

The FE solution is obtained in case of Lagrangian and pure structural analysis, solved with an explicit time integration method. The time step size is set about 0.1 ns in order to correctly appreciate the bunch profile (0.5 ns). The FE analyses are performed using 2D elements with 50 elements in the axial direction (element/bin size of 20 cm) and 100

elements in the radial direction (element/bin size of 0.1 mm). The study of the mesh influence is performed in [3] and showed that these values are a good compromise between solution accuracy and computational costs. The shell elements used are under-integrated (1 integration point). Also the FLUKA calculation is obtained on a 2D axisymmetric model of the pristine material (solid density) for the first bunch and then used without modification also for the next bunches, to simulate a multi-bunch impact.

6.1 Copper

The first case presented regards the numerical simulation of the impact against a bar made in copper. In Fig. 6.1 and 6.2 the FLUKA results on the copper bar for a single-bunch case are reported. The original FLUKA results, obtained in GeV/cm^3/proton, are converted to J/m^3 for the structural calculation.

In Fig. 6.1 there is the spatial energy distribution map (in logarithmic scale) on the target. In Fig. 6.2, the energy vs. radius curves varying the axial coordinate and the energy vs. axial direction curves varying the radial coordinate are shown. The peak of the energy deposition is about 36 GJ/m^3 and occurs along the axis of symmetry (r = 0 mm) at an axial coordinates of 16 cm.

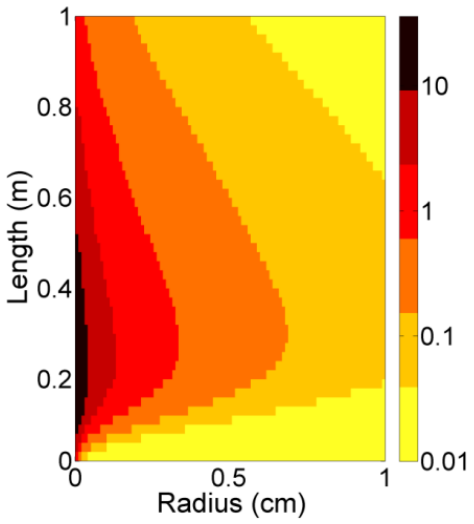

Fig. 6.1: Spatial distribution of the deposited specific energy (GJ/m^3) for a single bunch on copper cylindrical component.

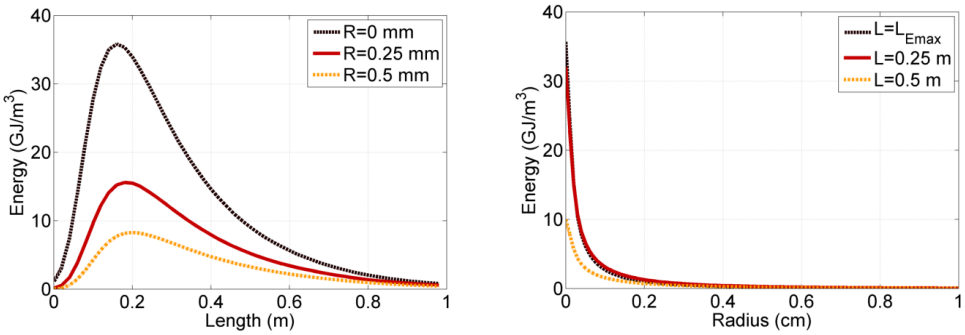

Fig. 6.2 Distribution of the deposited specific energy for a single bunch on copper cylindrical component: energy vs. axial direction curves varying the radial coordinate (left) and energy vs. radius curves varying the axial coordinates (right).

The strength model used for the description of the material behaviour is the J-C [5]. The failure J-C model [5] is also defined to model the damage in the solid state and a spall model to simulate the failure under hydrostatic tensile load. All these parameters are listed in Table 6.1.

Table 6.1: J-C parameters, copper [4, 5].

Parameter	Value	Unit	Parameter	Value	Unit
ρ_0	8937.5	kg/m^3	T_{melt}	1356	K
G	4.6×10^{10}	Pa	T_{room}	300	K
ν	0.3406	-	c_p	383	J/(kg K)
A	9.00×10^7	Pa	P_{spall}	-1.2×10^9	Pa
B	2.92×10^8	Pa	D_1	0.54	-
n	0.31	-	D_2	4.89	-
C	0.025	-	D_3	-3.03	-
$\dot{\varepsilon}_0$	1.00	s^{-1}	D_4	0.014	-
m	1.09	-	D_5	1.15	-

The EOS used as starting point for the polynomial interpolation is the table 3320 of the SESAME [6]. An erosion (deletion) criterion is added in order to preclude the possibility that elements with too low density are subjected to negative pressure (physically impossible condition). This means to avoid too high distortion of the numerical mesh. At each time step and for each element, the FEM solver performs the check of the erosion criterion condition: if at the same time both the pressure and the

density become lower than the corresponding imposed limits, then this element is deleted from the calculation. More precisely, the limit in terms of pressure is set equal to zero and the threshold in density is set equal to 8000 kg/m^3.

The numerical results on the component are shown in terms of pressure, density, temperature, Von Mises stress, plastic strain and particle velocity.

The entire deposition phase is about 200 ns. The numerical simulations are performed until 1 μs in order to have the possibility to evaluate the phenomenon evolution after the end of the impact phase. In Figures 6.3-6.8 the white area along the length axis represents the part of the component deleted from the calculation in accordance with the erosion criteria.

Figs. 6.3 and 6.4 report, respectively, the pressure and density evolutions at four different time steps: during the deposition phase (101.5 ns), at the end of the deposition phase (203.5 ns) and during the free phase (500 ns and 1000 ns).

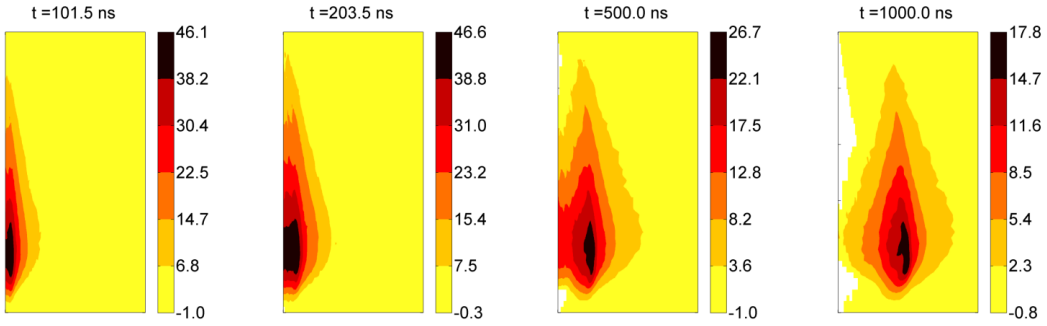

Fig. 6.3 Pressure distribution (GPa) on the copper cylindrical component at four different time steps: radius 0÷10 mm (→), length 0÷1 m (↑), the radial dimension is amplified.

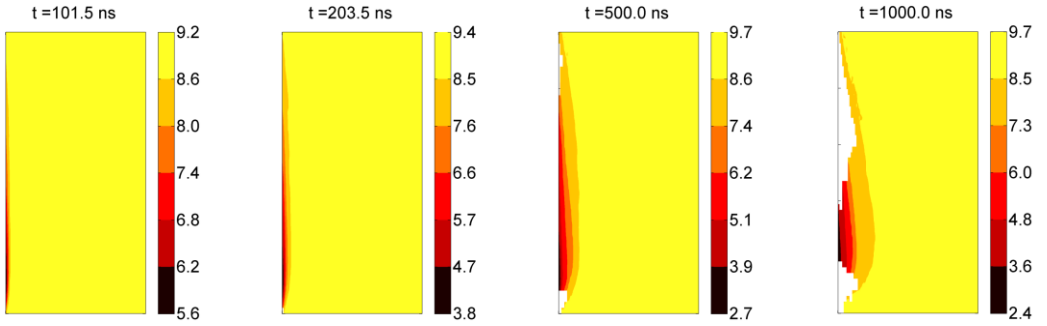

Fig. 6.4 Density distribution (kg/dm^3) on the copper cylindrical component at four different time steps: radius 0÷10 mm (→), length 0÷1 m (↑), the radial dimension is amplified.

The results show that the energy delivered on the hit (central) part of the component acts as an explosive. During the deposition phase the pressure grows up and reaches a maximum value close to 50 GPa in the central part. Once no more bunches are delivered, the shockwave, generated in the impact zone starts to travel from the hit zone to the external surface. The density evolution is strictly related to the pressure evolution in accordance with the EOS. The travelling shock-wave produces a rarefaction in the material placed behind and a compression in the material placed ahead of it. The central part of the target corresponds to the zone in which there is the material rarefaction. This part of material could be subjected to sudden and continuous changes of phase. The remaining part of the target behaves similar to the solid state resulting compressed by the transition of the shock front and then expanded by the travelling of the shock wave. This is in agreement with the results obtained in chapter 2 for the propagation of cylindrical shock-waves.

In Fig. 6.5 the pressure versus time history curve is depicted for elements situated in different positions on the hit component: along the axis of symmetry at three different longitudinal coordinates (P1: r=0 mm and L=5 cm; P2: r=0 mm and L=16 cm; P3: r=0 mm and L=50 cm) and at two distances from the axis of symmetry for two axial coordinates (P4: r=2.5 mm and L=20 cm; P5: r=5 mm and L=20 cm; P6: r=2.5 mm and L=50 cm; P7: r=5 mm and L=50 cm). The diagrams show that there is the growth in pressure followed by a sudden release in the part in which the highest values arise (P1-P3). In this portion, in the deposition phase, the pressure follows the typical sawtooth trend. Each peak of pressure is followed by a strong rarefaction process, which prevents a much larger pressure increase. In the part of the target, (P4-P7), that is quite far from the hit zone, during the deposition phase, the material remains quite undisturbed. On the other hand, this portion is affected by a further increase in pressure (that could become greater respect to the one reached during the deposition phase) due to the crossing in the component of the shock front.

In Fig. 6.6 the pressure versus radius curves at four different time steps (101.5 ns, 203.5 ns, 500 ns and 1000 ns) are depicted, in correspondence to two longitudinal coordinates (16 cm and 50 cm). The initial (t = 0) pressure evolutions follows the energy evolutions showed in Fig. 6.1. Observing the Fig. 6.6, it is possible to identify, at each time, the radial position of the shock front, that moves radially along the component reducing its intensity and investing the different part of the component at different times.

The shock front is identified by the spatial pressure discontinuity, which travels at a supersonic speed: after 1 μs, the shock front covers about 5 mm of the target.

The trend of the pressure, reported in the diagrams of Fig. 6.5 and 6.6, is in accordance with the results obtained in the chapter 2 for the travelling of cylindrical shock-waves. For elements P1, P2 and P3, it is not possible to appreciate the presence of negative pressure after the end of the shock, due to the presence of the erosion criteria. In any case these elements are situated in a part of the target, which is become gas or vapour (at low density and pressure) and is not subjected to negative pressure. For the elements P4 and P6 (situated in the solid part of the component), it is possible to notice that, after the maximum of pressure is reached (which correspond to the transition of the shock front), the unloading phase starts, but the simulation performed until 1 μs, is not long enough to reach the negative pressure state which follows the unloading one.

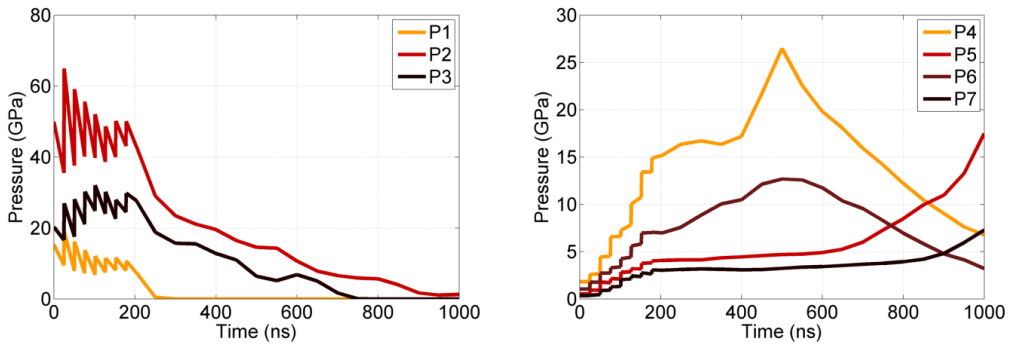

Fig. 6.5 Pressure vs. time history: (left) for three elements situated along the symmetry axis (P1: r=0 mm and L=5 cm; P2: r=0 mm and L=16 cm; P3: r=0 mm and L=50 cm) and (right) for four elements situated respectively at P4: r=2.5 mm and L=20 cm; P5: r=5 mm and L=20 cm; P6: r=2.5 mm and L=50 cm; P7: r=5 mm and L=50 cm.

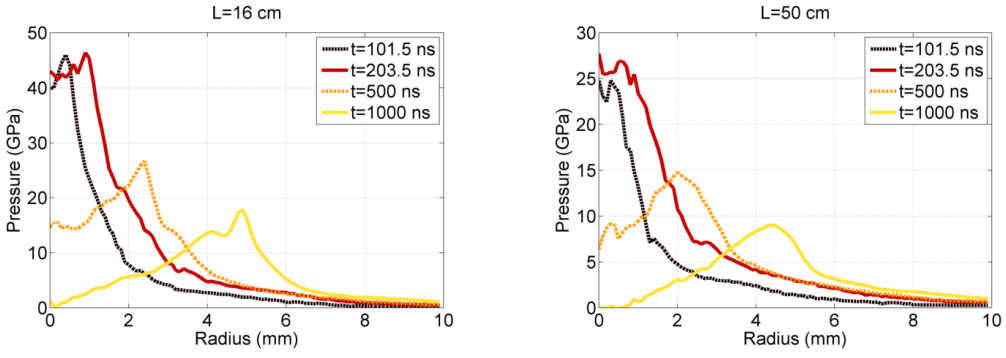

Fig. 6.6 Pressure vs. radius curves at four different time steps corresponding to two different longitudinal coordinates (16 cm on the left and 50 cm on the right).

Fig. 6.7 shows the spatial distributions of temperature, Von Mises stress, plastic strain and particle velocity at the end of the deposition.

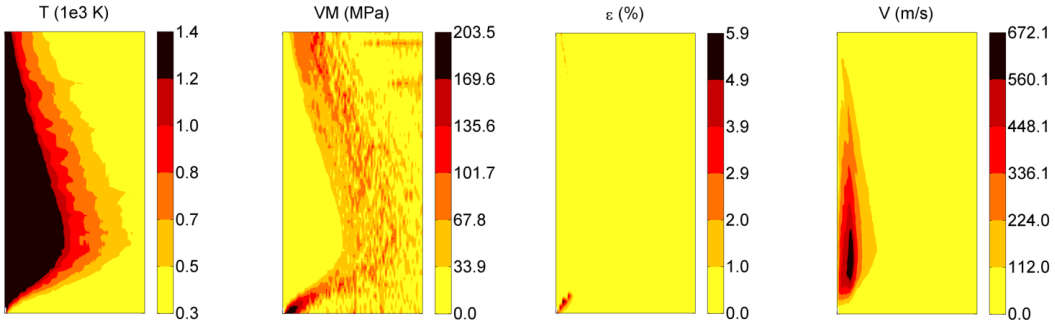

Fig. 6.7 Temperature, Von Mises stress, plastic strain and particle velocity distributions on the copper cylindrical component at the end of the deposition phase: radius 0÷10 mm (→), length 0÷1 m (↑), the radial dimension is amplified.

The temperature is limited to the melting value (1356 K). In case of pure structural analysis, the temperature evaluation is performed in, LS-DYNA, by the material strength model routine, which transforms the internal energy in temperature, using as proportional factors the density and the specific heat capacity for solid at room temperature. This implies the temperature calculation does not take into account the modification of the specific heat capacity with the phase changes of the matter. So, the temperature evaluation is correct only in the solid part. At the end of the deposition about 4 mm of the target are not still solid. The Von Mises stress is zero in the part of material that overcomes the melting value. This means in the central part of the component, since the mechanical resistance of the material is defeated, the material behaviour could be completely treated from a pure hydrodynamic point of view. On the other hand, for the material that remains solid, the maximum value of Von Mises stress is reached just across the shock front, where there is a sharp and significant discontinuity in pressure and density. At the end of the deposition the plastically deformed part of the component is still limited and the shock front is in the molten area.

In Fig. 6.8 there are the spatial distributions of the same quantities after 1 μs from the impact. The temperature is again limited to the melting value (1356 K). Comparing the molten area with that obtained at the end of the deposition, it is possible to conclude that the molten area stops to increase since there is no longer any external energy intake in the system. The maximum of the Von Mises stress follows the shock front and reaches high values (about two times the yield strength of the material). A significant part of the

component results to be heavy plastically deformed. During the free phase, the shock front propagates into the solid part of the target, increasing the particle velocity.

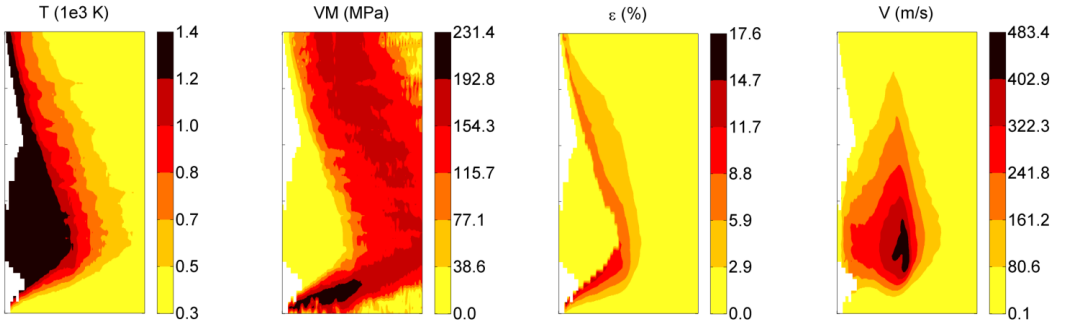

Fig. 6.8: Temperature, Von Mises stress, plastic strain and particle velocity distributions on the copper cylindrical component after 1 μs from the impact: radius 0÷10 mm (→), length 0÷1 m (↑), the radial dimension is amplified.

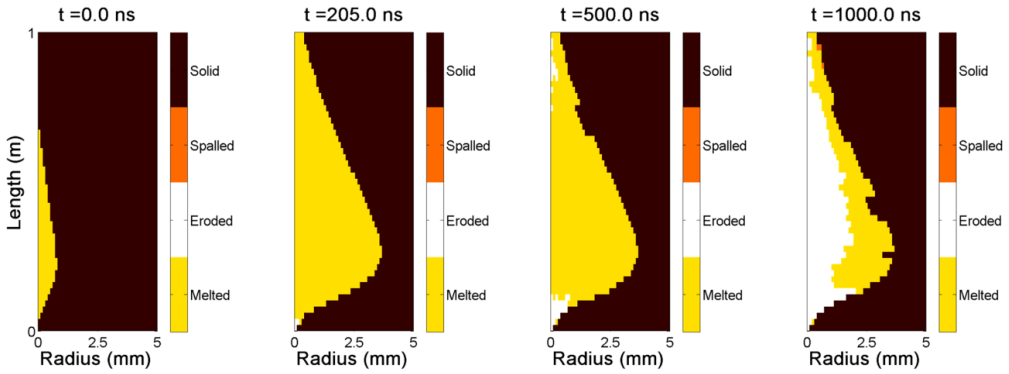

Fig. 6.9: Time evolution of the four type of damage evaluated: fusion, erosion, spallation and cumulative damage on the copper cylindrical component at four different time steps: radius 0÷5 mm (→), length 0÷1 m (↑), the radial dimension is amplified.

In order to evaluate the damage in the component it is necessary taking into account different methods of damage, corresponding to: exceeding the melting energy, reaching the state of matter corresponding to gas and vapour state, which is modelled with an element erosion criterion, spalling of the material and accumulation of the damage in the part of the target that remains solid. In Fig. 6.9, there is the time evolution of the different types of damage for a maximum radius of 5 mm.

For what concerns the melting energy, it is important to underline that for simplicity the evaluation of the fluid zone is done under the hypothesis that the melting temperature is constant with the density. The energy intensity deposited on the central part of the

component is such that the temperature overcomes the melting temperature: the shear strength is set to 0 and the material starts to behave like a fluid. In more detail, the results show that after a 1 μs from the impact the central part of the cylindrical target is molten over the 1 m of length, while in the radial direction the molten area is about 4 mm.

In the central part, the expansion leads to a significant reduction in density and pressure such that the erosion criteria are satisfied and the elements are deleted for all the longitudinal direction on the symmetry axis and until a radius of about 2 mm at the longitudinal coordinate correspondent to the maximum deposition values.

The part of the component behind the impacted area could be subjected to considerable values of tensile hydrostatic stresses, in accordance to what obtained in chapter 2 for the propagation of the cylindrical pressure shock-waves. As mentioned before, due to the imposed criteria, the elements, in which the pressure should become negative, are deleted from the calculation. The part of the target, which does not satisfy the deletion criteria, is not subjected to high negative pressure, therefore it does not exceed the spall limit. Moreover, in the solid part, there are not any boundary reflections, so the compressive wave does not become a tensile one.

In the solid part of the material, it is possible to calculate also the evolution of the cumulative ductile damage. Looking at the results, it is possible to notice that no element fails, since the damage parameter is less than unity during all the simulation.

In conclusion, until 1 μs after the impact, the principal damage source is represented by the material change of state (vaporizing and melting), while spallation and ductile damage do not occur. The reason is that the part of the component taken into account for this analysis is prevalently subjected to compressive stress that does not produce any cumulative damage or significant spallation. The last phenomenon will probably happen as soon as the shock-wave will be reflected by a free surface or if the target is hit near a free surface, but the latter case cannot be simulated with a 2D axisymmetric model.

Observing the EOS in the pressure-energy plane varying the density (see Fig. 6.10), it is quite easy to follow the transformation in the material. The gray lines plotted as background are the isodensity curves of the tabular SESAME EOS. The red and black lines are the paths obtained from the numerical simulation depending on the goodness of the polynomial interpolation. Fig. 6.10 shows the evolution for the element in which there is the maximum of the deposited energy. During the bunch arrival (0.5 ns), there is a sudden increase in the internal energy with a negligible variation in the material density

(isochoric transformation): consequently, the pressure increases. After the bunch impact (during the 25 ns of void separating two successive bunches, or at the end of the deposition), the material could be expanded (reaching lower value of pressure and density, case depicted in Fig. 6.10), or compressed (reaching higher value of pressure and density) depending on the global redistribution of the stress on the component.

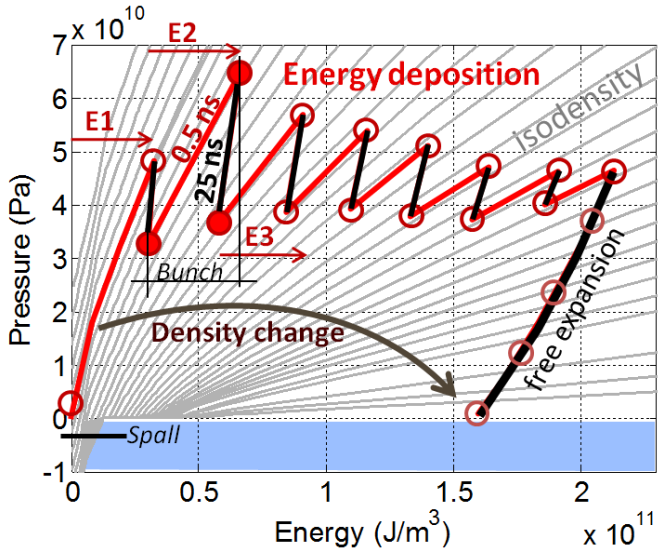

Fig. 6.10 Equation of state of copper: pressure vs. energy plane varying the density. The diagram represents the P-E-ρ evolution of the element in which there is the maximum of the energy deposition. The symbols represents the states P-ρ-E reached by the material. In particular, during the energy deposition phase, the symbols identify the material conditions after each bunch arrival and after 25 ns from its arrival. In the figure, E1 represents the energy deposited after the first bunch, E2 the total amount of energy after the arrival of the second bunch and so on.

6.2 Tungsten

The second case presented regards the numerical simulation of the impact against a bar made in tungsten. In Fig. 6.11 and 6.12, the FLUKA results on the tungsten bar for a single bunch are reported.

The original FLUKA results, obtained in GeV/cm^3/proton, are converted to J/m^3 for the structural calculation. In Fig. 6.12 there is the spatial energy distribution map (in logarithmic scale) on the target. In Fig. 6.13, the energy vs. radius curves varying the axial coordinate and the energy vs. axial direction curves varying the radial coordinate are shown. The peak of the energy deposition is about 150 GJ/m^3 and occurs along the axis of symmetry (r = 0 mm) at an axial coordinates of 6 cm.

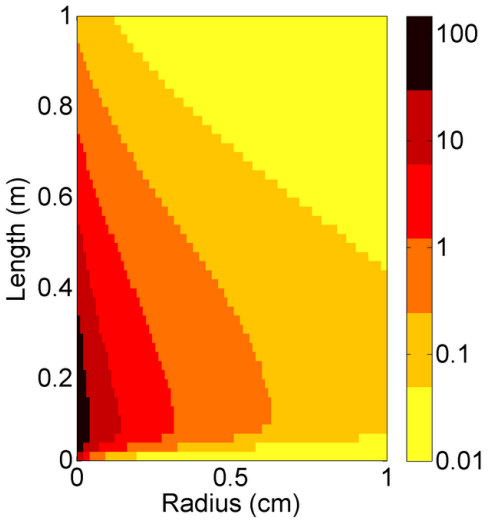

Fig. 6.11: Spatial distribution of the deposited specific energy (GJ/m^3) for a single bunch on tungsten cylindrical component.

Comparing the energy maps and the diagrams obtained for copper and tungsten, it is possible to notice a dependency between the density and the amount of energy absorbed by the material. The probability of the interaction between particles and matter is strongly density dependent and the material density plays a key role in the calculation of the proton energy loss in case of impact against a target. This subject is treated more in depth in the paragraph 6.4, where analytical calculations are made for estimating the pressure distribution in four different materials.

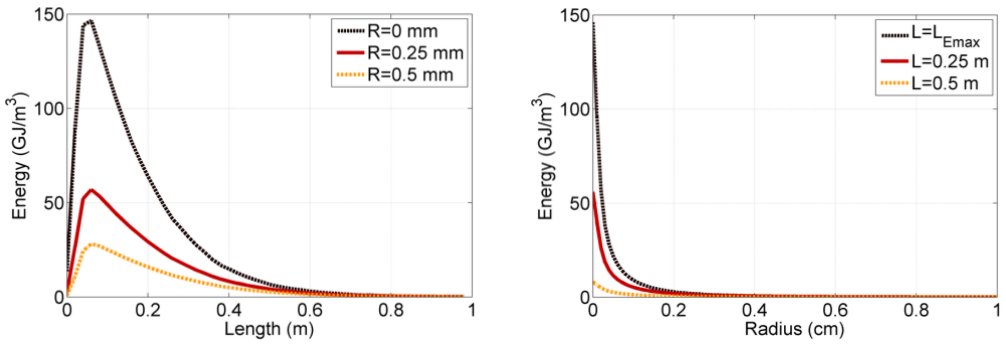

Fig. 6.12: Distribution of the deposited specific energy for a single bunch on tungsten cylindrical component: energy vs. axial direction curves varying the radial coordinate (left) and energy vs. radius curves varying the axial coordinates (right).

To simulate the energy deposition in tungsten, two material models are used for the description of the material strength: the J-C and the S-G. The failure model for the solid

state is not defined, in accordance with the results obtained for copper, which showed that after 1 μs no ductile damage in solid occurs, since this part is mainly subjected to compressive loads. The spall model is introduced for limiting the negative pressure, in the portion of material behind the shock front.

The parameters for the two material models are listed in Table 6.2 and 6.3. The erosion criterion defined for tungsten sets the threshold in pressure equal to zero and that in density equal to 14600 kg/m^3. The EOS used as starting point for the polynomial interpolation is the table 3550 of the SESAME [7].

Table 6.2: J-C parameters for tungsten [8].

Parameter	**Value**	**Unit**	**Parameter**	**Value**	**Unit**
ρ_0	19255	kg/m^3	$\dot{\varepsilon}_0$	1×10^{-3}	s^{-1}
G	1.6×10^{11}	Pa	m	0.41	-
ν	0.33	-	T_{melt}	3683	K
A	3.30×10^{8}	Pa	T_{room}	300	K
B	1.03×10^{9}	Pa	c_p	135.68	J/(kg K)
n	0.02	-	P_{spall}	-1.2×10^{9}	Pa
C	0.03	-			

Table 6.3: S-G parameters for tungsten [9].

Parameter	**Value**	**Unit**	**Parameter**	**Value**	**Unit**
ρ_0	19300	kg/m^3	h_1	0.938×10^{-11}	Pa^{-1}
G_0	1.6×10^{11}	Pa	$h2$	1.38×10^{-4}	K^{-1}
σ_0	2.20×10^{9}	Pa	T_{m0}	4520	K
β	24	-	a	1.3	-
n	0.19	-	γ_0	1.67	-
$\varepsilon_{pl,i}$	0	-	A	183.84	uma
σ_{MAX}	4.00×10^{9}	Pa	P_{spall}	-9×10^{8}	Pa

6.2.1 J-C model

In this paragraph, the results are reported for the J-C model in terms of pressure, density, temperature, Von Mises stress, plastic strain and particle velocity. It is important to note that the results in terms of pressure and density are independent from the strength material model used, since they depend only from the EOS. The main characteristics of generation and propagation of shock-waves are the same of those presented for copper. The differences are substantially due to the different amount of energy accumulated inside the material.

As for the case of copper, the entire deposition phase is about 203.5 ns and the numerical simulation is performed until 1 μs in order to have the possibility to evaluate the phenomenon evolution after the end of the impact phase. In Figs. 6.13-6.18, the white area along the length axis represents the part of the component deleted from the calculation, in accordance with the erosion criteria.

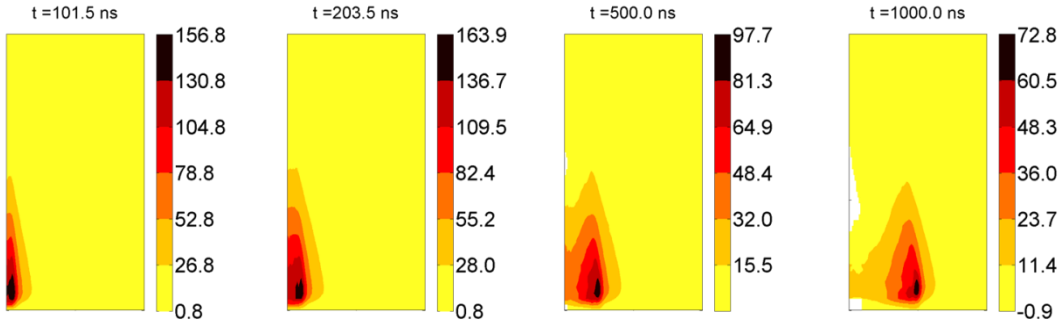

Fig. 6.13 Pressure distribution (GPa) on the tungsten cylindrical component at four different time steps: radius 0÷10 mm (→), length 0÷1 m (↑), the radial dimension is amplified.

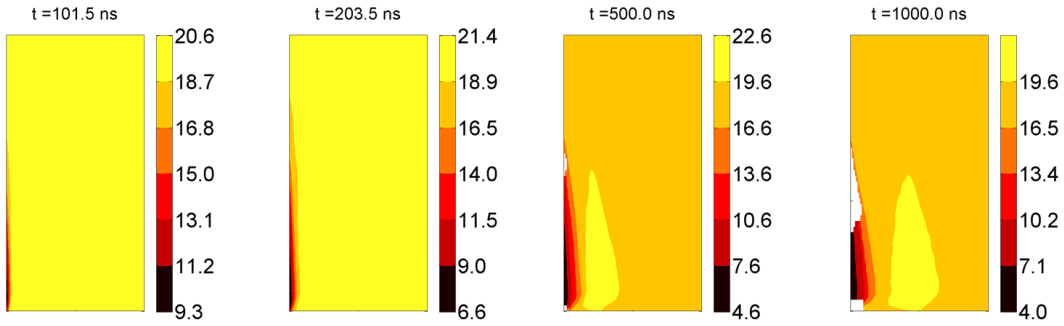

Fig. 6.14 Density distribution (kg/dm^3) on the tungsten cylindrical component at four different time steps: radius 0÷10 mm (→), length 0÷1 m (↑), the radial dimension is amplified.

Figs. 6.13 and 6.14 report, respectively, the pressure and density evolutions at four different time steps: during the deposition phase (101.5 ns), at the end of the deposition phase (203.5 ns) and during the free phase (500 ns and 1000 ns). The phenomenon evolution is similar to what happens for copper, but in this case, during the deposition phase, the pressure grows up and reaches higher value in the central part, since the pick of energy is about four times that of copper. Once no more bunches are delivered, the shock-wave, generated in the impacted zone starts to travel from the hit zone to the external radial surface, producing the rarefaction of the material placed behind the shock front.

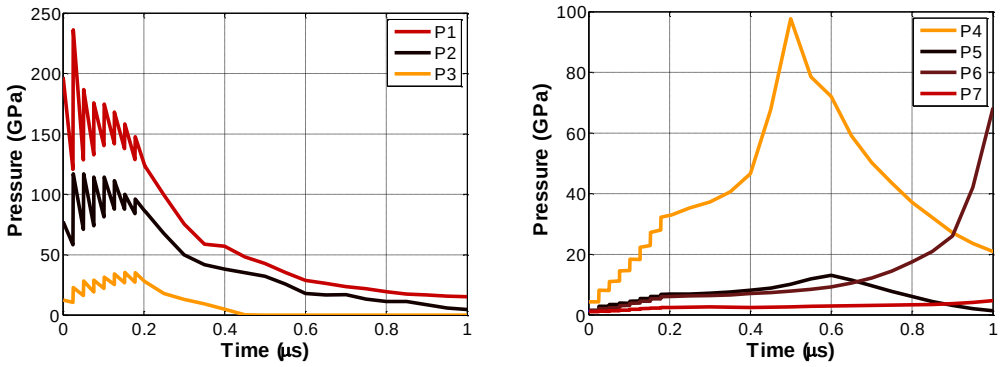

Fig. 6.15 Pressure vs. time history: (left) for three elements situated along the symmetry axis (P1: r=0 mm and L=6 cm; P2: r=0 mm and L=25 cm; P3: r=0 mm and L=50 cm) and (right) for four elements situated respectively at P4: r=2.5 mm and L=6 cm; P5: r=2.5 mm and L=50 cm; P6: r=5 mm and L=50 cm; P7: r=5 mm and L=6 cm.

In Fig. 6.15, the pressure versus time history curves is depicted for elements situated in different positions in the hit component: along the axis of symmetry at three different longitudinal coordinates (P1: r=0 mm and L=6 cm; P2: r=0 mm and L=25 cm; P3: r=0 mm and L=50 cm) and at two distances from the axis of symmetry for two axial coordinates (P4: r=2.5 mm and L=6 cm; P5: r=2.5 mm and L=50 cm; P6: r=5 mm and L=50 cm; P7: r=5 mm and L=6 cm).

In Fig. 6.16 the pressure versus radius curves at four different time steps (101.5 ns, 203.5 ns, 500 ns and 1000 ns) are depicted corresponding to two longitudinal coordinates (6 cm and 50 cm). The position of shock front can be identified by the spatial pressure discontinuity which travels at a supersonic speed: after 1 μs, the shock front covers about 5 mm of the target.

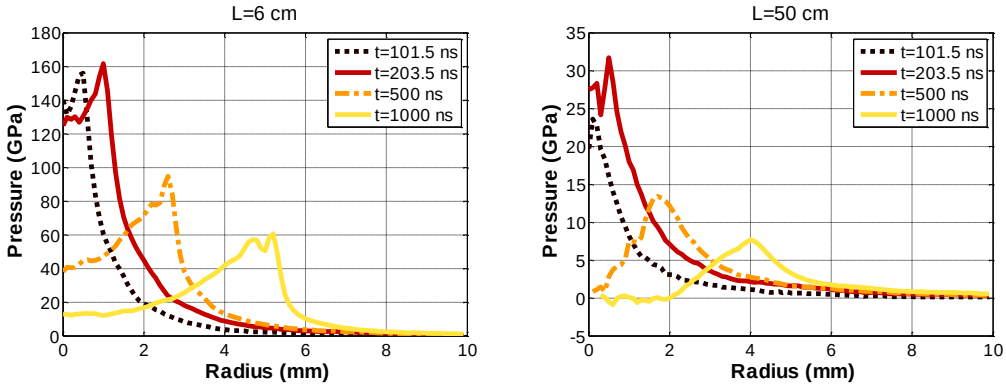

Fig. 6.16 Pressure vs. radius curves at four different time steps corresponding to two different longitudinal coordinates (6 cm on the left and 50 cm on the right).

In Fig. 6.17, there are the spatial distributions of temperature, Von Mises stress, plastic strain and particle velocity at the end of the deposition.

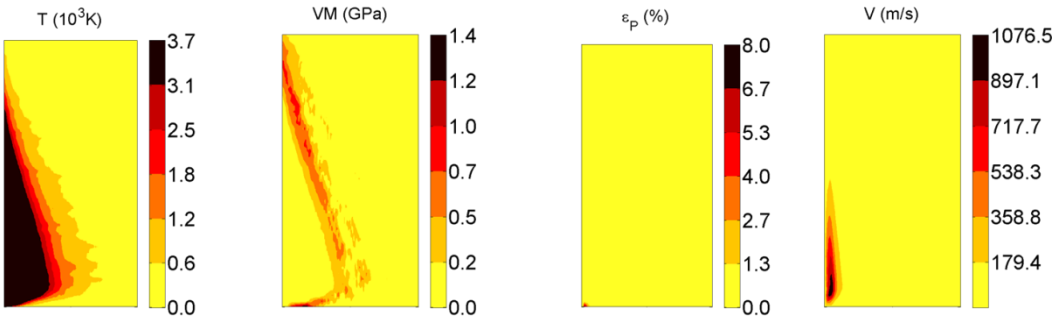

Fig. 6.17: Temperature, Von Mises stress, plastic strain and particle velocity distributions on the tungsten cylindrical component at the end of the deposition phase (J-C model): radius 0÷10 mm (→), length 0÷1 m (↑), the radial dimension is amplified.

The temperature is limited to the melting value (3683 K). At the end of the deposition about 3 mm of the component are not still solid. In Fig. 6.18, there are the spatial distributions of the same quantities after 1 μs from the impact. Also for the case of tungsten, the molten area stops to increase after the end of the deposition phase. The Von Mises stress is zero in the central part, which experiences a change of state, and is maximum just across the shock front: this implies that the solid part of the material is heavily plastically deformed. The shock front remains in the molten area until the end of the deposition, then starts to travel in the solid material, reaching a radial coordinate of about 5 mm after 1 μs.

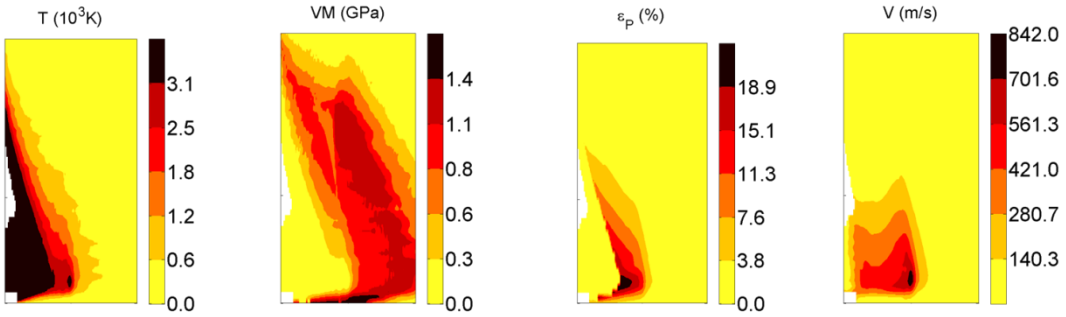

Fig. 6.18: Temperature, Von Mises stress, plastic strain and particle velocity distributions on the tungsten cylindrical component after 1 μs from the impact (J-C model): radius 0÷10 mm (→), length 0÷1 m (↑), the radial dimension is amplified.

For the case of tungsten, the *P* vs. *E* behaviour varying the density is reported for three elements, in Fig. 6.19.

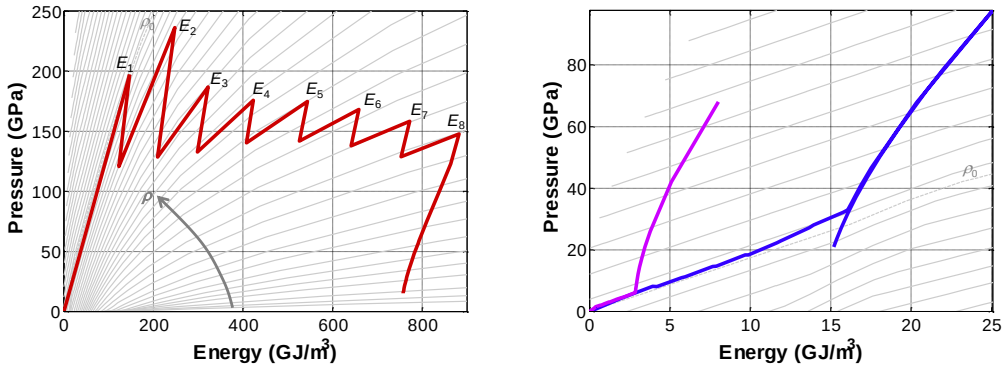

Fig. 6.19: Equation of state of tungsten: pressure vs. energy plane varying the density. The diagrams represent the P-E-ρ evolution of three elements: one situated where there is the maximum of the energy deposition (P1) and the other two far from this region (P4 blue and P5 magenta).

One element is situated on the longitudinal axis and is the element in which the maximum value of energy is deposited (P1). As it is possible to see, the behaviour of this element follows what happens for the equivalent element in case of copper. The other two elements are placed far from the impacted zone (P4 and P6). The deposition phase leaves these elements quite undisturbed. Since they absorb a low amount of energy, the consequent growth in pressure is limited and no significant changes in density occur. On the other hand, when the shock-wave reaches these elements, they are strongly compressed, reaching high values both in density and pressure. When the shock finishes, the unloading process starts.

6.2.2 S-G model

In this paragraph, the results are reported for the S-G model, in terms of deviatoric quantities. The results in terms of pressure and density are omitted, since the hydrodynamic response of material is not affected by the change of the strength material model.

The results are summarized in Figs. 6.20 and 6.21, in which the spatial distributions of temperature, Von Mises stress, plastic strain and particle velocity at the end of the deposition and after 1 μs are, respectively, reported. As for the case in which the J-C model parameters are used, also in this case the temperature is saturated at 3683 K, so the temperature distribution can be directly compared.

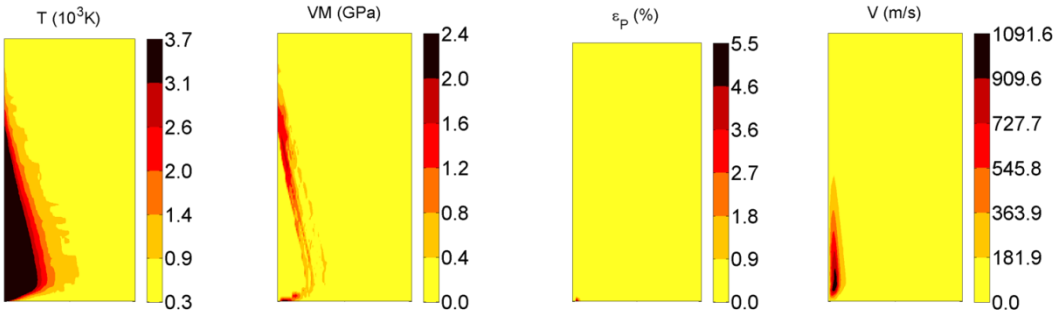

Fig. 6.20: Temperature, Von Mises stress, plastic strain and particle velocity distributions on the tungsten cylindrical component at the end of the deposition phase (S-G model): radius 0÷10 mm (→), length 0÷1 m (↑), the radial dimension is amplified.

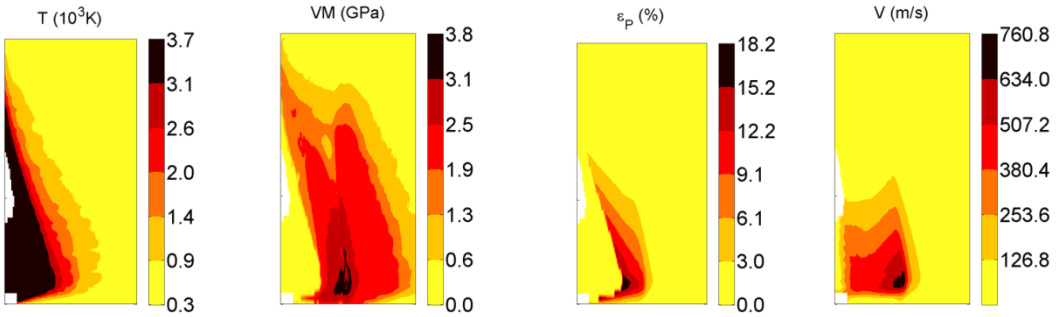

Fig. 6.21: Temperature, Von Mises stress, plastic strain and particle velocity distributions on the tungsten cylindrical component after 1 μs from the impact (S-G model): radius 0÷10 mm (→), length 0÷1 m (↑), the radial dimension is amplified.

6.3 Validity of the interpolation

In order to verify the efficacy of the polynomial interpolation of the tabular SESAME, two different checks are performed. In the first one, the pressure vs. time profiles obtained for copper and reported in Fig. 6.5, are compared to those obtained by the Engineering Group at CERN, with AUTODYN [10] for the same case (see Fig. 6.22). In AUTODYN, the SESAME table is implemented and can be directly used in the numerical simulation. Comparing the diagrams, it can be concluded that the EOS interpolated is able to reproduce, with a good level of approximation, the AUTODYN results. Some significant differences can be found during the free phase of expansion, since in this case the accuracy of the interpolation is lower: the fit is performed over a wide range in density and energy. Moreover, the erosion criteria introduced in LS-DYNA is not the same of that is defined in AUTODYN and this may causes differences also in the elements deletion.

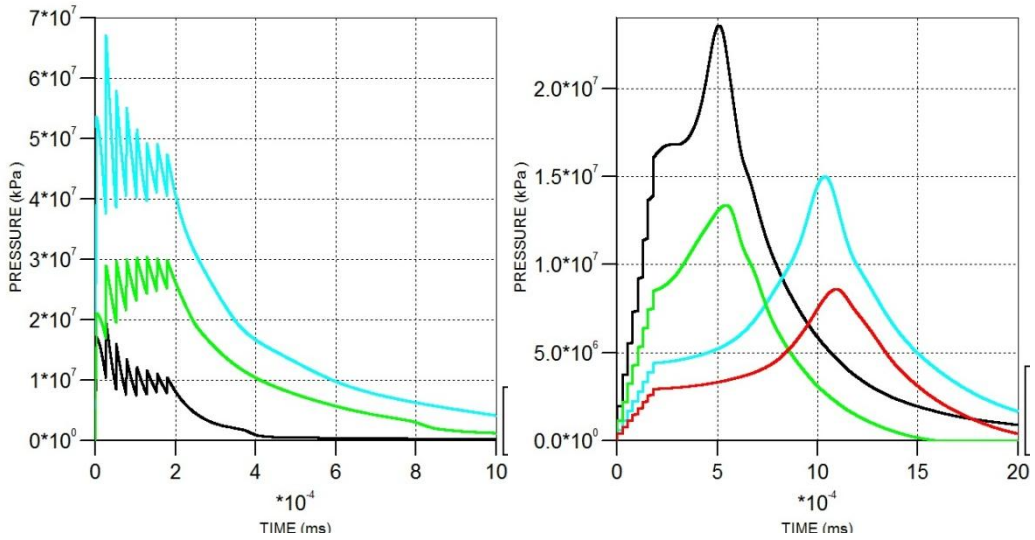

Fig. 6.22: *Pressure vs. time history obtained with AUTODYN: (left) for three elements situated along the symmetry axis (P1: r=0 mm and L=5 cm; P2: r=0 mm and L=16 cm; P3: r=0 mm and L=50 cm) and (right) for four elements situated respectively at P4: r=2.5 mm and L=20 cm; P5: r=5 mm and L=20 cm; P6: r=2.5 mm and L=50 cm; P7: r=5 mm and L=50 cm.*

In the second check, the comparison between the polynomial EOS and the original one is done on two elements, in the case of tungsten. The elements used for the analysis are P1, in which the maximum level of energy is deposited (r = 0 and L = 6 cm) and P7, situated at the coordinates r = 5 mm and L = 6 cm. In Figs. 6.23-6.26, the results are reported.

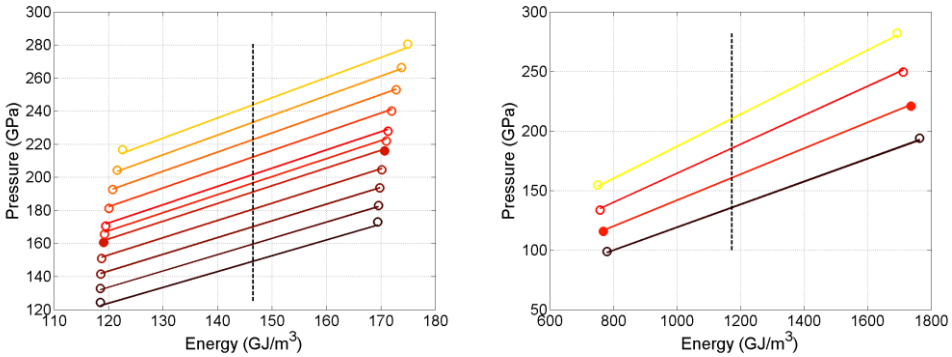

Fig. 6.23: Equation of state of tungsten: comparison in terms of pressure vs. energy plane varying the density between the original data and those obtained after the polynomial interpolation. The diagrams correspond to the element P1 (r=0 mm and L=6 cm) for the first (left) and the last (right) bunches.

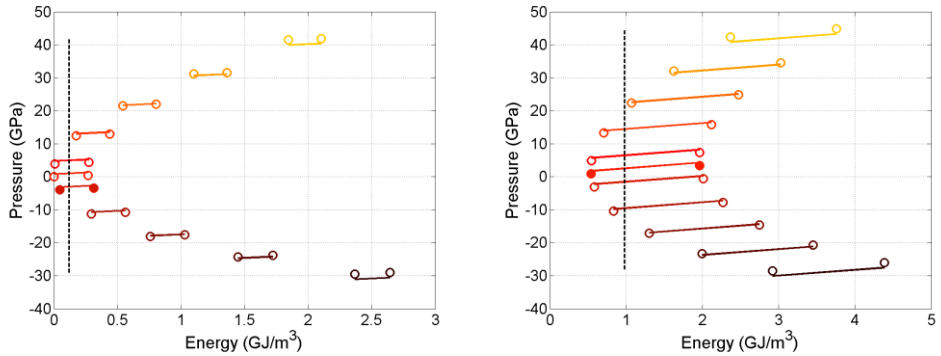

Fig. 6.24: Equation of state of tungsten: comparison in terms of pressure vs. energy plane varying the density between the original data and those obtained after the polynomial interpolation. The diagrams correspond to the element P7 (r=5 mm and L=6 cm) for the first (left) and the last (right) bunches.

In Fig. 6.23 and 6.24, the comparison is made on the pressure vs. energy plane, varying the density, for the interpolation related to the first bunch and the last one (solid lines).

For each density, the interpolation returns a line in energy. The markers represent the SESAME data taken into account for the interpolation. The filled markers identify the position of the actual density and the dashed vertical line represents the amount on energy deposited in the element. As it is possible to notice, the strategy for the identification of the range in which performing the interpolation is such that, at each interpolation (during the deposition phase), the total amount of energy and the actual density are in the middle of the considered ranges. Looking at the results, it can be concluded that, the polynomial interpolation gives good results. Obviously, the error increases during the calculation of the free expansion (after the end of the deposition phase), since the range in density and

energy considered is wider.

In Figs. 6.25 and 6.26, the cold and thermal pressure components obtained from the interpolation are compared with the SESAME data (markers). In more details, the values obtained for all the intercepts (one for each density) are linearly interpolated by the expression of the cold pressure. Similarly, all the values obtained for the slopes are linearly interpolated by the expression of the thermal pressure.

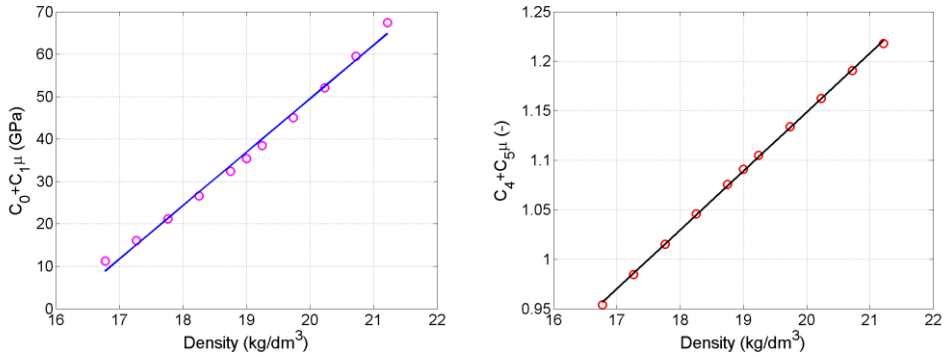

Fig. 6.25: Cold (left) and thermal (right) pressure components. The diagrams correspond to the element P1 (r=0 mm and L=6 cm) for the first bunch.

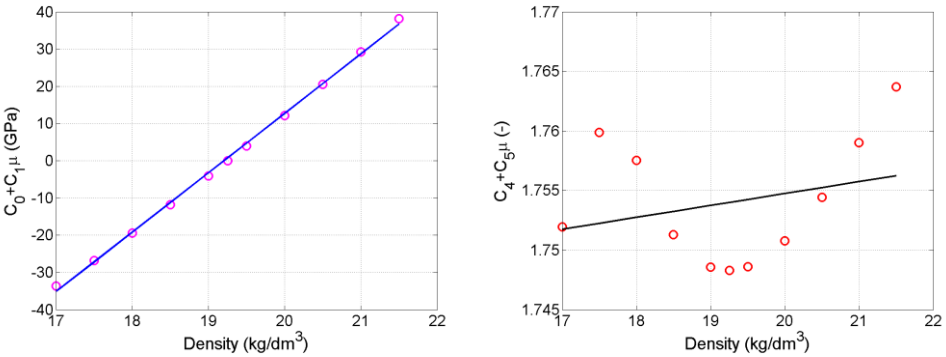

Fig. 6.26: Cold (left) and thermal (right) pressure components. The diagrams correspond to the element P7 (r=5 mm and L=6 cm) for the last bunch.

6.4 Density dependency

As mentioned in the previous paragraph, comparing the energy maps obtained for copper and tungsten, it is possible to notice a dependency between the density and the amount of energy absorbed, as well as on the penetration length.

The probability of the interaction between particles and materials is strongly density dependent and the material density plays a key role in the calculation of the proton energy loss in case of impact against a target. This implies that two materials subjected to the same impact condition, but with different density, experience different energy absorptions: the higher the density of the material, the higher its energy absorption. Indeed, the energy absorption is function of the type of the interacting high energy particles (protons, photons, electrons, hadrons, neutrinos, etc...) and different material properties, such as the atomic number, the ratio between atomic number and atomic mass, the lattice structure, etc... Besides, it means also that, for the same material, if there is a density evolution during the simulation, it should be taken into account in order to recalculate the energy deposition on the material in these new conditions. About the last point, up to now, a preliminary approach is followed: the energy deposition on the material is calculated on the initial condition (density of the solid state) and then used during the entire multi-bunch impact simulation without any modifications.

In order to better explain this concept, the results in terms of deposited energy and pressure are reported and compared for four materials: graphite, silicon carbide, copper and tungsten. In Table 6.3 some properties of the materials investigated are reported, as well as some results. In order to make the comparison, the FLUKA Team at CERN calculated the deposited energy map for the four materials on a cylindrical geometry of 10 mm of radius and 1 m long. The results are for one bunch of the LHC at 7 TeV with 1.15×10^{11} protons.

Table 6.4: Comparison between the energy absorption, in terms of energy, pressure and length of penetration of four materials with different densities.

Material	***Z* number**	**Density (kg/dm^3)**	**Maximum energy (GJ/m^3)**	**Maximum pressure (GPa)**	**L_{max} (mm)**
Graphite	6	2.28	0.46	0.16	> 1000
Silicon Carbide	-	3.21	3.09	2.94	600
Copper	29	8.94	37.45	52.34	160
Tungsten	74	19.26	153.27	202.64	60

Starting from the FLUKA map, for each material, the consequent rise in pressure can be evaluated, just searching the correct position on the SESAME EOS, under the hypothesis of isochoric transformation (normal solid density) during the deposition. The tabular EOS used are: table 7830 for graphite [11], table 6800 for silicon carbide [12], table 3320 for copper [6] and table 3550 for tungsten [7].

The maximum values of energy and pressure are reported in Table 6.4, where also the longitudinal position of the peak is indicated. As expected, the maximum value of energy corresponds to the material with the highest density, for which, otherwise, the maximum of the energy is situated at a lower longitudinal coordinate. In case of graphite, for example, the maximum of the interaction is developed for length greater than 1 m, so in the case reported, it is not reached.

In Figs. 6.27-6.30, the maps of the energy deposited by a single bunch and the consequent pressure are reported.

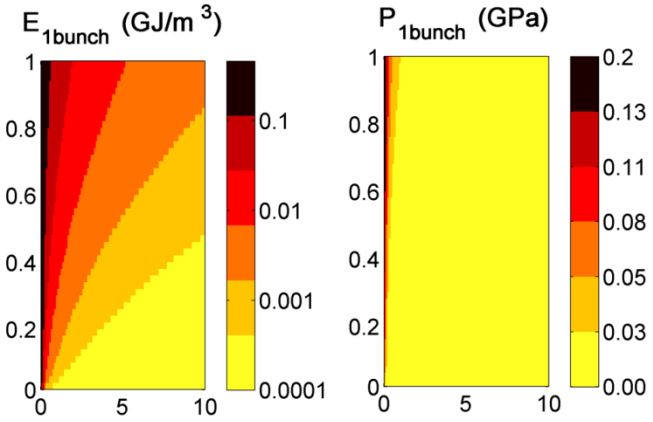

Fig. 6.27: Energy and pressure distribution for a single bunch deposition on a carbon cylinder; radius 0÷10 mm (→), length 0÷1 m (↑), the radial dimension is amplified.

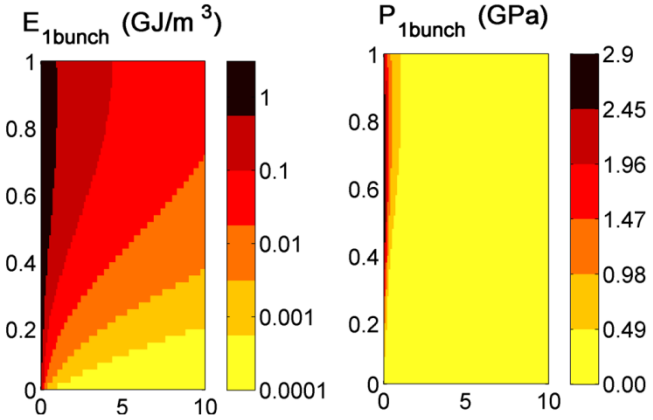

Fig. 6.28: Energy and pressure distribution for a single bunch deposition on a silicon carbide cylinder; radius 0÷10 mm (→), length 0÷1 m (↑), the radial dimension is amplified.

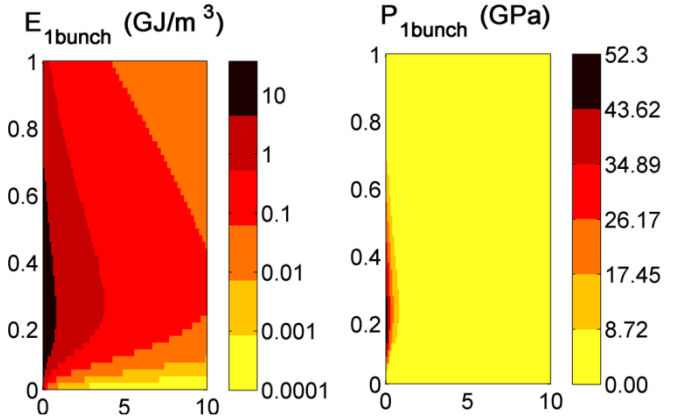

Fig. 6.29: Energy and pressure distribution for a single bunch deposition on a copper cylinder; radius 0÷10 mm (→), length 0÷1 m (↑), the radial dimension is amplified.

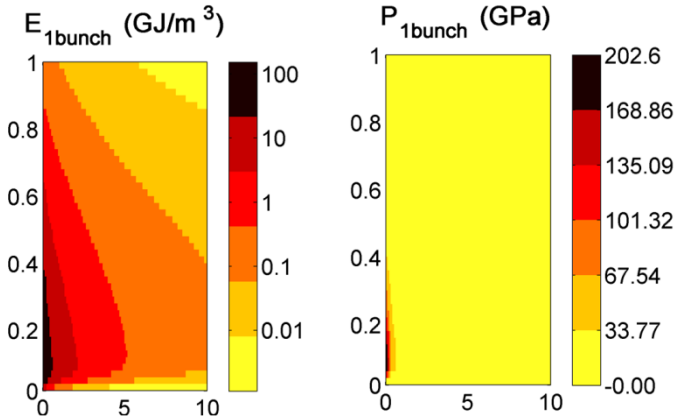

Fig. 6.30: Energy and pressure distribution for a single bunch deposition on a tungsten cylinder; radius 0÷10 mm (→), length 0÷1 m (↑), the radial dimension is amplified.

References

[1] Gladman B. et al., "LS-DYNA® Keyword User's Manual – Volume I – Version 971", LSTC (2007).

[2] Tahir N.A., et al., "Large Hadron Collider at CERN: Beams generating high-energy-density matter", Physical Review E, 79 (2009).

[3] Scapin M., Peroni L., Dallocchio A., "Thermo-mechanical modelling of high energy particle beam impacts", ACE-X 2010 (2010).

[4] Johnson, G. R. and Cook, W. A., "A constitutive model and data for metals subjected to large strains, high strain rates and high temperatures", 7th International Symposium on Ballistic, 541-547 (1983).

[5] Johnson, G. R. and Cook, W. A., Fracture characteristic of three metals subjected to various strains, strain rates, temperature and pressure. *Eng. Fract. Mech.* (1985) **2**

(1): 31-48.

[6] Kerley, G.I., "Equations of State for Copper and Lead", Kerley Technical Services report KTS02-1 (2002).

[7] Kerley, G.I., "Equations of State for Be, Ni, W, and AU", SANDIA REPORT SAND 2003-3784 (2003).

[8] Lennon A.M. and Ramesh K.T., "The thermoviscoplastic response of polycrystalline tungsten in compression", Material Science and Engineering A276:9-21 (2000).

[9] Steinberg, D.J., Equation of State and Strength Properties of Selected Materials, Lawrence Livermore National Laboratory, UCRL-MA-106439, (1996).

[10] "ANSYS AUTODYN User's Manual – Release 2010", ANSYS Inc. (2010).

[11] Kerley, G.I., "Multicomponent-Multiphase Equation of State for Carbon", SANDIA REPORT SAND 2001-2619 (2001).

[12] Kerley, G.I., "Equation of State and Constitutive Behavior of Silicon Carbide," Kerley Technical Services report KTS03-1 (2003).

7. 3D modelling

In this chapter, the impact of high energy proton beam against 3D structures is described. The FE solution is obtained in case of Lagrangian and pure structural analysis solved with an explicit time integration method, on 3D solid elements with a 1 integration point. Two different cases are reported. In the first one, the impact is simulated on the simplified model of a tertiary collimator, made in copper with the jaw in tungsten alloy (Inermet 180). The impact case is 8 LHC proton bunches at 5 TeV, impacting 2 mm inside the tungsten jaw and parallel to the external face. As for the 2D cases, the total duration of the deposition phase is about 200 ns. Then, the simulation of the expansion phase in free conditions is performed until 4 μs. The description of this case is of particular interest for the evaluation of the consequences of the impact near a free surface and the results are shown in terms of pressure and Von Mises stress. For the second case, the objective is the description of a numerical procedure, for a soft coupling between FLUKA and LS-DYNA codes, developed in collaboration with the FLUKA Team at CERN. The main objective is evaluating the influence of the change in density on the deposition phase. In order to achieve this, a great number of bunches (60) are supposed to impact against a tungsten parallelepiped. The results in terms of thermodynamic quantities are compared with the same case in which the coupling is not performed. Finally the study of the convergence of the results in function of the mesh dimension is evaluated, comparing three different cases.

7.1 TCT

The methodology described in the previous chapter is here applied to simulate the beam impact against a real complex geometry: the Target Collimator Tertiary (TCT) of LHC [1]. Collimators are particular devices that, placed close to the beam, intercept and stop particles of the external halo, see Fig. 7.1. Moreover, in case of accident scenarios, when the beam is out of control, collimators are strategically positioned, in order to absorb the particle impact, thus protecting other critical structures, such as the superconducting magnets. The LHC collimation system is made up of several collimators placed along the LHC ring. The study of the possible damage of the collimators is crucial issue, due to the fact that they are the closest components to the proton beam.

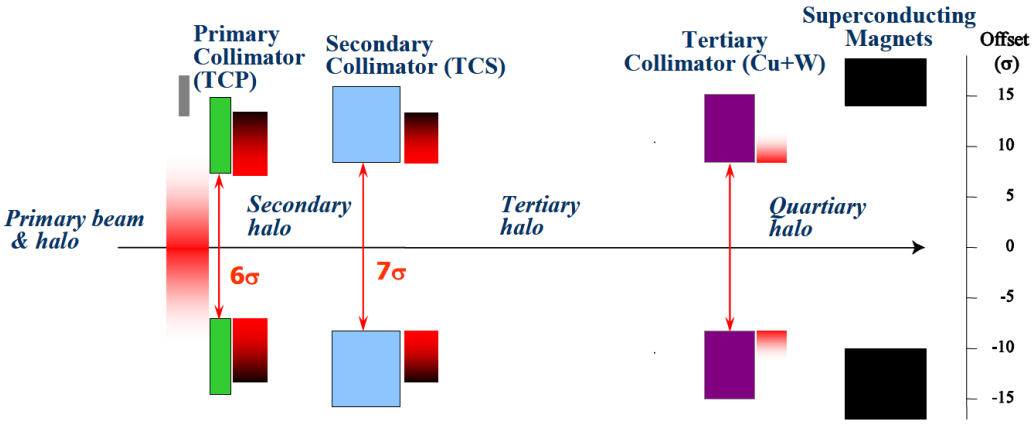

Fig. 7.1: Qualitative scheme of the LHC collimation system.

The TCT considered have the jaw in tungsten alloy, which is contained in a copper structure. The Lagrangian 3D numerical model (see Fig. 7.2) represents a simplified structure of the TCT respect to the original one, but it considers the presence of two different materials and the contact between the different model components. The Inermet block is modelled with the properties of pure tungsten one. Substantially, the structure is a parallelepiped with an internal part made in tungsten, which is the impacted part and corresponds to the active jaw of the collimator. The external part is made of copper and has a C-section.

The impacting bunches have 1.13×10^{11} protons each one, at the energy of 5 TeV (σ_x= 0.3 mm and σ_y= 0.19 mm). The FLUKA map calculated on the simplified component is reported in Fig. 7.3.

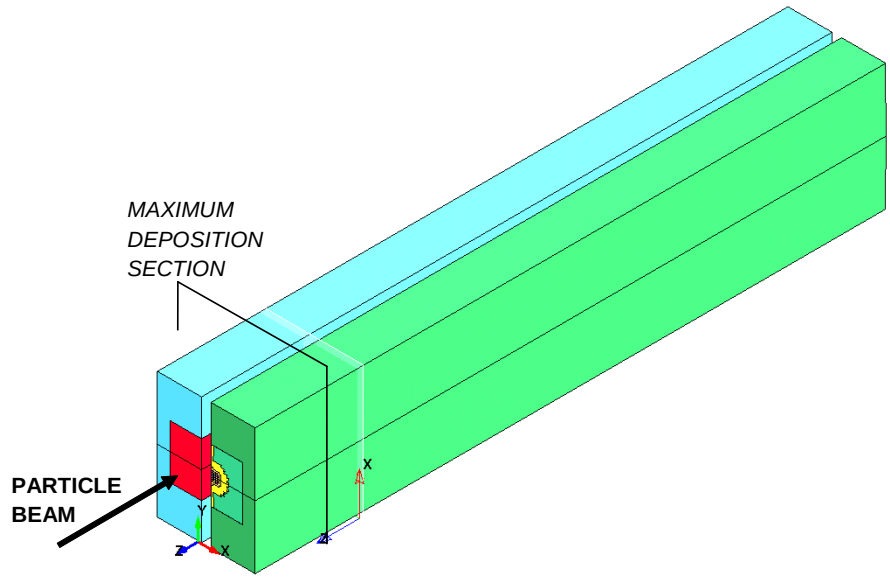

Fig. 7.2: 3D view of the simplified TCT.

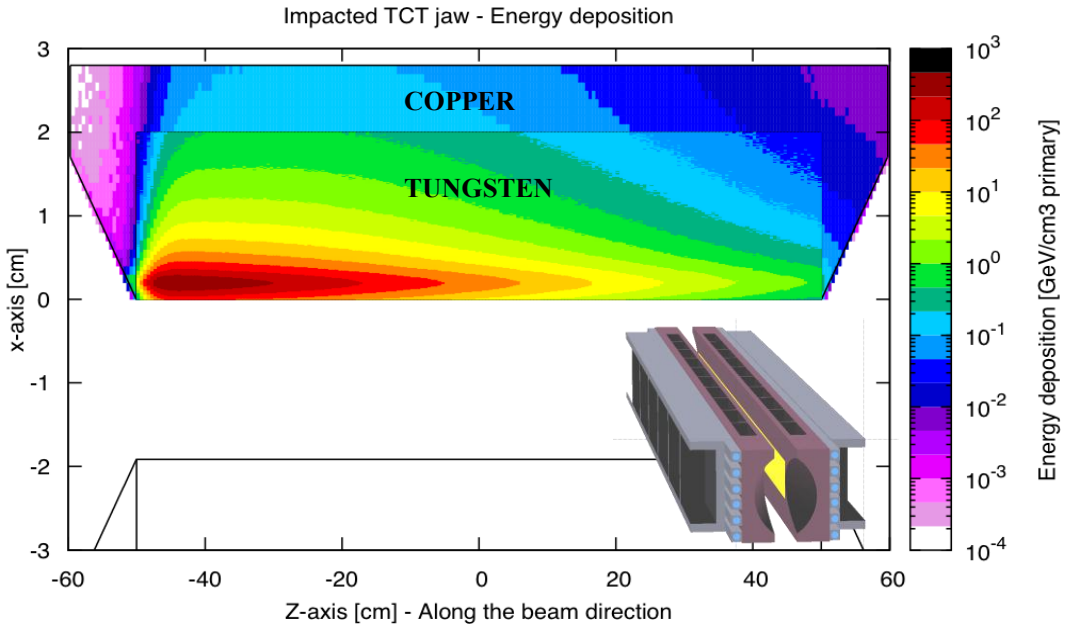

Fig. 7.3: Energy distribution (GeV/cm^3/p) on a tungsten/copper component (TCT jaw) for a single proton at 5 TeV.

For the simulation, the strength material model used for copper and tungsten is the S-G model [2]. For both the materials, a spall model is also defined. The EOS used for copper is reported in [3] and for tungsten is reported in [4]. All the data are reported in Tables 7.1 and 7.2.

In Figs. 7.4 and 7.5 some results obtained from the numerical simulation are reported

in terms of pressure and Von Mises stress. The results are shown on the section in the *y* direction, in which there is the maximum deposition energy. The results are reported both on the complete jaw (tungsten and copper) and on the copper C-component.

Table 7.1: S-G parameters for tungsten [2].

Parameter	Value	Unit	Parameter	Value	Unit
ρ_0	19300	kg/m^3	h_1	0.938×10^{-11}	Pa^{-1}
G_0	1.6×10^{11}	Pa	$h2$	1.38×10^{-4}	K^{-1}
σ_0	2.20×10^{9}	Pa	T_{m0}	4520	K
β	24	-	a	1.3	-
n	0.19	-	γ_0	1.67	-
$\varepsilon_{pl,i}$	0	-	A	183.84	uma
σ_{MAX}	4.00×10^{9}	Pa	P_{spall}	-9×10^{8}	Pa

Table 7.2: S-G parameters for copper [2].

Parameter	Value	Unit	Parameter	Value	Unit
ρ_0	8930	kg/m^3	h_1	2.83×10^{-11}	Pa^{-1}
G_0	48×10^{9}	Pa	h	3.77×10^{-4}	K^{-1}
σ_0	120×10^{6}	Pa	T_{m0}	1790	K
β	36	-	a	1.5	-
n	0.45	-	γ_0	2.02	-
$\varepsilon_{pl,i}$	0	-	A	63.546	uma
σ_{MAX}	640×10^{6}	Pa	P_{spall}	-1.9×10^{9}	Pa

During the deposition phase (0÷200 ns) the pressure evolution is quite similar to that of the 2D cylindrical case. The maximum level of pressure after the deposition of 8 bunches is lower with respect to the 2D case on tungsten, since the different beam intensity and size. Once the deposition is finished, the shock-wave starts its propagation and moves cylindrically from the impacted zone. Differently from 2D case, in which the beam hits the centre of the structure, in this case the material is hit near a free surface. For this reason, the pressure wave reaches in a short time the free surface of the tungsten part and is reflected back. The fact that this reflection occurs on a free surface implies that the

pressure wave is transformed in a tensile hydrostatic wave of the same intensity. The spall model limits the value of the negative pressure to the imposed threshold (P_{spall}). This condition corresponds to the failure of the material. The consequence is that the material is ejected from the surface at high velocity. The high level of particle speed in the material is a proof of shock-waves phenomena. Due to the presence of the other jaw, the spray of material may consequently provoke the damage of the other jaw.

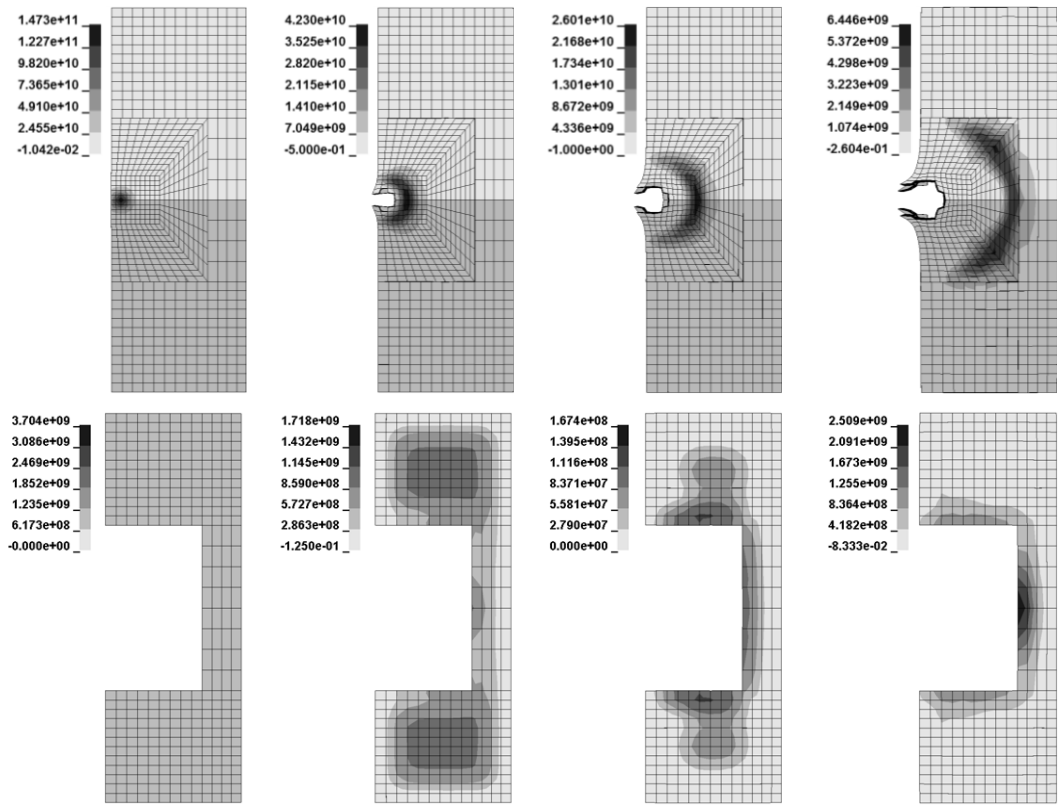

Fig. 7.4: Pressure distribution (Pa) on a tungsten/copper component (hit jaw of the TCT, top) and pressure distribution (Pa) on a C-copper component (hit jaw of the TCT, bottom) at 200, 1000, 2000 and 4000 ns from the impact.

The shock-wave, which is propagating in the opposite direction (towards the copper part), is then followed by a high negative pressure wave. When the pressure wave reaches the interface between the two materials, due to the significant difference in impedance, the shock wave is in part reflected in tungsten, with the potential spallation phenomena, and in part transmitted into copper, with a reduction of the pressure level. The results in terms of Von Mises stress in the tungsten part show that the material is heavily plastically deformed after the beam impact. In the molten part of the tungsten insert, the Von Mises

stress is zero and the behaviour is purely hydrodynamic. On the other hand, it reaches the maximum value just behind the shock front, as in case of 2D analysis. For what concerns the results in copper, Von Mises stress and pressure correlated to the propagation of the shock-wave from tungsten to copper, are those reported in distributions corresponding to the time of 4 μs. In the time steps before, Von Mises stress and pressure are correlated to the energy deposition in C-copper structure, which is much lower than in tungsten. The boundary effects are also visible.

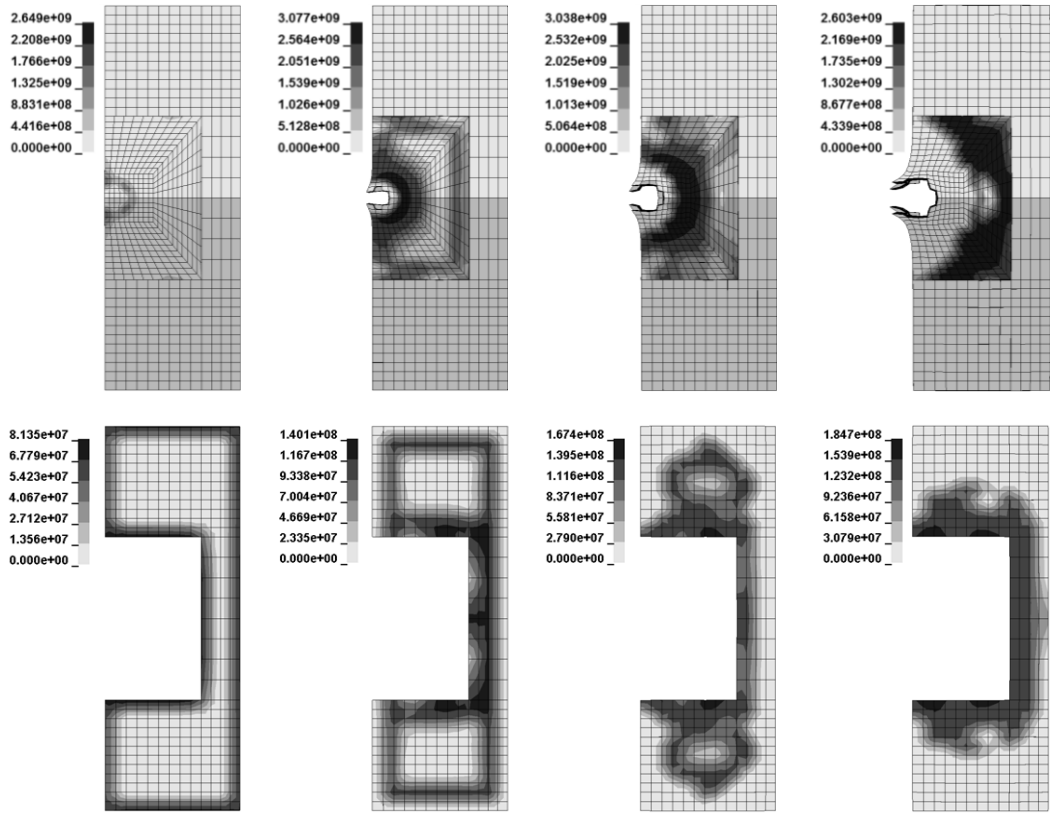

Fig. 7.5: Von Mises stress distribution (Pa) on a tungsten/copper component (hit jaw of the TCT, top) and Von Mises stress distribution (Pa) on a C-copper component (hit jaw of the TCT, bottom) at 200, 1000, 2000 and 4000 ns from the impact.

7.2 Soft coupling with FLUKA

The fact that the energy absorption of a material is strongly density dependent (as shown by the comparison of the deposition in copper and tungsten, see chapter 5), it means also that, for the same material, if there is a density evolution during the simulation,

it should be taken into account, in order to recalculate the energy deposition on the material in these new conditions. About the last point, for the previous cases (2D and TCT simulations), a preliminary approach was followed: the energy deposition on the material is calculated on the initial condition (for the density of the solid state) and then used during the entire multi-bunch impact simulation without any modifications. So, any effects, due to density modification consequent to the travel of the shock wave inside the material, were not taken into account.

To consider this effect, a soft coupling between FLUKA [5, 6] and FE code LS-DYNA [7] is developed, in collaboration with the FLUKA Team at CERN. The routine is implemented in Matlab and iteratively, runs FLUKA and LS-DYNA on a Linux platform (Fedora14).

The method is applied to simulate the beam impact against a tungsten geometry, which represents a parallelepiped of 21×35×1000 mm. The mesh is such that 21×35×200 elements are used, so the elements dimensions are 1×1×5 mm. The same discretization is used both for FE and FLUKA models. The Lagrangian 3D numerical model is built using solid elements with 1 integration point and is shown in Fig. 7.6.

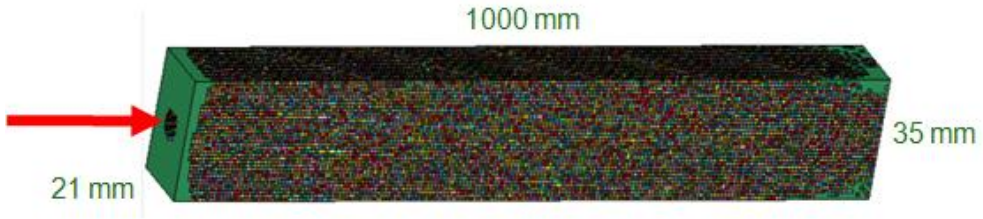

Fig. 7.6: 3D numerical model of a parallelepiped made in tungsten used for the simulation of a multi-bunch impact. (x,y,z): 21x35x1000 mm.

The FLUKA model is built using the voxel geometry [8]. A voxel is a tiny parallelepiped with equal size in the three dimensions, which forms a 3D grid. In principle this method can be applied with any geometry. In FLUKA it was implemented for nuclear medicine and radiotherapy applications. Voxel geometry is especially useful when translating a Computed Tomography (CT) scan of a human body into a dosimetry phantom. Therefore, the word “organ” indicates a group of voxels (or even more than one group) made of the same material, e.g. Fig. 7.7.

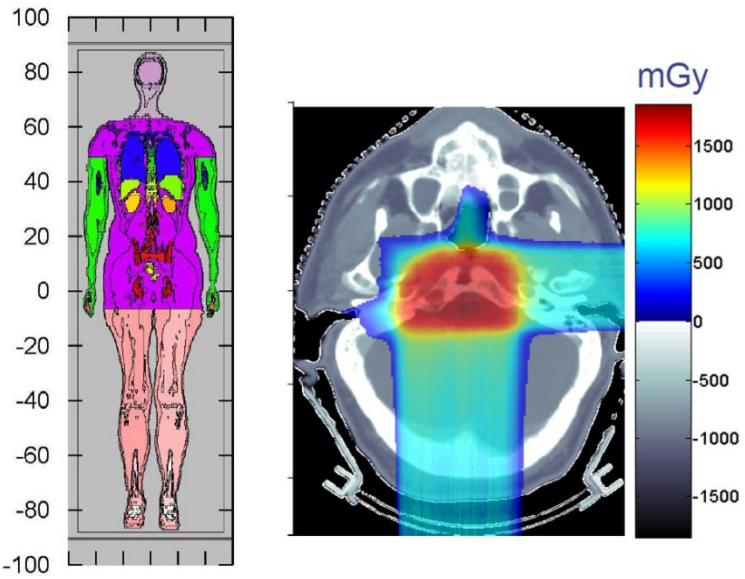

Fig. 7.7: Voxel geometry examples [8].

7.2.1 Procedure

The method applied implies that, first of all, before starting, it is necessary to define a sufficient number of primaries, needed to achieve a good precision on the energy deposition and beam size and intensity. Then, the first FLUKA calculation is run, considering that the entire target is solid. As next step, the first FE mechanical analysis is run. At this point the iterative procedure starts and will terminate when the desired number of bunches impact against the target. Each iteration contains the deposition phase (0.5 ns) and the successive free phase (25 ns). At each iteration, the coupling algorithm:

- takes as input the density map resulting from the FE calculation and defines discrete density levels. A maximum of 500 density levels are available as each level corresponds to an independent FLUKA material;
- defines, using a voxel structure, the regions with different density in the target block and associates to each voxel the corresponding material with the correct density;
- stores the energy deposition for each voxel, and runs the new FLUKA simulation;
- takes as input the energy map resulting from FLUKA calculation and defines discrete energy levels. A maximum number of 10000 energy levels are allowed;
- generates the new FE model. At this step the main points are: to associate to each

FE element the corresponding energy and interpolate the SESAME EOS for getting the polynomial coefficients for each element;

- restarts the mechanical LS-DYNA simulation for the next bunch;
- analyzes the results in order to get the density map for the construction of the new FLUKA model.

The FLUKA calculation is performed for a proton bunch at 7 TeV. The beam dimensions are taken from a real physics case of the accident loss on the TCT located to the left of the IR5 interaction region, where the full width at half maximum of the beam are 0.12 cm and 0.076 cm along the *x* and *y* axis, respectively. A total of about 20000-30000 primaries are simulated, depending on the required precision. The time required for the simulation is reduced by splitting the CPU-demanding tasks over about 30-40 CPU cores.

A more detailed description of the generation of the new FE model is required. In LS-DYNA a total number of 10000 EOS is defined for each model. The identifier number of the EOS, for each element, is constructed in an appropriate way, as combination of temperature, density and energy of that element.

Since the total number of elements (147000) is greater than the allowed number of EOS, it is not possible to create a specific EOS for each element, but it is necessary to group the elements. First of all, the discretization of the energy deposition is performed. To do this the number of levels is decided and then the discretization is performed on the logarithm of the energy. At this point, the correct energy value is assigned to each element.

The ID number of the EOS is obtained also on the basis of the state of the element on the EOS surface. Differently from the cases presented before, the entire SESAME EOS is divided into a certain number of regions a priori. The number of regions depends on the discretization in density and temperature (which are the independent variable of a SESAME table). Each region is labelled with a number, which identifies the density and the temperature at the middle of the region.

On each region a linear interpolation is performed. The assignment of the right coefficient to each element of the FE model is performed on the basis of its density at the beginning of the iteration (which corresponds to the value assumed at the end of the previous step) and the amount of energy absorbed (discretized). This condition identifies a precise state on the EOS surface and, consequently, it corresponds to a precise region in

which the EOS is divided. At this point the ID number of the EOS is completed.

As final step, a control on the total number of EOS is performed. If the total number exceeds the allowed one, the procedure of the assignment of the ID number is remade, reducing the initial number of levels for the energy discretization (the number of regions in which the EOS is divided are fixed), until the number of total EOS is exactly 10000. The same is made also if the total number of EOS is lower than the allowed one. In this case, the procedure is remade increasing the number of levels for the energy discretization. This allows using the maximum number of energy levels for each simulation, achieving the best discretization as possible. The update of the FLUKA map not performed at each bunch, but preliminary studies suggested that updating every 5 bunches is sufficient.

7.2.2 Results

In Figs. 7.8-7.10, some results of the numerical analysis are reported in the *x*-*z* section of the target. In more details, the results are in terms of energy calculated by FLUKA, pressure and density maps, corresponding to the bunches number 1, 10, 20, 30, 40, 50 and 60. The results are shown for the end time of each simulation (after the free phase in which there is not the deposition, 25 ns).

Looking at the results of Fig. 7.8, it is possible to notice that the energy distribution on the target changes, both in values and shape, during the deposition phase. This is a direct consequence of the density variation, reported in Fig. 7.9.

As a matter of fact, the material, in which a great amount of energy is deposited, is subjected to a significant density reduction during the free expansion phase (25 ns before the arrival of the next bunch). This implies that the material becomes more transparent to the next proton bunch, and consequently the probability of interaction decreases. This provokes the so called tunnelling effect. The consequences of this are that the proton beam penetrates more in depth in the material in the axial (*z*) direction and the energy is more diluted over the target.

The results in terms of density emphasize the tunnelling: the density modification involves higher longitudinal coordinates increasing the number of bunches. After 60 bunches the total length of the target experiences a reduction in density in the zone around the beam axis.

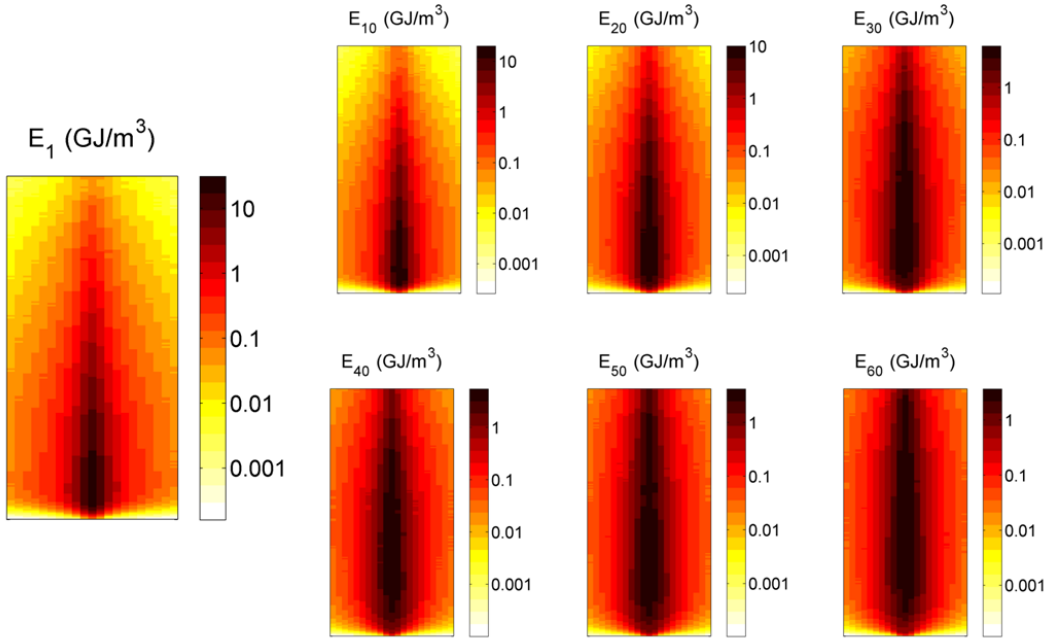

Fig. 7.8: Energy distribution on the tungsten target in the z (↑)-x (→) section corresponding to the maximum energy deposition in the y direction: results for the bunches number 1, 20, 30, 30, 40, 50 and 60 after the free phase (the x dimension is amplified).

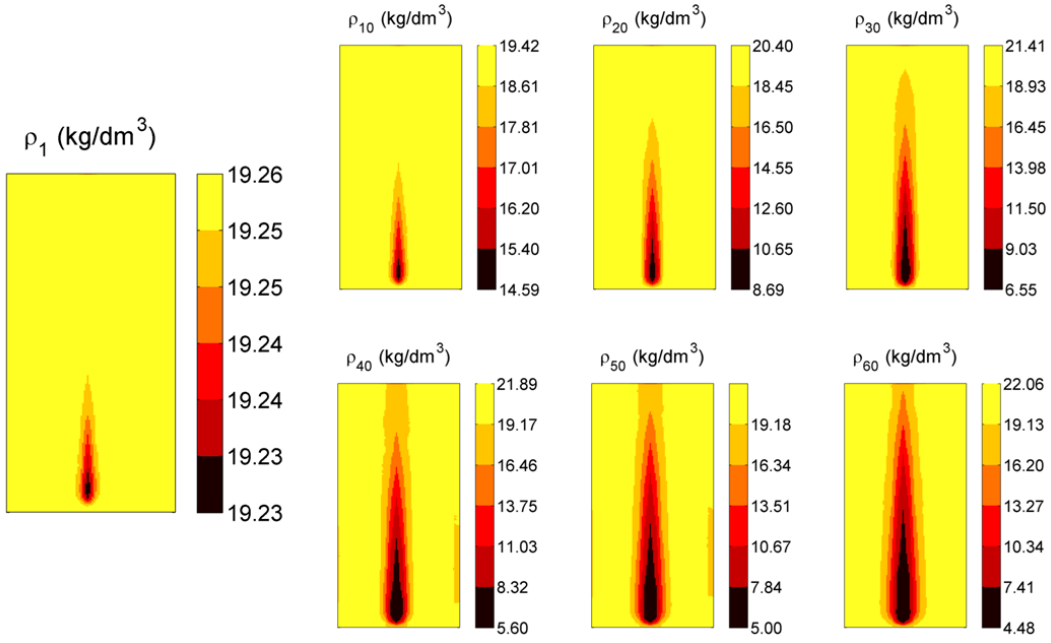

Fig. 7.9: Density distribution on the tungsten target in the z (↑)-x (→) section corresponding to the maximum energy deposition in the y direction: results for the bunches number 1, 20, 30, 30, 40, 50 and 60 after the free phase (the x dimension is amplified).

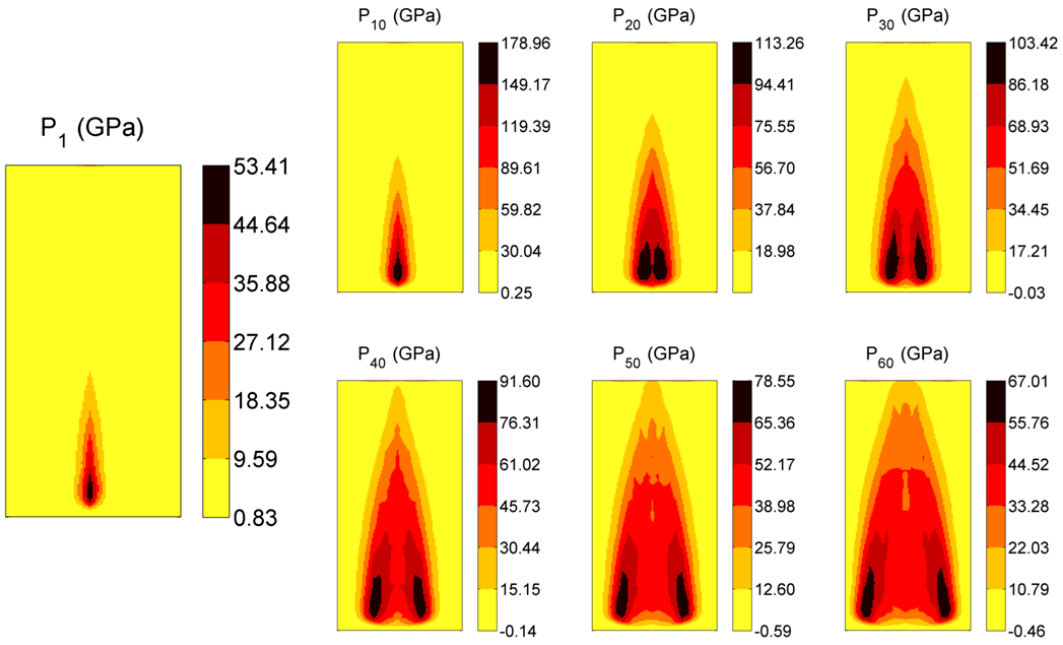

Fig. 7.10: Pressure distribution on the tungsten target in the z (↑)-x (→) section corresponding to the maximum energy deposition in the y direction: results for the bunches number 1, 20, 30, 30, 40, 50 and 60 after the free phase (the x dimension is amplified).

The results in terms of pressure (Fig. 7.10) show that the maximum of pressure remains more or less in the same longitudinal position with respect of the first bunch, but the pressure wave starts to travel in the *x* direction. Since the pressure wave generated is cylindrical (due to the shape of the energy deposition), the same happens also in the *y* direction. The fact that the energy deposited by the following bunches is lower and more widespread, with respect to that calculated for the first bunch impacting the solid material, implies that the pressure increment, consequent to the next bunches, is reduced in the zone, in which the first bunch deposited a great amount of energy. On the other hand it should increase in the part of the target, in which there is an increment in density.

In order to better appreciate the differences with an uncoupled simulation, the same case is simulated without changing the energy map. The results in terms of pressure and density, obtained from the two cases are compared in Figs. 7.11-7.13 for the bunches number 20, 40 and 60. The results are shown fixing the scale to that of the uncoupled simulation. Looking qualitative the results, it is possible to appreciate that the shock wave penetrates more in the component with a consequent reduction in the pressure level, in case of coupled analysis.

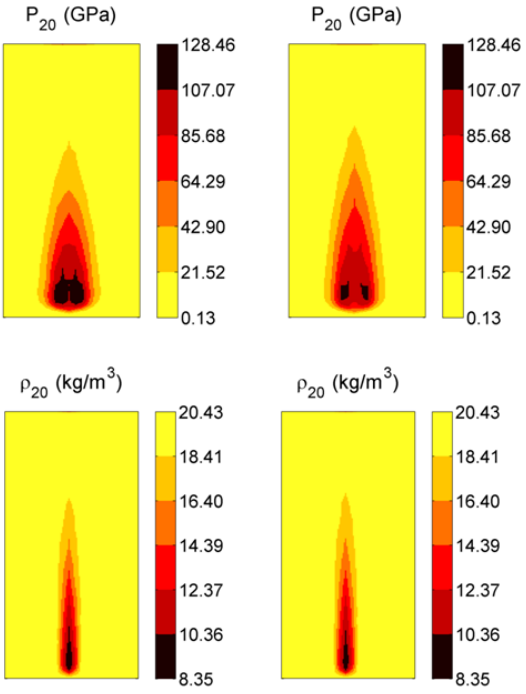

Fig. 7.11: Pressure (top) and density (bottom) distributions on the tungsten target in the z (↑)-x (→) section the bunch number 20 in case of non-coupled (left) and coupled (right) simulations (the x dimension is amplified).

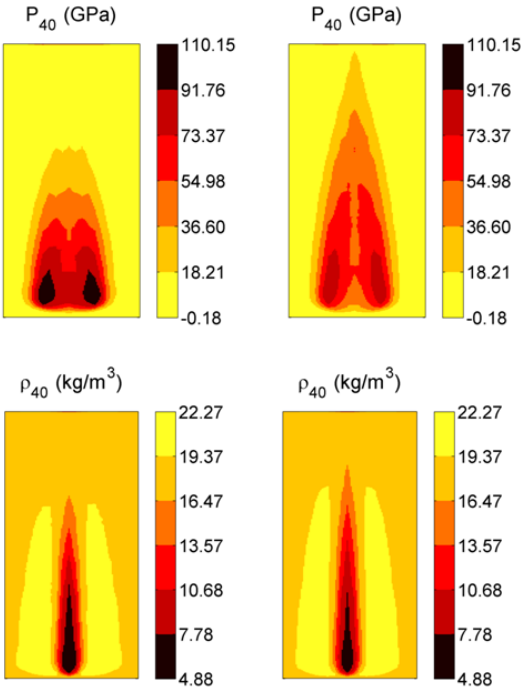

Fig. 7.12: Pressure (top) and density (bottom) distributions on the tungsten target in the z (↑)-x (→) section for the bunch number 40 in case of non-coupled (left) and coupled (right) simulations (the x dimension is amplified).

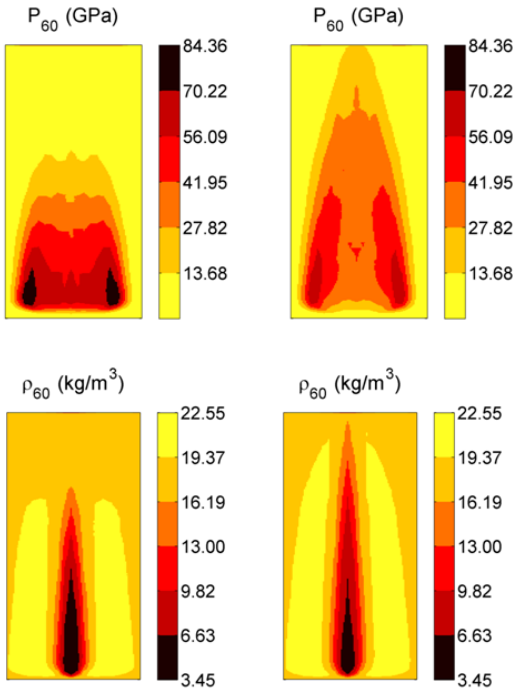

Fig. 7.13: Pressure (top) and density (bottom) distributions on the tungsten target in the z (↑)-x (→) section for the bunch number 60 in case of non-coupled (left) and coupled (right) simulations (the x dimension is amplified).

In case of coupled simulation the pressure decreases in the region where there is the maximum deposition at the beginning while increases in the longitudinal direction due to the more in depth penetration of the beam. This provokes a substantial modification in the pressure distribution over the target. On the other hand, the shape and the values of density distribution appear less different in the two cases, but however a greater reduction can be observed along the beam axis direction in the coupled simulation. The fact that the density is similar in the two cases, but the energy deposited in the uncoupled case is higher near to the hit face and lower increasing the longitudinal coordinates, is sufficient to explain the differences in pressure. As a matter of fact, the state in term of pressure is completely defined on the EOS knowing the density and the energy. Considering the same density, the pressure is higher where the energy is higher. The differences between the two cases become more relevant increasing the number of bunches.

Looking at the results in terms of pressure vs. number of bunches (Fig. 7.14) on a single element, obtained from coupled and uncoupled simulations, it is possible to directly compare the pressure evolution. The diagrams of Fig. 7.14 are obtained for four elements situated at different longitudinal coordinates along the beam axis direction (r = 0). The longitudinal positions of the four elements are: 60 mm (coordinate in which the maximum level of energy is deposited), 250, 500 and 750 mm. The levels of pressure reported in the

diagrams correspond to the end time of each simulation. For this reason, the diagram does not show the characteristic trend similar to a sawtooth wave, as shown in the previous chapter in Fig. 6.7 and 6.17.

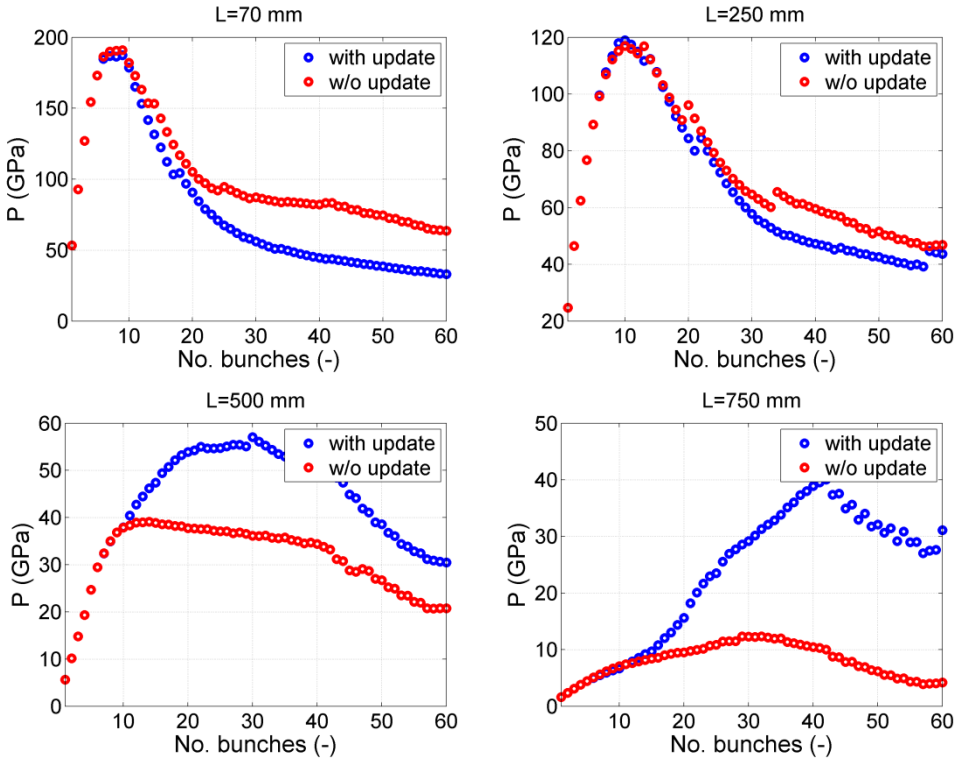

Fig. 7.14: Pressure in function of the number of bunches deposited on the target obtained for four elements situated at different longitudinal coordinates along the beam axis direction: comparison between coupled and uncoupled analysis.

The points reported in the diagrams of Fig. 7.14 correspond to the minimum values of the previous ones. As it is possible to notice, until 8-10 bunches (~200 ns), the differences between the two simulations are negligible for all the elements. Thanks to this, it is possible to conclude that the results obtained from the previous analysis (2D and TCT simulations) can be considered reliable, since the maximum number of impacted bunches was 8. After this time however, the change in density becomes relevant, because the shock-waves has the time to travel away from the hit zone producing a great rarefaction in the middle. The consequence is that the two simulations give more and more different results increasing the number of bunches. In particular two situations can be developed, depending on the position of the elements. For the elements situated in the neighbourhood of that in which the maximum energy is deposited, the uncoupled simulation

overestimates the pressure. This can be easily explained since those elements are subjected to the greatest density variation. Consequently they becomes more transparent to the proton beam and the successive bunches deposit on them lower energy, which implies lower growth in pressure. Otherwise, elements that are situated along the beam direction at higher longitudinal coordinates (far from the maximum energy region), are subjected to higher energy deposition during the successive bunches due to the tunnelling effect with respect to the first bunch. Obviously, this provokes an underestimation of the pressure level in case of uncoupled analysis.

7.2.3 Mesh influence

The previous case demonstrates that the method applied works and is able to describe the tunnelling effect. Once, the method is tested and validated, also the mesh influence (both for FE and FLUKA models) is evaluated varying the elements (or bin) dimension and the number of primaries used for the FLUKA calculation.

Three cases are analyzed, in which a total number of 8 bunches impact against the target. Knowing the results obtained for the coarser case, these simulations are made without performing the update of the energy deposition.

The coarser case corresponds to the previous one, in which the element dimensions are 1×1×5 mm, so the total number of elements is 21×35×200. In the intermediate case the element dimensions are 0.5×0.5×2.5 mm, so the total number of elements is 42×70×400. In the finest case, the element dimensions are 0.2×0.2×2.5 mm, so the total number of elements is 105×175×400. The numbers of primaries used in three cases are 20000-30000.

In Fig. 7.15, the energy deposition, calculated for the first bunch, is reported for the three cases. As it is possible to notice, a finer discretization allows appreciating with more precision the energy pick of the deposition. The results in terms of pressure, density and Von Mises stress are shown Figs. 7.17-7.19, for the bunch number 8. The distributions of these quantities are reported fixing the scale to that corresponding to the finest case in. From a qualitative point of view, comparing the three cases, it is possible to conclude that globally they produce the same results.

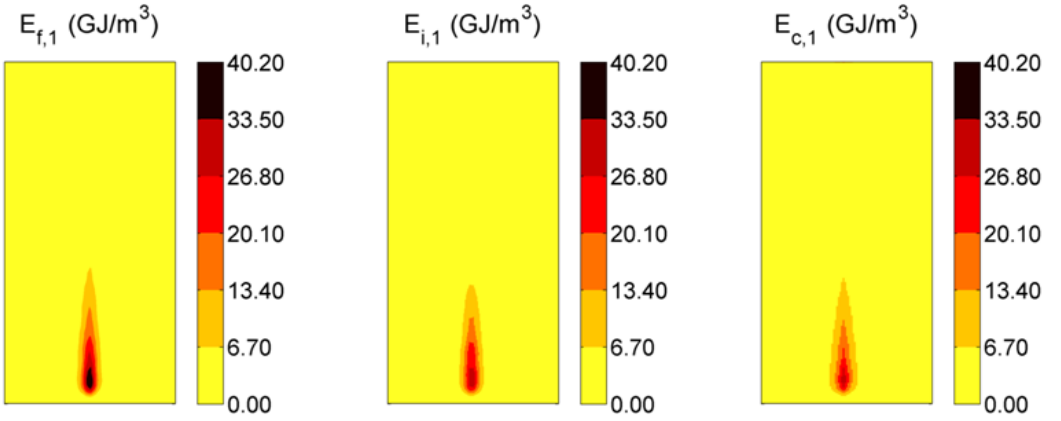

Fig. 7.16: FLUKA energy distribution on the tungsten target in the z (↑)-x (→) section corresponding to the maximum energy deposition in the y direction, for the three cases: fine (f), intermediate (i) and coarse (c) discretization (the x dimension is amplified).

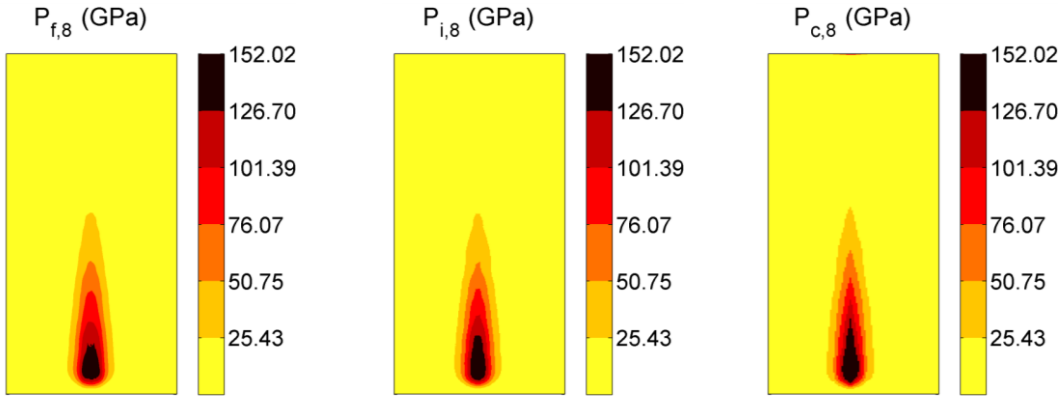

Fig. 7.17: Pressure distribution on the tungsten target in the z (↑)-x (→) section corresponding to the maximum energy deposition in the y direction. Results for the bunch number 8 for the three cases: fine (f), intermediate (i) and coarse (c) discretization (the x dimension is amplified).

The finest case implies a more in depth penetration of the beam respect to the other ones and obviously a more defined and smooth distribution of the quantities over the target. The maximum pressure level reached after eight bunches is lower for the finest case but it is associated to a more significant reduction in density, which is compatible with a higher tunnelling effect. For the Von Mises stress the same observation can be made. The central zone in which the Von Mises stress is zero corresponds to the part of target which is not still solid.

As conclusion, it is possible to assess that, surely considering a finer simulation produces more accurate results, but obviously with a high computational cost. So, if the

aim of the simulation is just to appreciate the phenomenon evolution, evaluating the entity of the shock-wave, also a coarser simulation can be sufficient, especially for what concerns the mechanical quantities. On the other hand, for a precise estimation of the quantity variation on the target, a finer simulation is needed.

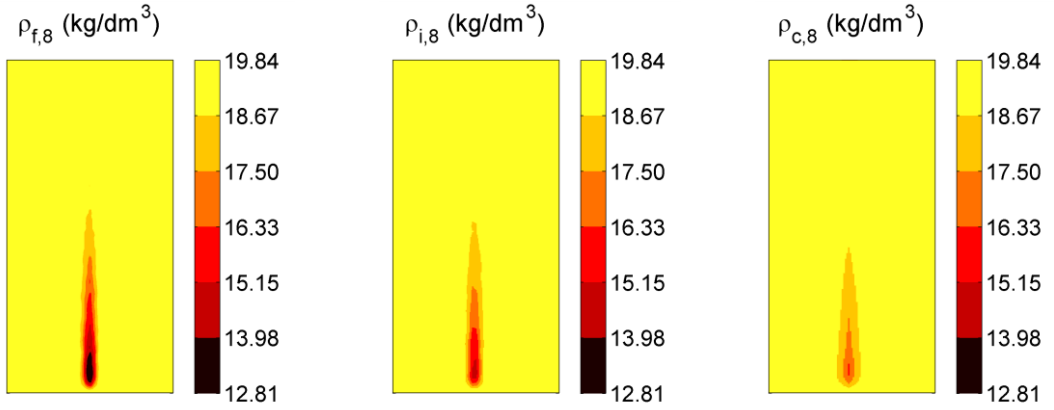

Fig. 7.18: Density distribution on the tungsten target in the z (↑)-x (→) section corresponding to the maximum energy deposition in the y direction. Results for the bunch number 8 for the three cases: fine (f), intermediate (i) and coarse (c) discretization (the x dimension is amplified).

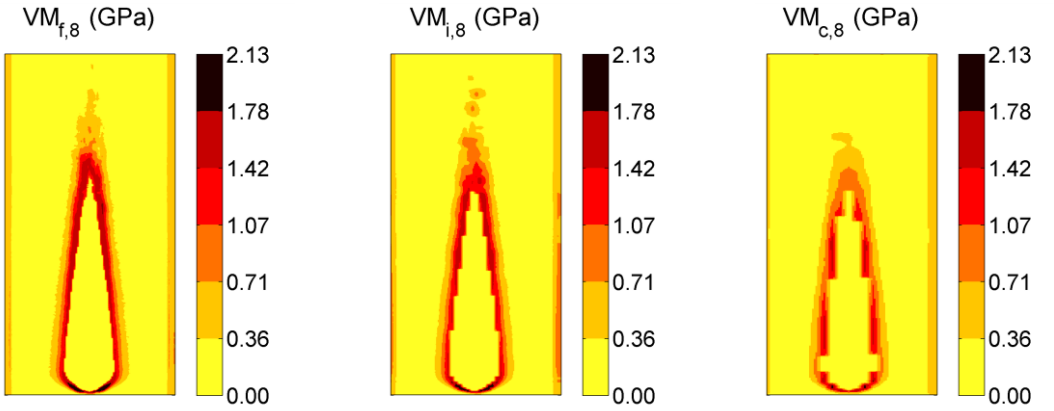

Fig. 7.19: Von Mises stress distribution on the tungsten target in the z (↑)-x (→) section corresponding to the maximum energy deposition in the y direction. Results for the bunch number 8 for the three cases: fine (f), intermediate (i) and coarse (c) discretization (the x dimension is amplified).

Just to give an idea of the computational cost, the coarse simulation takes xx the LS-DYNA simulation, while in case of the finest one it takes xx. It is more or less insensitive to the number of bunches, since in each simulation the maximum number of allowed EOS is used. The computing time for FLUKA calculations depends on several factors, among which the number of transitions between regions with different density. For this reasons,

the time needed for the FLUKA calculation at the first step is the same both in case of fine and coarse cases. As example, it takes 1-2 hours over 10 CPU cores. Obviously the time needed for the finest calculation increases a lot, with respect to the coarsest one, increasing the number of bunches, to which correspond a greater number of assigned densities.

References

[1] Redaelli S., et al., "Operational performance of the LHC collimation", Proceedings of HB2010 (2010).

[2] Steinberg, D.J., Equation of State and Strength Properties of Selected Materials, Lawrence Livermore National Laboratory, UCRL-MA-106439, (1996).

[3] Kerley, G.I., "Equations of State for Copper and Lead", KTS02-1 (2002).

[4] Kerley, G.I., "Equations of State for Be, Ni, W, and AU", SANDIA REPORT SAND 2003-3784 (2003).

[5] Battistoni G., Muraro S., Sala P.R., Cerutti F., Ferrari A., Roesler S., Fasso` A. and Ranft J., "The FLUKA code: Description and benchmarking", Proceedings of the Hadronic Shower Simulation Workshop (2006), Fermilab 6--8 September 2006, M. Albrow, R. Raja eds., AIP Conference Proceeding 896, 31-49, (2007).

[6] Fasso A., Ferrari A., Ranft J. and Sala P.R., "FLUKA: A Multi-Particle Transport Code", CERN-2005-10, INFN/TC_05/11, SLAC-R-773 (2005).

[7] Gladman B. et al., "LS-DYNA® Keyword User's Manual – Volume I – Version 971", LSTC (2007).

[8] "Voxel and medical applications", 7th FLUKA course (2008).

8. HiRadMat experiment

In this chapter, a first-of-its-kind experiment is described. It consists of impacting materials with high energy proton beam, measuring the material response. The aim is to validate numerical models and extract material data in terms of strength and EOS models. The experiment was performed in the HiRadMat facility at CERN in October 2012. In the first part, the description of the experiment is reported, focusing the attention on the most relevant aspects of the design phase, including the choice of the impact conditions. Then, a brief description of the materials analyzed is reported. In the final part, a summary of the instrumentation used for the measurements is reported before the description of some preliminary results, which are available up to now.

Predicting the consequences of highly energetic particle beams accidentally impacting protection devices, as collimators, or other Beam Intercepting Devices (BID) is a fundamental issue in protection and design of modern particle accelerators. As shown in the previous chapters, such complex dynamic phenomena involves material phase transitions, extended density changes, shock waves propagation, explosions-like phenomena, material fragment projections etc. From this follows the need to develop suitable method for the simulation of such events, using highly non-linear numerical tools (FE and Hydro-codes).

However, to produce accurate results, the definition of reliable material constitutive models are required, but, at the extreme conditions induced by a high energy particle beam impact, are, up to now, scarce and inaccurate.

In order to derive and/or validate material models (in the sense of equations of state, strength and failure models), a comprehensive, first-of-its-kind experiment was designed at CERN using the HiRadMat facility.

HiRadMat is a short for High Radiation to Materials [1], a new facility developed at CERN for the study of the effects induced in materials as consequences of high energy impact of intense pulsed beams. The aim is to have a reliable facility for testing material and components of the accelerator, in order to study and, eventually, avoid or constrain damages, which, otherwise, should be catastrophic for the entire machine.

The facility uses, when it works with protons, the beam extracted from SPS (see Fig. 8.1). The beam energy is 440 GeV with a pulse length of 72 μs. The beam spot size and the beam intensity can be varied, allowing testing materials at different deposited energy levels.

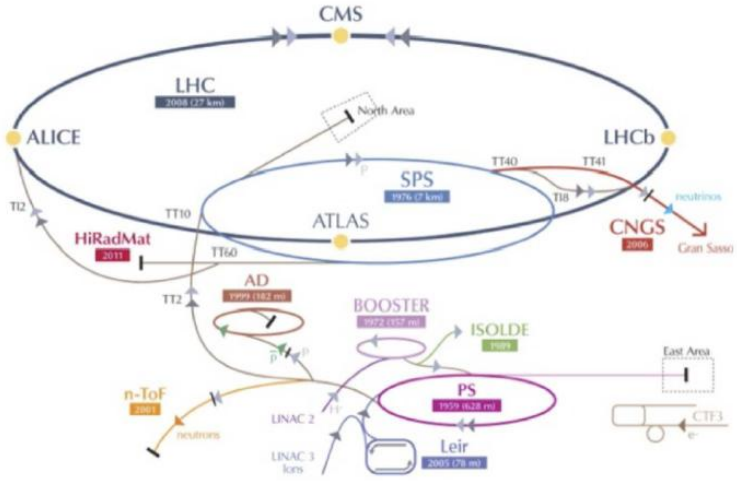

Fig. 8.1: Scheme of the CERN accelerator complex: identification of the HiRadMat site.

8.1 HRMT-14

In this chapter one of the experiments performed this year in the HiRadMat facility is reported. The name of the experiment is HRMT-14 and was performed in October 2012. The objective of this experiment is performing experimental tests, in which controlled impact of intense and energetic proton beams are induced on six different materials. Tests were run at two levels of intensity (medium and high intensity), using the Super Proton Synchrotron (SPS) proton beam, which has an energy of 440 GeV. The experimental method adopted may find applications to test materials under very high strain-rates and temperatures in domains well beyond particle physics (such as, severe accidents in fusion and fission nuclear facilities, space debris impacts, high power targetry, fast and intense loadings on materials and structures etc.).

The experimental data were obtained from strain-gages, temperature sensors, Laser Doppler Vibrometer (LDV) and high speed camera. The quantities measured during the experiments are: longitudinal and hoop strain, radial velocity and temperature. Data were collected at very high sampling rates to fit expected shock wave profiles with sufficient accuracy. Microphones were also installed, as well as vacuum pressure gauges. Projections of particles, generated by the beam impact, were filmed by a high-speed camera. Moreover, an in depth post-irradiation analyses are foreseen, once the specimens have reached a sufficiently low level of activation. In the next paragraphs, some aspects of the design phase are discussed and some preliminary results are shown.

8.1.1 Materials

The multi-material sample holder was designed to hold six different materials: Inermet® 180, Glidcop® AL-15, Molybdenum, Molybdenum-Copper-Diamond (MoCuCD), Copper-Diamond (CuCD) and Molybdenum-Graphite (Carbon Fibers) (MoGR). The first three materials are conventional pure metals or alloy, which are currently used as materials for some structural parts of the collimation system. The last three material are novel composites, currently under intense development and testing [2, 3], since they are good candidates as material for jaw in the phase II collimators.

Inermet® 180 is a commercial tungsten heavy alloy, which combines excellent thermal and mechanical properties with high density. The material is obtained by liquid-phase sintering of a powder mixture composed of tungsten (95%), nickel (3.5%) and copper (1.5%); 100μm-large tungsten grains are immersed in the low-melting Ni-Cu phase, which provides thermal and electrical continuity (Fig. 8.2). Besides, nickel enhances the diffusion of tungsten atoms through the grain borders improving particle adhesion, thus increasing mechanical properties.

Molybdenum is produced by sintering of pure powders at temperatures over 2000 ˚C; the material is later cold-worked to achieve 50% reduction in thickness. In the lamination direction, the fracture elongation can thus reach up to 40%. The microstructure is made of stretched Mo grains with small inclusions, mostly of Mo_2C, finely dispersed into the matrix (Fig. 8.3).

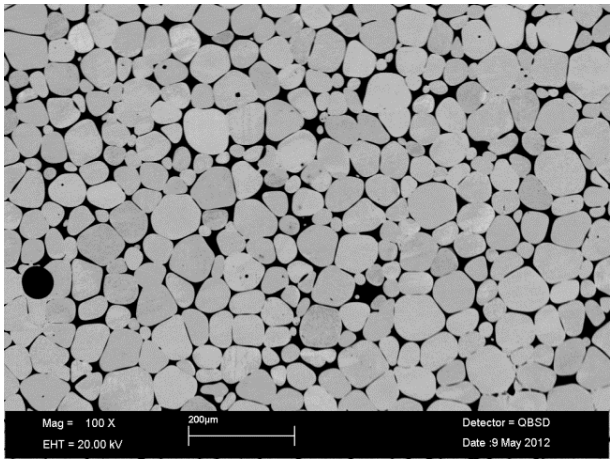

Fig. 8.2: SEM observations with backscattered electron detector of Inermet® 180 microstructure.

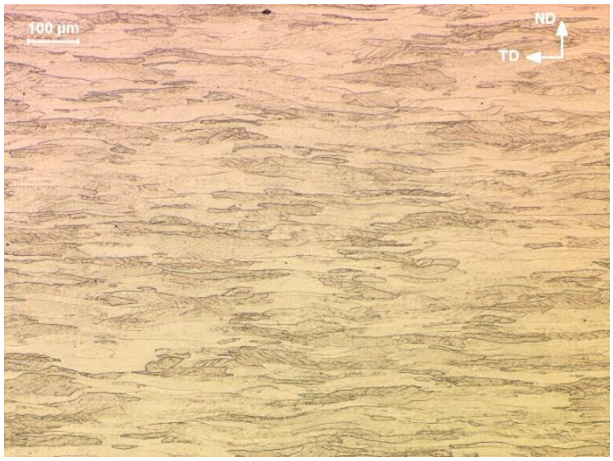

Fig. 8.3: Optical microscope observation of cold worked molybdenum.

Glidcop® AL-15 is an alumina-strengthened copper produced from copper grains with a small percentage of aluminium, mixed with copper oxide powders. The solid-state reaction generates alumina particles (Fig. 8.4), finely dispersed into the matrix, which reduce dislocation movements and grain growth at high temperatures. As a result, the material keeps good mechanical strength at high temperatures, while maintaining thermo-physical properties comparable to those of pure copper.

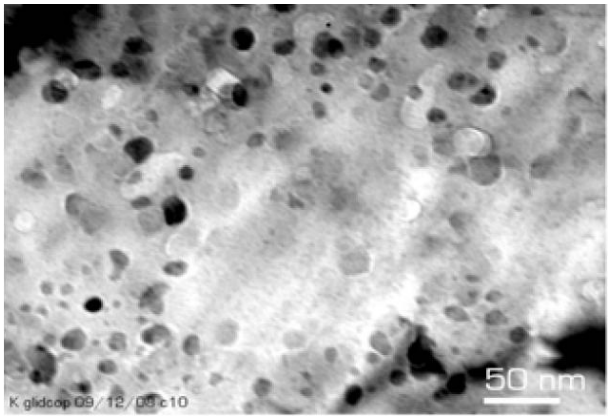

Fig. 8.4: Glidcop® AL-15 microstructure: small alumina particles dispersed into the copper matrix are visible.

Molybdenum-Copper-Diamond is a novel composite material jointly developed by CERN and an Italian SME, BrevettiBizz (Verona): goal of the R&D program is to combine the mechanical strength and electrical conductivity of metals with the high thermal properties (such as low CTE and low density) of diamond. The material is obtained by liquid-phase sintering of small synthetic diamonds (40%), pure molybdenum (35%) and pure copper powders (25%) through rapid hot-pressing. During the sintering process at 1200°C, molybdenum forms stable carbides on the surface of diamonds, improving mechanical adhesion of the elements; on the other hand, the temperature is not high enough to extensively sinter molybdenum grains: the addition of a low-melting filler increases the compaction rate (Fig. 8.5). Copper also enhances thermal and electrical properties.

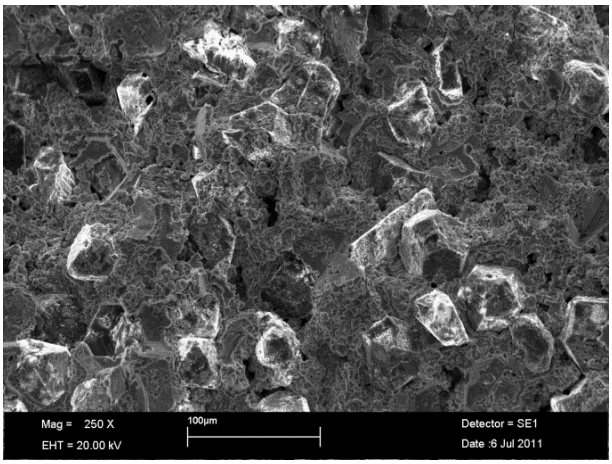

Fig. 8.5: SEM view of MoCuCD microstructure: 45µm-large diamonds embedded inside the Mo-Cu matrix.

Copper-Diamond (CuCD) has been developed by AIT (Austrian Institute of Technology, Seibersdorf, A), now RHP-Technology, and studied for particle accelerator applications in the frame of the EuCard collaboration. CuCD is made of 60% synthetic diamonds, 39% copper powder and 1% boron powder, mixed and sintered through rapid hot pressing: diamonds enhance the material thermal conductivity while decreasing density. Boron forms carbides at diamond interfaces and slightly dissolves in copper, assuring mechanical bonds between the two main phases. This interface has, however, inherent limitations due to the brittleness of boron carbides and to its reduced extent (Fig. 8.6).

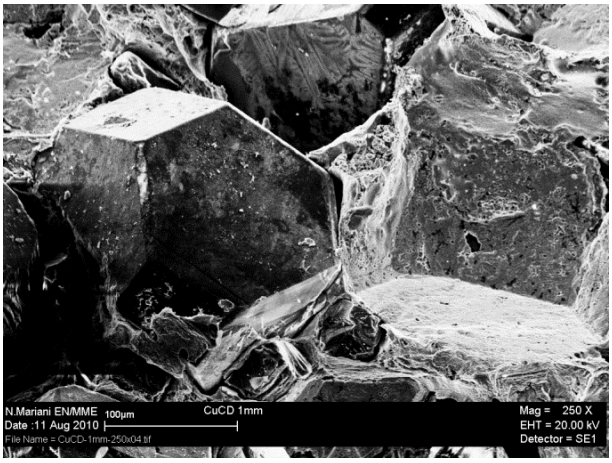

Fig. 8.6: SEM view of CuCD: 175µm diamonds surrounded by the Cu phase. The white spots on diamond surfaces are boron carbides.

The presence of low-melting phases inside MoCuCD and CuCD strongly affects the resistance of these materials in case of beam impacts. To overcome this limitation, a new composite has recently been co-developed by CERN and BrevettiBizz: Molybdenum-Graphite (MoGR).

The preferential recrystallization of {1000} graphite planes during rapid hot pressing at temperatures up to 2200º C leads to a heavily anisotropic structure, assuring high thermal properties in the principal direction and fair mechanical properties. The high mobility of carbon atoms favours a solid-state reaction between molybdenum and graphite, which generate Mo_2C; a secondary MoC phase, finely dispersed inside the primary carbide phase, is also formed. Fig. 8.7 shows recrystallized graphite grains (black), Mo_2C primary phase (light grey) and MoC inclusions (black acicular bands inside the Mo_2C grains). In order to further increase the thermal properties of MoGR, the addition of carbon fibres

(Fig. 8.7) is currently under development; first tests show that the thermal conductivity is substantially increased, although their presence tends to lower the compaction rate, somehow reducing mechanical strength. Further developments are therefore aiming at minimizing material porosities.

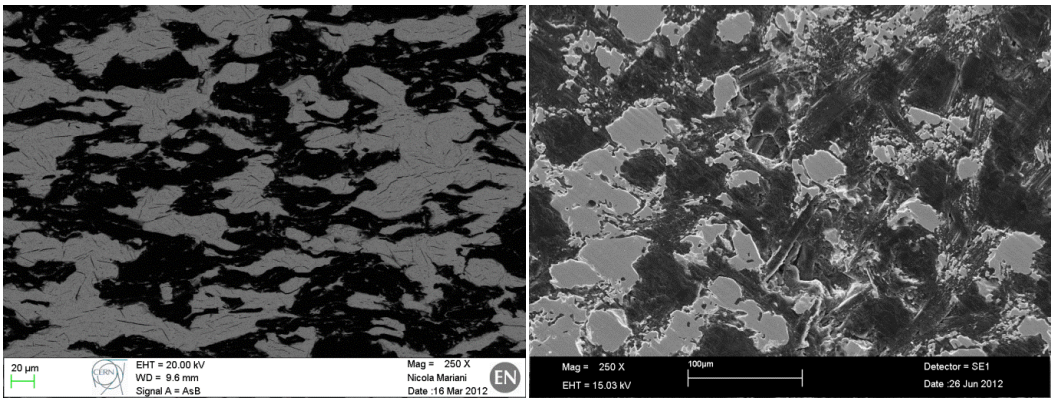

Fig. 8.7: MoGR without carbon fibres (left); MoGR with carbon fibres: porosities are clearly visible (right).

8.1.2 Samples

Two different specimen shapes (Fig. 8.8) were chosen for each material to be tested, with the aim to generate different material response. In both cases, the guidelines for the design of the experiment were developed on the basis of existing numerical results. Totally, 12 material samples were investigated (6 for each type). The model of the sample holder is shown in Fig. 8.9.

The first idea was to develop specimens for the study of the cylindrical shock-wave propagation (type 1). As discussed in chapter 6, this condition is generated if the beam impacts a cylindrical specimen perpendicularly at the centre of one face. For this reason, the first type of specimen reproduces a cylindrical geometry. The diameter of the samples was designed in order to avoid too high deformation on the external surface (where strain-gages are glued). The good compromise was 40 mm. The length of each specimen was decided on the basis of the capability of each material to absorb energy. As a matter of fact, as discussed in chapter 6: the higher the density, the higher the energy absorption. In more details, the length of the specimen is decided in function of the radiation and nuclear interaction lengths of the sample material: longer specimens are needed in case of low density material. In any case, for each material the specimen was divided in a series of small cylinders, each 30 mm long. The maximum number of sample for each material is

10. On these samples, medium intensity tests were performed.

For the second type of tests, half-moon cross section specimens were used (type 2), with the same diameter and length were of type 1 and with the flat surface 2 mm distant from the centre of the cylinder. In this case, high intensity impacts were considered and the beam hit the material nominally 2 mm inside with respect to the flat surface. The main goal of this experiment is allowing extreme surface phenomena (melting, material explosion, debris projections etc.) to be visualized and optically acquired. In both the types of specimen, each single cylinder was supported by ring in graphite.

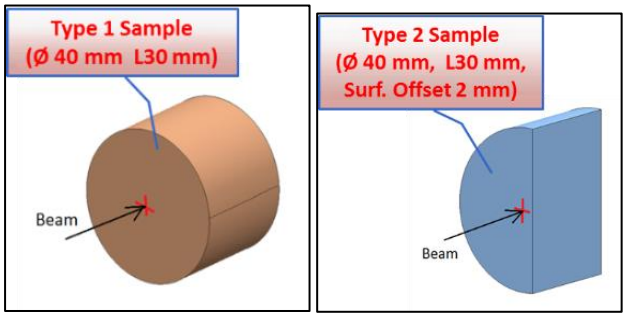

Fig. 8.8: Material specimen shapes for medium intensity (type 1 - left) and high intensity (type 2 - right).

The sample holder was designed for containing the two types of specimens vertically arranged (as shown in Fig. 8.9). It is made in Al 6082-T6, which presents low density and good elastic limit. The supports and the spacers of the samples are in graphite and this minimizes the shock-wave transfer from the impacted specimen to the entire structure. The sample holder has two degrees of freedom (vertical and lateral) and is contained in a vacuum tank, to avoid emission of irradiated material. The vacuum-vessel is in stainless steel and has a series of optical viewports, with a transparent window, designed to withstand internal vacuum and fragment impacts. Moreover, a set of mirror is embarked.

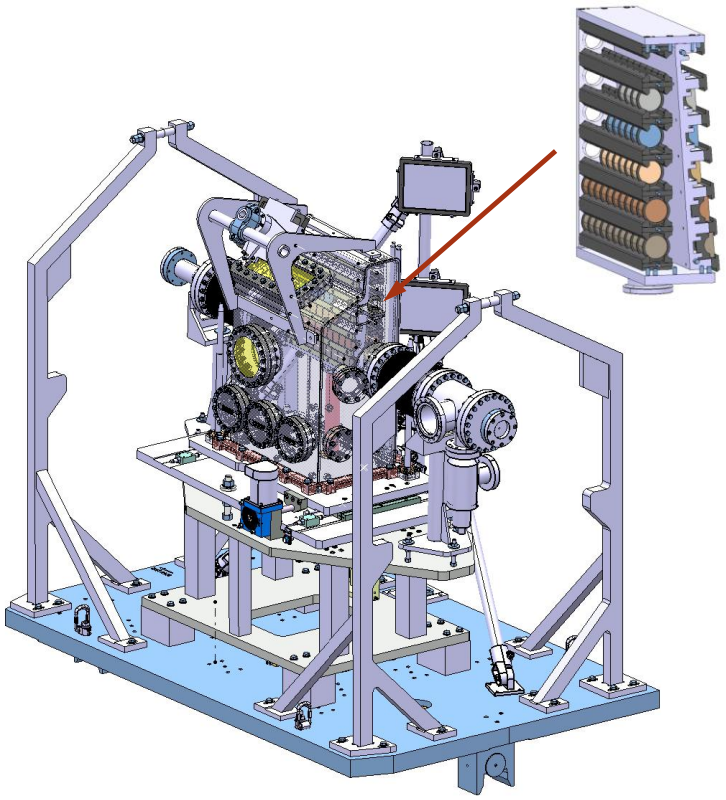

Fig. 8.9: General assembly of the HRMT-14 test-bench and particular of the material sample holder.

8.1.3 Instrumentation

As outlined in the introduction, the experimental data were obtained from strain-gages, temperature sensors, Laser Doppler Vibrometer (LDV) and high speed camera. Given the high radiation level expected during the experiment, only radiation-hard equipment could be installed in-situ.

The strain-gages were placed on the single samples in order to measure both longitudinal and hoop strains. In total, 244 resistive strain-gages (112 for the hoop strains and 112 for the longitudinal one) were used, with maximum amplitude of 3000 με and a sample rate of 4 MHz. Both the two type of specimens were instrumented with strain-gages.

The temperature was measured with 36 thermocouples Pt100 both on type 1 and type 2. The maximum temperature has not to exceed 150 °C.

A Laser Doppler Vibrometer (LDV) measured the radial velocity on the outer surface

of one cylindrical sample per material and only for the medium intensity specimens (type 1). A system of aligned mirrors was put in place to reflect the laser beam back to the vibrometer, positioned inside the protected bunker 40 m upstream of the experimental area. The maximum recordable velocity is 24 m/s and the sampling rate was 2.5 MHz.

A high-speed camera (20000 f/s) was used to film the particle projection produced by impacts on type 2 specimens. In this way, the particle front propagation was followed. The problem related with a high speed video is related to the lighting. As a matter of fact, it is necessary to have a lot of light for the acquisition. It was provided by a battery of radiation-hard xenon flashes mounted on the tank, which were, carefully, synchronized with the beam arrival, to ensure the sufficient level of luminosity.

8.1.4 Experimental phase

The tests were performed between the end of September and the first week of October 2012. The beam energy was 450 GeV, the bunch spacing 25 ns and the maximum intensity of each bunch was 1.1×1011 protons. For each pulse the number of bunch available could vary between 1 and 144. In total a number of 52 pulses where used, which correspond to 1558 bunches. The beam size was 1.5×1.5 mm in case of medium energy impact and 2×2 mm for high intensity tests. In Table 8.1 and 8.2, the summary of all the performed tests is reported, divided for the two types of specimen.

Table 8.1: Medium intensity tests.

Material	**Total number of protons $\times 10^{12}$**	**Total number of bunches**	**Total number of pulses**
Inermet 180	4.3	51	6
Molybdenum	8.0	112	7
Glidcop	7.8	111	6
MoCD	14	135	7
CuCD	14	136	8
MoGr	15	149	10

Table 8.2: High intensity tests.

Material	**Total number of protons $\times 10^{12}$**	**Total number of bunches**	**Total number of pulses**
Inermet 180	9.1	72	1
Molybdenum	2.85	216	2
Glidcop	17.7	144	2
MoCD	19.6	144	1
CuCD	19.5	144	1
MoGr	19.5	144	1

8.1.5 Experimental results

A very large amount of data was acquired during the experiment and is currently under intense post-processing. As said above, the main goals of the experiment are to corroborate the simulation methods, increasing confidence in advanced simulation techniques, validate existing material constitutive models and derive new constitutive models for less known materials. This is mainly done by benchmarking strains and velocities measured on the outer surface of the specimens and pictures taken during impacts on type 2 samples with simulation results, as well as by performing post-irradiation analyses of impacted specimens.

Records concerning better known materials (Inermet and Glidcop) were treated first; preliminary results are presented below. The comparison of the results is made on the basis of the numerical simulation obtained with the FE code AUTODYN [3].

For the simulation on medium intensity impact on Glidcop, the strength material model used is the J-C model, the EOS is the tabular SESAME EOS 3320 and failure model is the pure copper one. In spite of this approximation and of the difference in beam transverse size, experimental measurements (strain-gages and LDV) and simulations are in very good agreement. In Fig. 8.10, red, black and green dotted lines are referred to the hoop strains measured by strain gauges placed on the external surface with 90˚ azimuthal spacing: in principle, given the axial symmetry of load and geometry, the three lines should be superposed. Slight fluctuations must be analysed, but are possibly mainly due to noise on cables and gauges during the acquisition as well as to errors on the beam impacting position. It is also interesting to note that electromagnetic noise induced by the particle

beam perturbed the strain-gage measurements during a few microseconds after the impact, concealing the first deformation peak; however, this interference died out immediately after, allowing capturing the remainder of the phenomenon. In Fig. 8.10, also the radial velocity measurement obtained from the LDV (blue dot markers) is compared with the radial velocity obtained from the numerical simulations.

The good matching between numerical results and experimental measurements confirms the reliability of the simulations techniques as well as the validity of the EOS and strength model for Glidcop. A similar approach will be adopted in the near future for those other materials for which constitutive models are relatively known (Inermet and molybdenum). For novel materials the approach will be somehow different: combining measurements and theoretical work, constitutive models will be conjectured and implemented in the hydro-code models, then benchmarking simulations results against measured values will allow iteratively converging towards consistent material models.

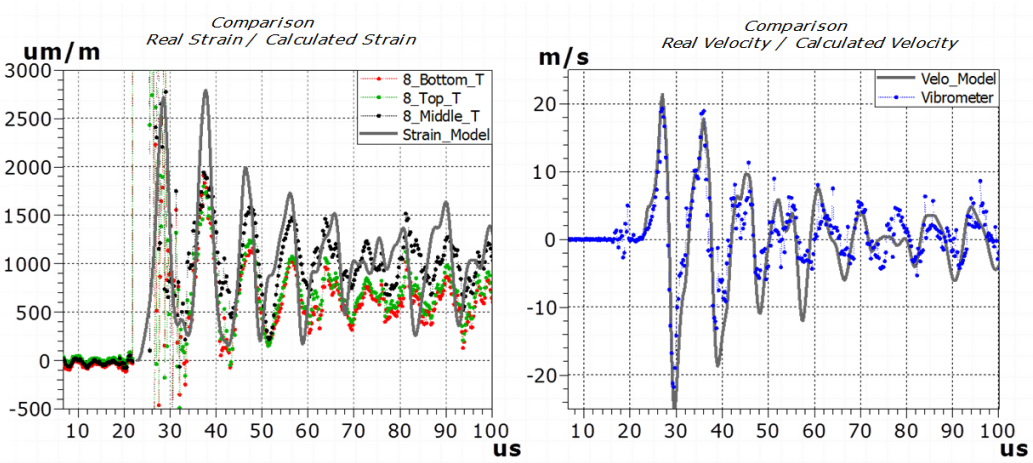

Fig. 8.10: Hoop strain: comparison between measurements of three strain gauges and numerical model (left); radial velocity measured by the vibrometer, in blue, and simulated one, in black (right).

The high-speed camera and flash systems allowed to record images of the impact of a hadron beam on solid targets and of the effects this induced. The most remarkable phenomena occurred during beam impact on Inermet, the material with the highest stopping power. Also in this case, the comparison is made on the basis of the simulation obtained in AUTODYN. The strength material model used is the J-C model, the EOS is the table 3550 of the SESAME EOS and the failure model is an imposed minimum pressure. All the material data used are for the pure tungsten.

As shown in Figs. 8.11 and 8.12, a large quantity of hot material was ejected at high

velocity from the two most loaded samples. The high temperatures reached are confirmed by the intense light emitted by the fragments during a few hundred microseconds.

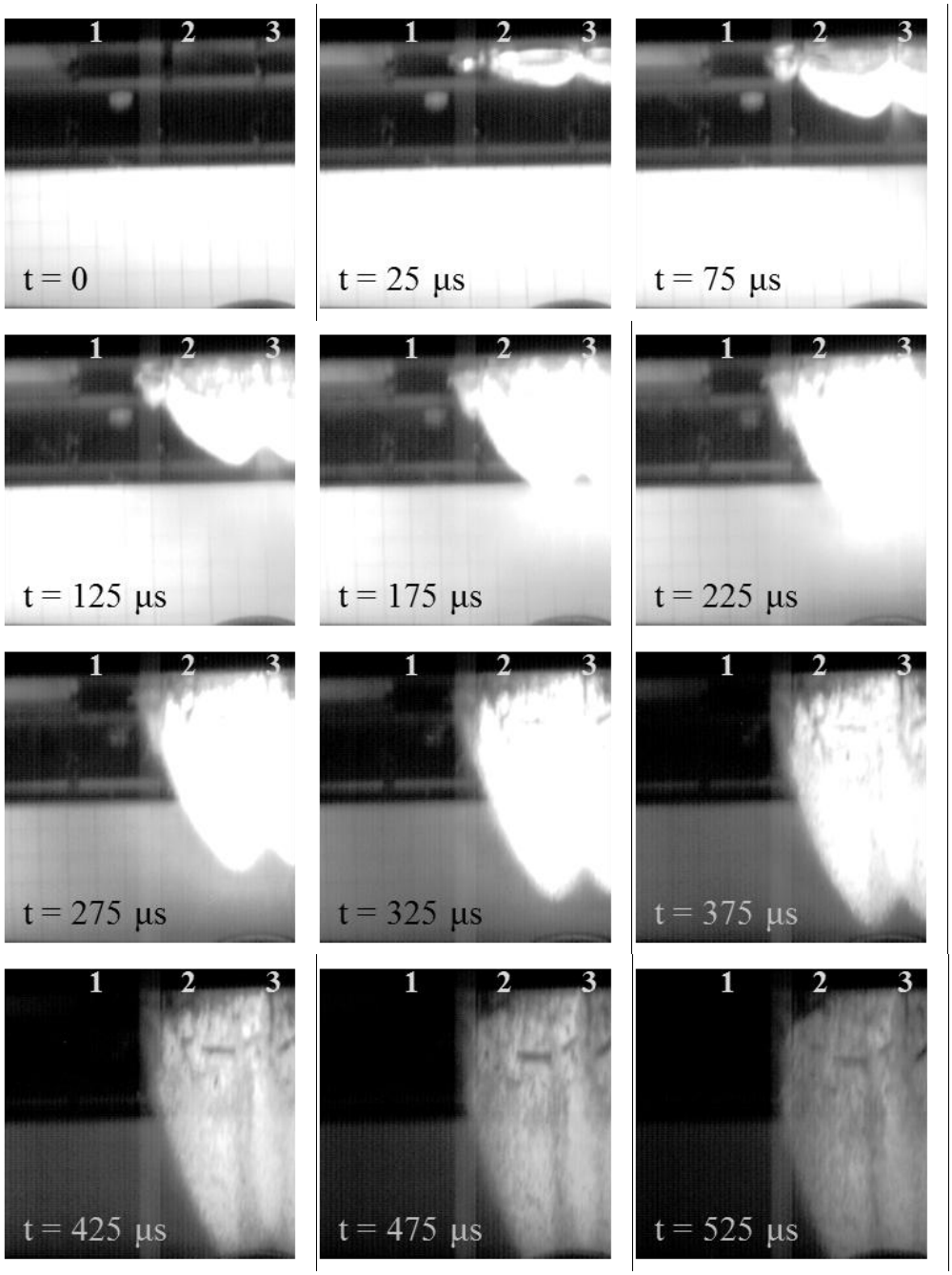

Fig. 8. 11: Image sequence of the impact on Inermet® 180 of a 72 bunches proton pulse. Beam is coming from the left; three Inermet samples are partially visible and are numbered in the picture.

Both ejected particle front shape and velocity are consistent with high-speed camera acquired data (Fig. 8.12), even considering the differences between real and the simulated

scenarios. The estimated velocity of the fragment front, as acquired, is ~275 m/s, well matching the simulated velocity of 316 m/s.

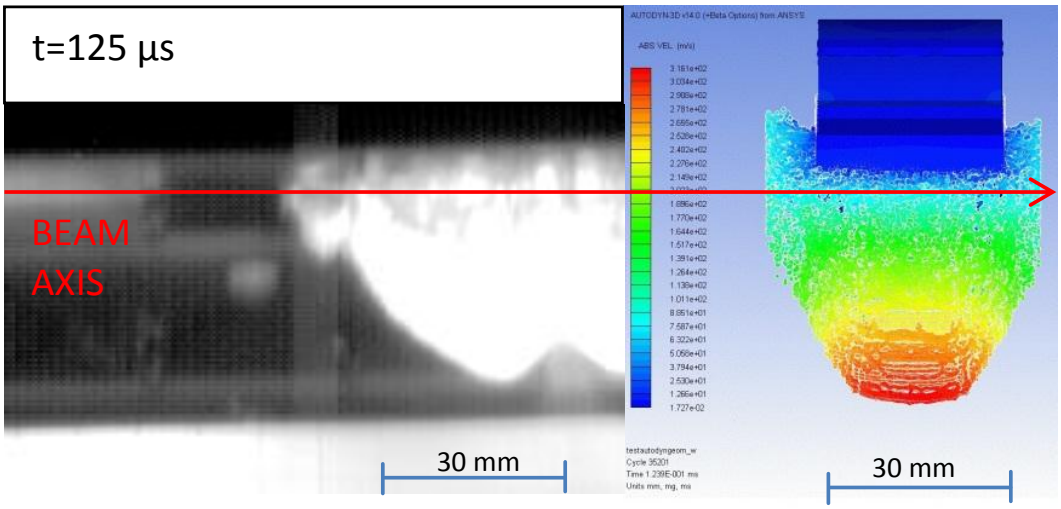

Fig. 8.1:. Comparison between simulation (SPH method) and acquired image ~125 µs after the impact.

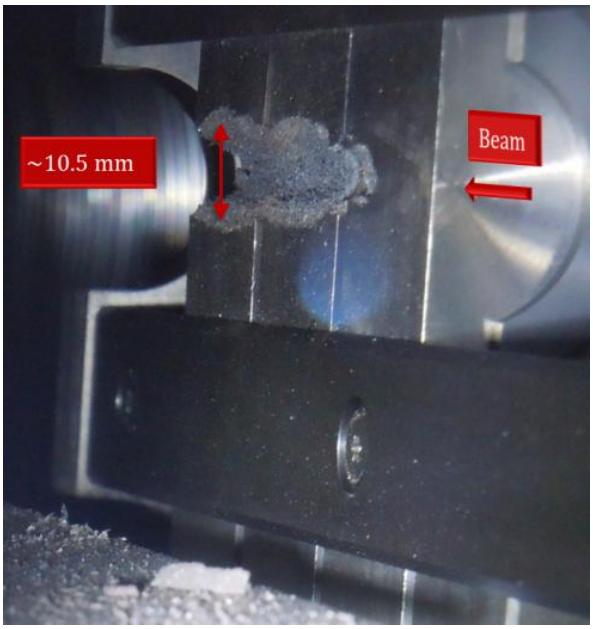

Fig. 8.13: Damage on Inermet provoked by impact of 72 bunches (9.05e12 protons).

Only limited and rapid visual observations were allowed after the experiment on account of the high residual dose levels. Valuable information was nevertheless gathered about the beam impact resistance of the densest materials (Fig. 8.13). < and on the flat surface. The low-melting point of copper and nickel probably played an important role in determining the extent of damaged zone.

References

[1] Efthymiopoulos I., et al., "HiRadMat: a New Irradiation Facility for Material Testing at CERN", IPAC'11 (2011).

[2] Bertarelli A., et al., "Research and Development of Novel Advanced Materials for Next-generation Collimators", IPAC'11 (2011).

[3] Bertarelli A., et al., "An Experiment to Test Advanced Materials Impacted by Intense Proton Pulses at CERN HiRadMat Facility", CERN-ATS-Note-2013-005 TECH (2013).

9. Conclusions

The understanding of the material response in the case of high strain-rate, impact or shock loading is fundamental in several applications, such in ballistic, nuclear and military fields. The main objective of this thesis was the development of accurate and reliable numerical methods for the description of such extreme phenomena, in order to be able to predict dynamic events, such as high velocity or high energy impacts, detonation of explosives and high energy depositions. To do this, first of all it was necessary to understand which are all the variables involved. To reach this goal, a general study of the wave and shock-wave propagation in solids was performed. In general, in case of shock loading conditions, producing the propagation of waves, the material is allowed to deform only in the impact direction, while in the orthogonal direction the deformation is prevented (or limited) by the inertia. This implies that a uniaxial strain state is generated to which also a great level of pressure is associated. The results obtained from simple numerical models, in case of purely hydrodynamic material, demonstrated that no signals move ahead the shock front: the shock front is supersonic relative to the undisturbed material. Otherwise, in case of shocked material, the sound speed is higher than the signal speed: the shock front is subsonic with respect to the shocked material. This means that any disturbance can catch the shock front from behind and explains why a shock front is spontaneously generated starting from a quite smooth pressure signal. Another important point is that, after the end of the planar shock, the shocked material returns in the undisturbed condition. This is not true in case of cylindrical wave propagation, for which, due to the axisymmetric constraint, the shock is always followed by a negative pressure wave. After that, the case of solid material was considered, for which also the material strength had to be taken into account and three cases were examined. For low pressure wave that material remains elastic and a single elastic front is generated, which propagates at the solid sound speed. For medium intensity shock, the material enters the plastic

domain: two different pressure fronts are generated (elastic and plastic), which moves at different velocity (the plastic wave moves with a lower velocity). Depending on the intensity of the shock, the material could yield also during the unloading phase. The last case implies that a very strong shock is generated, a single plastic supersonic front.

All these results were very useful in the prediction of the evolution in case of high energy deposition case, which is reported, in this thesis, as application of strong shock-wave propagation in matter. In more details, the case of LHC high energy beam impact against solid targets was deeply investigated. When a particle beam interacts with a solid target the particles deposit their energy in the material. This provokes a dynamic response of the structure entailing thermal stress waves and thermally induced vibrations or even the failure of the component. The pressure and temperature increase and the materials could reach at its melting temperature or vaporize, depending on the impact conditions. The remaining part of the material, which remains solid, is characterized by high values of plastic strain, strain-rate and temperature. From these considerations it is clear what was the complexity of the problem, which needed of a multi-physics approach to be completely examined.

The main objective of the thesis was the development of accurate and reliable methods for the numerical description of these events. The FE code used was LS-DYNA and all the cases analyzed regarded multi-bunch impacts.

In order to correctly simulate the thermo-mechanical response of the material it was necessary to take into account both the hydrodynamic behaviour, using a dedicated Equation Of State (EOS), and the deviatoric behaviour, using a dedicated strength material model. Due to the fact that the material involved could experience a lot of changes of state, multi-phase EOS, taken from the SESAME Library, were used. Moreover, since the mechanical quantities, which influence the phenomenon, are strain (both plastic and volumetric), strain-rate, temperature and pressure, the material models used were Johnson-Cook and Steinberg-Guinan. For what concerns the EOS, since in LS-DYNA the SESAME is not implemented, it was necessary to interpolate the tabular data with a polynomial formulation. This aspect was very crucial, since an ad-hoc interpolation was done for each element of the numerical model, depending on the estimation of its position of the EOS surface.

The numerical models were constructed starting from the evaluation of the thermal loads on the impacted material performed by the FLUKA Team at CERN, using the

statistical code, called FLUKA. The provided FLUKA maps were used as starting point in the thermo-mechanical simulations.

As first approach, the numerical simulations of cylindrical targets, made in copper and tungsten, impacted perpendicular at the centre of one face by 8 bunches of LHC at 7 TeV, were performed. The fact that both the target geometry and the load applied, in terms of energy deposition, were axisymmetric allowed treating the problem as axisymmetric, simplifying the 3D problem in a 2D one. The results showed that the energy delivered on the impacted (central) part of the component acts as an explosive: during the deposition phase the pressure grows up, reaching very high values. Once no more bunches are delivered, the shock-wave starts to travel from the central zone to the external surface. The pressure evolution is strictly related to the density changes and the energy deposition, in accordance with the EOS. The travelling shock-wave produces a rarefaction in the material placed behind and a compression in the material placed ahead of it. The central part of the target corresponds to the zone where the material rarefaction is. This part of material could be subjected to sudden and continuous changes of state. The remaining part of the target behaves similarly to the solid state resulting compressed by the transition of the shock front and then expanded by the travelling of the shock-wave. The analysis of the damage in the component showed that the principal damage source is represented by the change of state (vaporization and melting), while spallation and ductile damage are missing. The reason is that the part of the target taken into account for this analysis was prevalently subjected to compressive stress that did not produce any cumulative damage or spallation. The last phenomenon will probably happen as soon as the shock-wave will be reflected by a free surface or if the target is hit near a free surface, but the latter case cannot be simulated with a 2D axisymmetric model. Looking at the results in terms of path on the EOS surface allowed to observe that in the part close to the maximum energy absorption, during the deposition phase, there is a sudden increase in the internal energy with a negligible variation in the material density (isochoric transformation), but when the rarefaction process starts, the material could be expanded (reaching lower values of pressure and density). For the part of the target, in which low values of energy are deposited, the deposition phase leaves these elements quite undisturbed: the consequent growth in pressure is limited and no significant changes in density occur. On the other hand, when the shock-wave reaches these elements, they are strongly compressed, reaching high values both in density and pressure.

An improvement of the numerical model was got simulating a 3D more complex geometry, in which there was also the presence of two different materials in contact. The model represented a jaw of a tertiary collimator (TCT), made by an insert in tungsten alloy surrounded by a C-structure in copper. The case analyzed regarded the simulation of the impact of 8 bunches of LHC at 5 TeV, which hit the tungsten alloy part near the free surface. The results showed that: during the deposition phase the pressure evolution is quite similar to that of the 2D cylindrical case. Once the deposition is finished, the shock-wave starts and moves cylindrically from the hit zone. The pressure wave reaches in a short time the free surface of the tungsten part and is reflected back. The fact that this reflection happens on a free surface implies that the pressure wave is transformed in a tensile hydrostatic wave of the same intensity. The spall model limits the value of the negative pressure and this condition corresponds to the failure of the material. The consequence is that the material is ejected from the surface at high velocity. The shock-wave, propagating in the opposite direction (towards the copper part), is then followed by a high negative pressure wave. When the pressure wave reaches the interface between the two materials, due to the significant differences in impedance, the shock-wave is in part reflected in tungsten, with the potential spallation phenomena, and in part transmitted into copper, with a reduction of the pressure level.

By the comparison between the FLUKA energy maps obtained for different target materials, it was possible to notice the dependency between the density and the amount of energy absorbed, as well as the penetration length and the stopping power. The probability of interaction between particles and materials is strongly density dependent and the material density plays a key role in the calculation of the proton energy loss in matter. This implies that two materials subjected to the same impact condition, but with different atomic numbers (Z numbers), experience different energy absorption. In particular, the higher the atomic number of the material, the higher its energy absorption. Besides, it means also that, for the same material, if there is a density evolution during the simulation, it should be taken into account in order to recalculate the energy deposition in the material in these new conditions.

The last consideration was at the basis of the further improvement in the numerical model, for which a soft coupling between FLUKA and FE code LS-DYNA was developed, in collaboration with the FLUKA Team at CERN. The routine was implemented in Matlab and iteratively, run the two codes. The method was applied to

simulate the beam impact against a 3D tungsten target. The FLUKA model was built using the voxel geometry and the FE one using 3D solid elements. Comparing the results obtained for coupled and non-coupled simulations it was possible to make some important considerations. The material, in which a great amount of energy is deposited, is subjected to a significant density reduction during the shock-wave propagation. This implies that the material becomes more transparent to the next proton bunches, and consequently the probability of interaction decreases. This provokes the so called tunnelling effect. The consequences of this are that the proton beam penetrates more in depth in the material in the beam axis direction and the energy is more diluted over the target. The density distribution emphasizes the tunnelling: the density modification involves much higher longitudinal coordinates increasing the number of bunches. The results in terms of pressure showed that the maximum of pressure remains more or less in the same longitudinal position with respect of the first bunch, but the pressure wave starts to travel in the transversal directions. The fact that the energy deposited by the following bunches is lower and more widespread implies that the pressure increment, consequent to the next bunches, is reduced in the zone, in which the first bunch deposited a greater amount of energy. On the other hand it should increase in the part of the target, where there is an increment in density. The results obtained showed also that until 8-10 bunches (~200 ns), the differences between the two simulations are negligible. Thanks to this, it was possible to conclude that the results obtained from the previous analysis (2D and TCT simulations) could be considered reliable. After this time however, the change in density becomes relevant, because the shock-waves has the time to travel away from the impacted zone, producing a great rarefaction in the middle. The consequence is the two simulations give more and more different results increasing the number of bunches. In particular two situations could be developed, depending on the position on the target. For the elements situated in the neighbourhood of that in which the maximum energy was deposited by the first bunch, the uncoupled simulation overestimates the pressure. This could be easily explained since those elements are subjected to the greatest density variation. Consequently they become more transparent to the proton beam and the successive bunches deposit on them lower energy, which implies lower growth in pressure. Otherwise, elements that are situated along the beam direction at higher longitudinal coordinates (far from the maximum energy region), are subjected to higher energy deposition during the successive bunches due to the tunnelling effect with respect to the

first bunch. Obviously, this provokes an underestimation of the pressure level in case of uncoupled analysis.

As conclusion of this study, a first-of-its-kind experiment was described: six different materials (Inermet® 180, Glidcop® AL-15, Molybdenum, Molybdenum-Copper-Diamond, Copper-Diamond and Molybdenum-Graphite) were impacted under controlled situation with a certain number of proton bunches at 450 GeV. The aim of the experiment was to validate numerical models and extract material data in terms of strength and EOS models, especially for novel materials. The experiment was performed in the HiRadMat facility at CERN in October 2012 and some preliminary results on Glidcop and Inermet 180 were compared with those obtained from numerical simulations of similar events. The good match between numerical results and experimental measurements confirmed the reliability of the simulations techniques as well as the validity of the EOS and strength model used. Similar approaches will be adopted in the near future for those other materials for which constitutive models are relatively known. For novel materials the approach will be somehow different: combining measurements and theoretical work, constitutive models will be conjectured and implemented in the hydro-code models, then benchmarking simulations results against measured values will allow iteratively converging towards consistent material models.